

Control for Bipolar DC Microgrid and DC/DC Bidirectional Converter in Energy Access Context

Thesis Report

Xiaochuan Zhou



Control for Bipolar DC Microgrid and DC/DC Bidirectional Converter in Energy Access Context

by

Xiaochuan Zhou

in partial fulfillment of the requirements for the degree of

Master of Science

in Electrical Power Engineering

at the Delft University of Technology,

to be defended publicly on Wednesday August 23, 2023 at 13:00.

Supervisor:	Dr. Zian Qin Dr. Ir. Laurens Mackay	TU Delft DC Opportunities R&DBV
Thesis committee:	Prof. Dr. Ir. Pavol Bauer Dr. Zian Qin Dr. Mohamad Ghaffarian Niasar Dr. Ir. Laurens Mackay	TU Delft TU Delft TU Delft DC Opportunities R&DBV
Company supervisor:	Ir. Jesse Echeverry	DC Opportunities R&DBV
University advisor	Ir. Sachin Yadav	TU Delft
Project Duration:	November 2022 - August 2023	
Student number:	5489415	

This thesis is confidential and cannot be made public until August 23, 2023.

An electronic version of this thesis is available at <http://repository.tudelft.nl/>.



Copyright © Xiaochuan Zhou, 2022
All rights reserved.

Abstract

*Xiaochuan Zhou
Delft, August 2023*

Rural electrification remains a significant challenge for engineers, given its intricate relationship with multiple issues, including geographical constraints and underdeveloped infrastructural provisions. As a result, with the development of Solar Home Systems (SHS) and direct current (DC) microgrids, DC systems for energy access have emerged as a promising solution.

In this context, a bidirectional DC/DC converter serves as a bridge connecting the SHS and the grid. Thus, it is important to design a converter's control mechanism to ensure a smooth and efficient exchange of power in both directions. Beyond this aspect, the system perspective involves the coordination of photovoltaic (PV), battery storage, and grid power supply priorities within the SHS. Consequently, this thesis centers its attention on two objectives: the control of the bidirectional DC/DC converter and the system-level control of the DC microgrid.

To ensure high efficiency under variable loads and smooth transitions between two directional operations, this thesis proposes and evaluates a novel control methodology. Transfer functions are derived through mathematical modeling and PI parameters are determined by analyzing Bode-Plots. This work also shows the simulation and testing results. Both results demonstrate that the proposed control method achieves a high efficiency under light load conditions, maintaining a stable output voltage despite load power dramatic fluctuations.

Analysis of energy exchange between the DC microgrid and SHS involves a bipolar DC microgrid model based on an established grid in Matlab/Simulink. Employing droop control, which is a widely used decentralized strategy, for each converter within the grid. To ensure priority order of power supply in the system, a system-level decentralized control methodology is developed, assuming internal communication within the SHS. Through simulation, the priority order of PV, battery, and grid is verified, along with the impact of dynamic shifts between scenarios on the load. However, given the absence of communication devices in the existing SHS, an alternate decentralized coordinated control strategy is developed and simulated, without direct communication interfaces. Simulation results demonstrate that the SHS bus voltage remains stable even with power supply changes.

Keywords: Rural Electrification, Bipolar DC Microgrid, Dual Active Half Bridge (DAHB), ZVS, Decentralized Control, Burst Mode Operation, Droop Control, PI Control

Contents

Abstract	ii
Nomenclature	vi
List of Figures	vi
List of Tables	x
1 Introduction	1
1.1 Background	1
1.2 Research Motivations	3
1.3 Research Objectives	4
1.4 Research Questions	4
1.5 Contributions	4
1.6 Proposed Approach	5
1.6.1 Dual Active Half Bridge Converter(DAHB)	5
1.6.2 DC Microgrid	5
1.7 Thesis Outline	5
2 Literature Review	6
2.1 Isolated bi-directional DC-DC converter	6
2.1.1 DAB and DAHB	7
2.1.2 Modulation strategies	7
2.1.3 State space modeling	9
2.1.4 Developing modeling of a DAHB	10
2.1.5 Control of a DAHB	11
2.2 PV-based DC microgrid	12
2.2.1 Solar home System	12
2.2.2 DC microgrid	12
2.2.3 Decentralized control	14
3 Modeling of Dual-Active-Half-Bridge DC/DC Converter	19
3.1 Overview	19
3.2 Topology	19
3.2.1 Comparison with a conventional DAB converter	19
3.2.2 Active clamp circuit	20
3.3 Power transfer Characteristics	22
3.3.1 Charging operation principles	23

3.3.2	Discharging operation principles	24
3.4	Steady-state analysis	25
3.4.1	boundary conditions	25
3.4.2	Output characteristics	25
3.4.3	ZVS	27
3.5	Dynamic analysis	28
3.5.1	Mathematical model derivation	28
3.5.2	Average model	30
3.5.3	Small signal model	30
3.5.4	Control system design	32
3.6	Conclusion	36
4	Modeling and Droop Control of DC Microgrid	37
4.1	Overview	37
4.2	Schematic	37
4.3	Components modeling	38
4.3.1	MPPT converter	38
4.3.2	Voltage balancing converter	42
4.3.3	DC load	43
4.3.4	Battery and bidirectional converter	44
4.3.5	Solar Charging Station(SCS)	47
4.4	Conclusion	48
5	Converter Controller Design and System Control Design	49
5.1	Overview	49
5.2	DAHB	49
5.2.1	Single phase shift with burst mode operation	49
5.2.2	Dynamic burst mode control strategy	51
5.3	Coordinated Control	53
5.3.1	Decentralized control with centralized SHS	53
5.3.2	Decentralized control with decentralized SHS	55
5.3.3	Comparison of two decentralized control	58
5.4	Conclusion	58
6	Simulation and Testing Results	59
6.1	Overview	59
6.2	DAHB simulation and testing results	59
6.2.1	DAHB simulation results	59

6.2.2	DAHB prototype testing	63
6.3	DC Microgrid simulation and testing results	67
6.3.1	DC microgrid simulation results	67
6.3.2	DC microgrid testing results	71
6.4	Testing results	73
6.5	Conclusion	77
7	Conclusions	78
7.1	Future work	79
	References	80
A	Cascaded PI Control for a DAHB Converter with SPS	84
A.1	Cascade PI control	84
A.2	Simulation results	85
A.3	Conclusion	85
B	Experimental Setup	86
B.1	Power Electronic Converters	86
B.2	Laboratory Power Supplies	86
B.3	Laboratory loads	87
	Acknowledgements	88

Nomenclature

Abbreviations

Abbreviation	Definition
IEA	International Energy Agency
DAHB	Dual Active Half Bridge
SPS	Single Phase Shift
SCS	Solar Charging Station
SHS	Solar Home System
MPPT	Maximum Power Point Trackers
SoC	State of Charge

Symbols

Symbol	Definition	Unit
L_s	Transformer leakage inductor	[H]
i_L	Transformer leakage inductor current	[A]
C_{in}	Input capacitor	[F]
$S_{1,2,3,4}$	Primary and secondary main switches	
$S_{3a,4a}$	Switches of active clamping circuit	
$C_{3,4}$	Resonance capacitors of the active clamping circuit	[F]
C_5	Output capacitor	[F]
n	Transformer turns ratio	
v_1	input capacitor C_{in1} voltage	[V]
v_2	input capacitor C_{in2} voltage	[V]
v_{5p}	C_5 voltage reflected to primary side	[V]
C_{5p}	C_5 reflected to primary side	[F]
R_{op}	output resistor reflected on the primary side	[Ω]
r_s	C_5 Input resistor	[Ω]
V_{HV}	DC microgrid side high-voltage	[V]
V_{LV}	SCS side low-voltage	[V]
V_{ab}	Voltage on the transformer's primary side	[V]
V_{cd}	Voltage on the transformer's secondary side	[V]
Φ	phase shift	[$^\circ$]
T_S	Switching period	[s]
f_s	Switching frequency	[Hz]
P_o	Actual output power	[W]
P_{unit}	Normalized output power	[W]
M	Voltage ratio of the voltage on the two sides of the transformer	
R_o	Output resistor	[Ω]
D_b	Duty cycle in burst mode operation	
P_b	Actual output power in burst mode operation	[W]

List of Figures

1.1	Number of people without access to electricity, 2000-2019[3]	1
1.2	Electricity access, 2020[4]	2
1.3	A comparison of solar-power benchmark LCOE targets for 2030 with historical values[8]	2
1.4	Power generation from solar PV in the net zero configuration, 2010-2030[7]	3
1.5	System overview - energy access	4
1.6	Outline of the thesis and the interrelation between the chapters	5
2.1	IBDC topology	6
2.2	DAHB converter topology	7
2.3	DAHB Modulation techniques	8
2.4	Waveforms of a DAB converter within the burst mode operation[22]	9
2.5	Comparison of DAB modeling methods	11
2.6	Comparison of DAB control methods	12
2.7	SHS consists of a single PV, MPPT converter, battery, and loads	13
2.8	Common topologies used for power sharing grid	13
2.9	Example of LVDC distribution system	14
2.10	Voltage balancing converter	15
2.11	System hierarchical control structures[43]	15
2.12	Possible current-voltage characteristic for the local control of a storage converter[45]	16
2.13	Comparison of MPPT algorithms	17
2.14	P-V and I-V curves of an ideal PV panel	17
2.15	Battery OCV Vs. SoC	18
2.16	Lumped element models for a line	18
2.17	Bipolar system line impedance model[43]	18
3.1	A modified DAB topology used in energy access[16]	20
3.2	Equivalent circuit of the active damping circuit	20
3.4	DAHB gate signal and output results	21
3.5	Theoretical waveforms of DAHB	22
3.6	Equivalent circuit during various intervals	23
3.7	Operation modes of SPS control and output current	25

3.8	Output power versus phase shift	27
3.9	ZVS range	28
3.10	The simplified circuit of the proposed DAB	29
3.11	Output to control bode plot	32
3.12	Block diagram of feedback control	32
3.13	Charging mode: output results with variable K_p and K_i	33
3.14	Charging mode: stability analysis	34
3.15	Two disturbing tests(0.03s: V_{in} changes from 350v to 355v 0.06s: Rload is doubled)	34
3.16	Discharging mode: output results with variable K_p and K_i	35
3.17	Discharging mode: stability analysis	35
3.18	Two disturbing tests(0.03s: V_{in} changes from 24v to 20v 0.06s: Rload is doubled)	36
4.1	Schematic of a DC microgrid	38
4.2	I-V and P-V characteristics of MPPT converter	38
4.3	MPPT converter topology	39
4.4	Cascade PI Control for the MPPT converter	39
4.5	State machine flowing chart	40
4.6	P&O MPPT algorithms	41
4.7	I-V characteristic for the droop control of converters	41
4.8	Simulation results of MPPT algorithms with a variable irradiance	42
4.9	Voltage balancing converter topology	42
4.10	Droop control for the voltage balancing converter	43
4.11	Effect of a voltage balancing converter in the bipolar DC microgrid	43
4.12	LED inverted buck converter topology	44
4.13	Droop control for the LED inverting buck converter	44
4.14	Simulation results of the inverted buck converter and LED with variable PV energy	44
4.15	Battery buck-boost converter topology	45
4.16	Droop control for the battery buck-boost converter	46
4.17	Simulation results for the battery buck-boost converter charging operation modes	46
4.18	Simulation results of battery buck-boost converter with variable PV energy	46
4.19	I-V characteristic of the battery droop control at different SoC	47
4.20	24V SCS schematic consists of an MPPT converter, a single battery, and a power bank as a load	47
4.21	SCS-MPPT converter	48
4.22	Simulation results of the 24V Solar Charging System with variable PV energy	48

5.1	Single Phase Shift(SPS) control with voltage feedback block diagram	49
5.2	Power variation with burst duty cycle	50
5.3	Single Phase Shift (SPS) with burst mode (a) Db=0.25 (b) Db=0.5	50
5.4	Novel burst mode with reset phase and SPS hybrid control method block diagram	51
5.5	Transition points between switching modes of proposed control technique	51
5.6	Hysteresis control scheme for burst mode operation	52
5.7	Decentralized control with centralized SHS	53
5.8	Possible operation scenarios of decentralized control with SHS	54
5.9	Decentralized control with decentralized SHS	56
5.10	Possible operation scenarios of decentralized control with SCS	57
6.1	Simulation model built in Matlab/Simulink	60
6.2	Typical DAHB waveforms with SPS	60
6.3	Typical DAHB waveforms dynamic SPS and burst mode control	61
6.4	Simulation results with approached dynamic SPS and burst mode control	62
6.5	Simulation results of the novel burst mode with reset phase and SPS hybrid control method	63
6.6	Prototype test	63
6.7	SPS with Db=0.25 prototype testing results from Grafana	64
6.8	SPS with Db=0.25 prototype testing results from Picoscope	64
6.9	Prototype testing results (Vref=24V)	65
6.10	Prototype testing results (Vref=29V)	65
6.11	Prototype testing results from Picoscope	66
6.12	Measured prototype efficiency	66
6.13	Prototype testing results ($\phi_{max} = 50^\circ$)	67
6.14	Simulation and prototype testing comparison between $\phi_{max} = 30^\circ$ and $\phi_{max} = 50^\circ$	67
6.15	DC microgrid model in Matlab/Simulink	68
6.16	Coordinate control with SHS simulation	69
6.17	Coordinate control with SCS simulation	71
6.18	DC microgrid simulated circuit breaker and line impedance	72
6.19	DC microgrid simulated circuit breaker and line impedance	72
6.20	DC microgrid simulation with circuit breaker and line impedance	72
6.21	LED droop control testing	73
6.22	24-hour performance data from DC microgrid converter in Green Village	74
6.23	Power supplies turn off performance data from DC microgrid converter in Green Village	75

6.24 DC microgrid interconnection and LED Droop Control	77
A.1 Cascade double loop control based on novel burst mode with reset phase and SPS hybrid control method block diagram	84
A.2 Cascade double loop control model in Matlab/Simulink	85
A.3 Cascade control simulation results	85
B.1 DAHB converter prototype	86
B.2 SM 500-CP-90 bidirectional power supply from Delta Elektronika	87
B.3 72-13210 DC Electronic Load from Tenma	87

List of Tables

3.1	DAHB modeling parameters	31
3.2	Stable margin with variable Kp for charging mode	33
3.3	Stable margin with variable Kp for discharging mode	35
5.1	Initial phase for dynamic burst operation	52
5.2	Possible operation scenarios and decision making for centralized SHS	55
5.3	Possible operation scenarios and decision making for decentralized SHS	55
5.4	Comparison of decentralized control with both decentralized and centralized SHS	58
6.1	Circuit breaker and line impedance components	72
A.1	PI parameters of cascade voltage and current control	84

1

Introduction

1.1. Background

Electricity is crucial to alleviating poverty, economic growth, and improving living standards. At a global level, the total number of people without electricity access has steadily dropped in recent decades[1]. However, globally, the number of people without electricity is expected to increase by nearly 20 million in 2022 and reach almost 775 million by then[2]. The growth is mainly in sub-Saharan Africa, which accounts for three quarters of the global deficit shown in Fig.1.2.

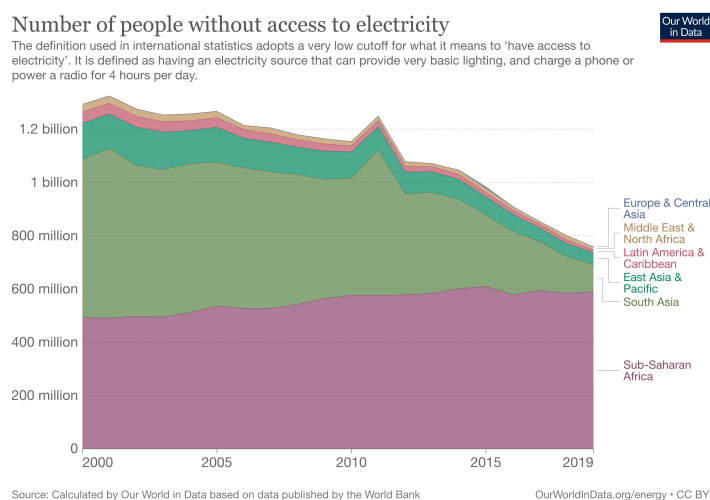


Figure 1.1: Number of people without access to electricity, 2000-2019[3]

In most developing countries, central grids play a high priority in electrification. However, though many villages may have already been reached by the central grid, not all households within those villages have been connected in rural areas[5]. Furthermore, even when a village is formally connected to the grid, there are various barriers, including geographical obstacles and limited and unreliable resources, that prevent households from obtaining and maintaining a reliable electricity connection.

Conventional grid-based models have faced limitations in delivering electricity to rural areas, leading to increased adoption of alternative solutions such as off-grid SHS in recent years[6]. These SHSs, powered by solar photovoltaic (PV) technology, offer several advantages. First, they provide access to clean and sustainable power, addressing environmental concerns associated with traditional energy sources. Moreover, there has been a remarkable decrease in the cost of solar PV modules over the last

Electricity access, 2020



Share of the population with access to electricity. The definition used in international statistics adopts a very low cutoff for what it means to 'have access to electricity'. It is defined as having an electricity source that can provide very basic lighting, and charge a phone or power a radio for 4 hours per day.

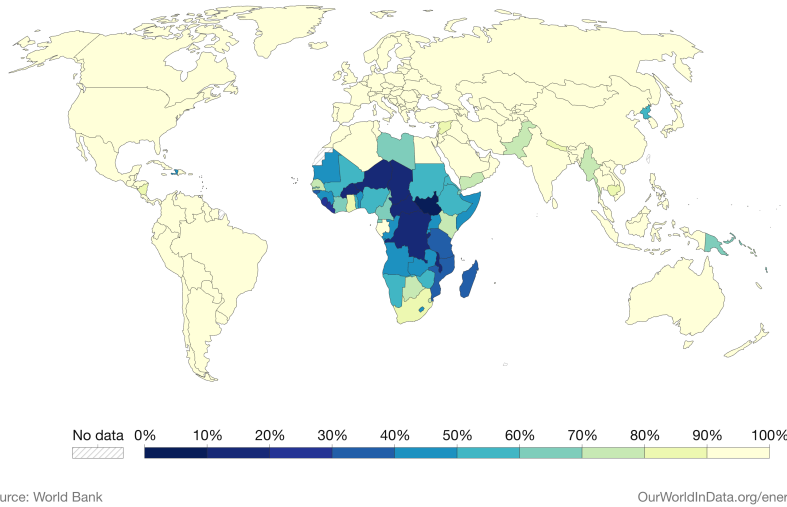


Figure 1.2: Electricity access, 2020[4]

few decades, as shown in Fig.1.3. In fact, the cost of solar PV has experienced a significant reduction of approximately 90% within the last decade. The substantial cost reduction, in conjunction with the implementation of solar policy incentives, has led to a rapid expansion of solar photovoltaic generation [7]. In 2021 alone, power generation from solar PV witnessed a record increase of 179 TWh, marking a remarkable growth of 22% compared to 2020 [7]. The widespread popularity of photovoltaics has consequently made Off-grid SHS highly affordable for households and communities, further promoting their adoption as a reliable and sustainable energy solution.

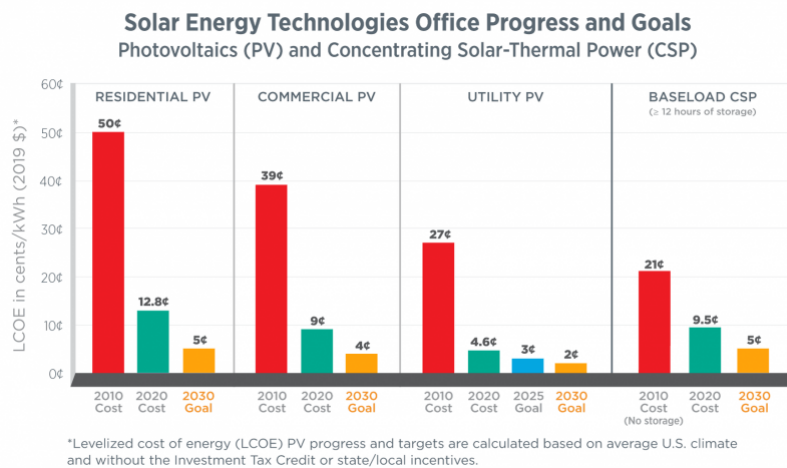


Figure 1.3: A comparison of solar-power benchmark LCOE targets for 2030 with historical values[8]

Standalone SHS consists of a solar panel that absorbs sunlight and converts it into DC power, a battery utilized for storing excess energy for later use, and some loads. However, it is worth noting that these individual standalone solutions have certain limitations, as they do not leverage resource sharing and fail to capitalize on the benefits of usage diversity[9].

A microgrid composed of interconnected standalone SHS presents an alternative solution for providing reliable electricity access in remote areas. In this approach, multiple SHSs are connected to form a DC microgrid, allowing resource sharing and improved system performance. In cases where individual SHS

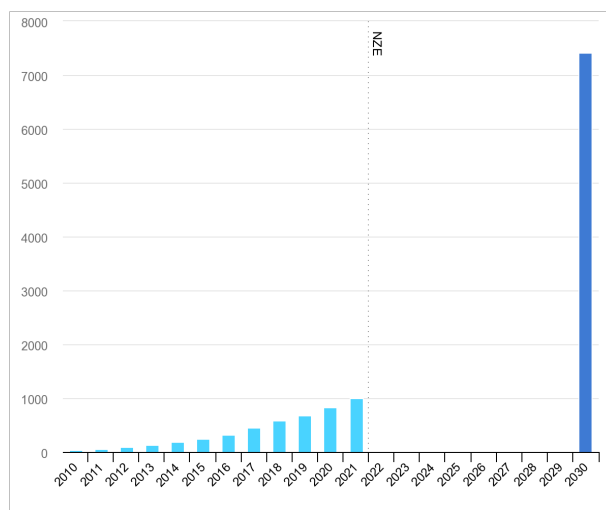


Figure 1.4: Power generation from solar PV in the net zero configuration, 2010-2030[7]

solar panels cannot generate enough energy to meet demand, the microgrid can be supplemented with grid power. This hybrid configuration ensures a continuous and reliable power supply. By integrating the grid as a backup power source, the microgrid can ensure the consistent meeting of power needs.

Bidirectional DC/DC converters are essential components between the grid and SHS due to their ability to manage the power flow between the grid and the loads. The management of bidirectional DC/DC converters has emerged as a pivotal realm of research focus. These converters are not only with maintaining a steady output as loads shift but also with seamless transition between the forward and reverse directional power flow directions. Apart from this, great system-level coordinated control can make sure users always access stable energy even when energy generates shifts. This control strategy improves system stability and resilience, making it an alternative solution for remote areas.

1.2. Research Motivations

Since there are more than a billion people who do not yet have access to electricity due to geographical obstacles together with limited and volatile resources, customized electrification solutions based on these conditions are challenges. Hence, one reliable solution is using modular Solar Home Systems and flexible meshed DC microgrids, which can provide high efficiency, fast dynamic response, bidirectional power flow, and flexible demand[10].

Within a DC microgrid, isolated bidirectional DC/DC power converters assume a significant role. Among these, dual active bridge converters emerge as one of the most promising IBDC configurations due to their ability to automatically adjust bidirectional power flow and wide voltage conversion gain range. To implement converters for high conversion ratio and low voltage and high-current applications, a half-bridge push-pull active clamp converter is proposed. The advantages of these converters are numerous such as simple structure, and the ability to withstand low voltage and high current. In addition, an active clamp circuit is implemented to clamp the turn-off voltage spike on the low-voltage side and suppress the turn-off voltage spike.

In terms of modulation technique, phase shift control is most commonly used in dual active bridge topologies because of its simplicity and the possibility of using half-bridge circuits to generate high-frequency transformer voltages. However, ZVS operation will be lost under light load conditions resulting in low efficiency. To overcome the limitations of the SPS scheme, an investigation into alternative control methods is necessary.

Furthermore, within a decentralized microgrid constituted by interlinked solar home systems, the core

principle revolves around power sharing among users to curtail surplus energy wastage. Consequently, modeling a DC microgrid incorporating an SHS is important. Upon connecting the SHS to the grid, an examination of the system's control strategy becomes essential to ensure the precedence of photovoltaic power and grid power.

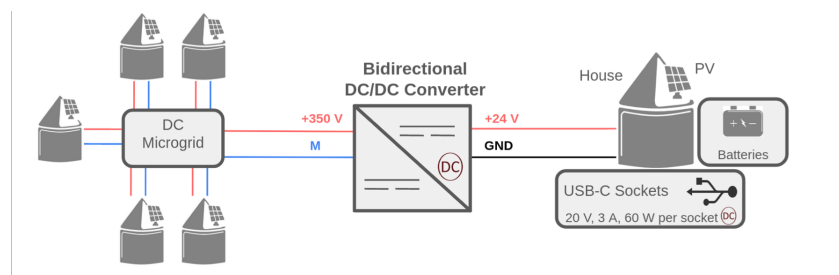


Figure 1.5: System overview - energy access

1.3. Research Objectives

- Stability analysis via state space model;
- Design and test the best method to control the converter to maintain both efficiency and bidirectional control;
- Implement the control into MCU and test prototype;
- Design a DC microgrid that connects to an SHS via a DC/DC bidirectional converter;
- System level control of multiple DC/DC converters using droop control;
- Establish different grid operation configuration that ensure SHS has priority and DC Microgrid is a backup;

1.4. Research Questions

- How to select, model, and implement the DAHB bidirectional control with smooth transitions between forward and reverse directions while considering both efficiency and complexity?
- How to model and design simulation for system-level control for a DC grid used in energy access?
- How can coordinated control be designed and modeled while prioritizing renewable energy and using droop control if DAHB and a solar charging station are considered integrated SHS?
- If DAHB and SCS are independent modules, how do design and model a decentralized control suitable for the existing grid in the Green Village¹?

1.5. Contributions

This thesis makes significant contributions to the model and control strategy of a DAHB converter. Another contribution is the implementation of decentralized control techniques for a DC microgrid used for energy access. The sections in which they can be found are summarized below.

- **Section 3.4** Derive the transfer function of DAHB with a Reduced-order model. Proposed a new method to tune PI parameters and verify stability in zero-pole maps.
- **Section 4.2** Modeling of a realistic bipolar DC microgrid for energy access.
- **Section 5.2** A novel burst mode with reset phase and hybrid SPS control method is designed for the DAHB converter.

¹The Green Village in Delft is one of the living labs where tests and demonstrations will be performed

- **Section 5.3** A coordinated control strategy is developed for the DC microgrid used for energy access.

In addition, the decentralized DC microgrid will be tested, and the results will be compared with the simulated results. This test will verify the realism of the modeling of the DC microgrid module.

1.6. Proposed Approach

1.6.1. Dual Active Half Bridge Converter(DAHB)

- Literature review about DAHB converters;
- Modelling of DAHB including steady-state analysis and dynamic analysis;
- Transfer function derivation and stability analysis;
- Development of control strategy;
- Simulation of the closed loop system with proposed control;
- Prototype testing in the lab.

1.6.2. DC Microgrid

- Literature review about DC Microgrid and decentralized control strategy;
- Establish a system composed of SHS, DC/CD converter, PV, streetlight, and battery;
- Implement system-level control and simulate;
- Create different grid operation configuration prioritizing renewable sources and microgrids as backups.

1.7. Thesis Outline

The outline of the remainder of this thesis, the details discussed in Section 1.6, and the interrelation between the chapters are schematically shown in Fig.1.6.

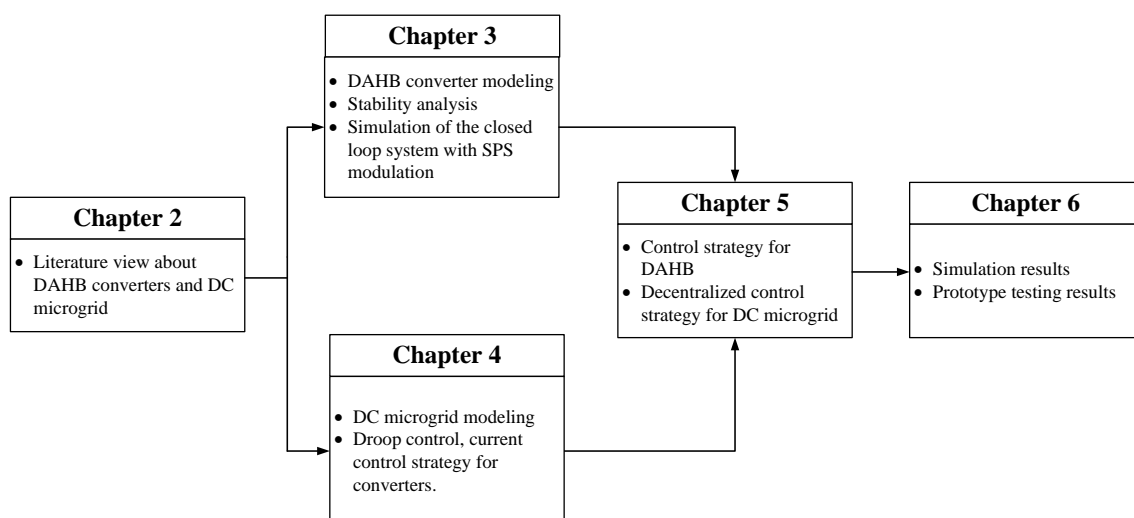


Figure 1.6: Outline of the thesis and the interrelation between the chapters

2

Literature Review

2.1. Isolated bi-directional DC-DC converter

In recent years, DC microgrids have garnered significant attention owing to their broad-ranging benefits such as offering enhanced compatibility with various forms of renewable energy systems and energy storage configurations, alongside improved harmonization with consumer electronics, as elucidated in [11]. For a household configuration with a PV panel, in order to meet the demand of feeding back to the grid when the excess electricity is generated, and obtaining electricity from the grid when it is insufficient, a bidirectional DC/DC converter (IBDC) is used as an interface between the SHS and the DC microgrid.

One of the widely used IBDC is a topology based on two full bridge IUDCs. A typical structure is shown in 2.1a. This topology was proposed to interface between the low-voltage battery and high-voltage DC-link for the motor drive in a hybrid vehicle. The topology was introduced to the connection between the low-voltage battery and the elevated-voltage DC link within a hybrid vehicle setting. Nonetheless, this topology is unsuitable in high-power contexts since high-voltage spikes on secondary switches during switching. In order to implement in high-power applications, some researchers propose improved typologies to reduce the voltage stress such as adding a RDC snubber circuit or an energy recovery snubber into the current-fed side[12].

Fig.2.1b illustrates another widely used IBDC that evolved from half bridge IUDCS, which consists of fewer devices and achieves higher power ratings. As the primary side switches can act as active clamp switches, adding an additional voltage-clamping circuit is unnecessary to suppress voltage stress[13].

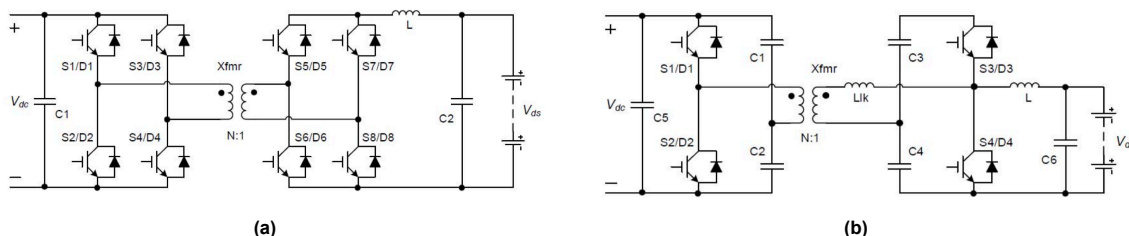


Figure 2.1: IBDC topology (a) Full bridge IBDC topology (b) Half bridge IBDC topology [14]

2.1.1. DAB and DAHB

Dual active bridge (see Fig.2.2a and Fig.2.2b) is another type of IBDC that is employed for various applications such as solid-state transformers in power grids, energy storage units, and onboard chargers for electric vehicles. due to the following reasons[15]:

- 1) Capability of auto-adjust bidirectional power flow, able to respond to fast changes on source and load in microgrids.
- 2) Zero voltage switching (ZVS) can be realized for switches within both bridge.
- 3) The extensive voltage conversion gain span makes it well-suited for linking with energy storage systems

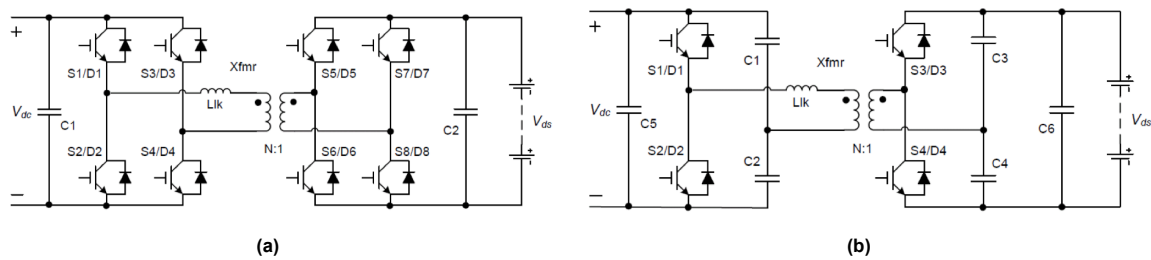


Figure 2.2: Dual active bridge converter topology (a) Full bridge topology (b) Half bridge topology[14]

It has been demonstrated that DAB can provide high power conversion efficiency in academic settings. However, conventional DABs did not develop rapidly since the voltage conversion ratio and the transferred power heavily affect the switching and conduction losses of the DAB. Furthermore, in instances of light loads, the potential inadequacy of leakage inductance to sufficiently discharge the capacitance can lead to a scenario of hard switching, which reduces the efficiency of power conversion. With the development of GaN-based power devices, DAB-IBDC become much more feasible. [16] illustrated a 1000W, 400 V-to-12 V DAB prototype achieved 98.3% efficiency with GaN devices. [17] demonstrated 97.5% peak efficiency can be reached with a 1 MHz 1200W/400V DAB using Gallium Nitride (GaN) devices.

IBDCs come in diverse topological variations. In addition to the previously discussed type, it's also possible to combine multiple types to create integrated IBDCs. For example, a combination of a half-bridge IUDC and a push-pull IUDC is been implemented in high current and low voltage applications[16]. Nonetheless, this particular kind of converter could encounter issues with a notable voltage spike. One of the alternative solutions is to incorporate a clamp circuit to mitigate the voltage spike when the switch on the low-voltage side turns off. [18]also notes that the power flow characteristic of this type of IBDC is the same as conventional DAB, hence, the modulation strategy of traditional DABs can also be utilized.

2.1.2. Modulation strategies

Both DAB converters and DAHB converters prominently employ the Single-Phase-Shift (SPS) modulation strategy. To regulate both the amplitude and direction of power flux, management of the phase differential between the primary and secondary switch gate signals is employed. A significant advantage of SPS is its simplicity and ability to produce high-frequency transformer voltages through the utilization of half-bridge configurations. Nevertheless, it is worth noting that substantial deviations from the nominal operational point can give rise to a significant accumulation of reactive power within the high-frequency transformer, resulting in high conduction loss and low efficiency.

Hence, some researchers propose alternative modulation methods[19] and[20]. The manipulation of the phase shift between the switching legs of an H-bridge facilitates the generation of three-level transformer voltages with varied duty cycles. This alternative solution has a different work principle com-

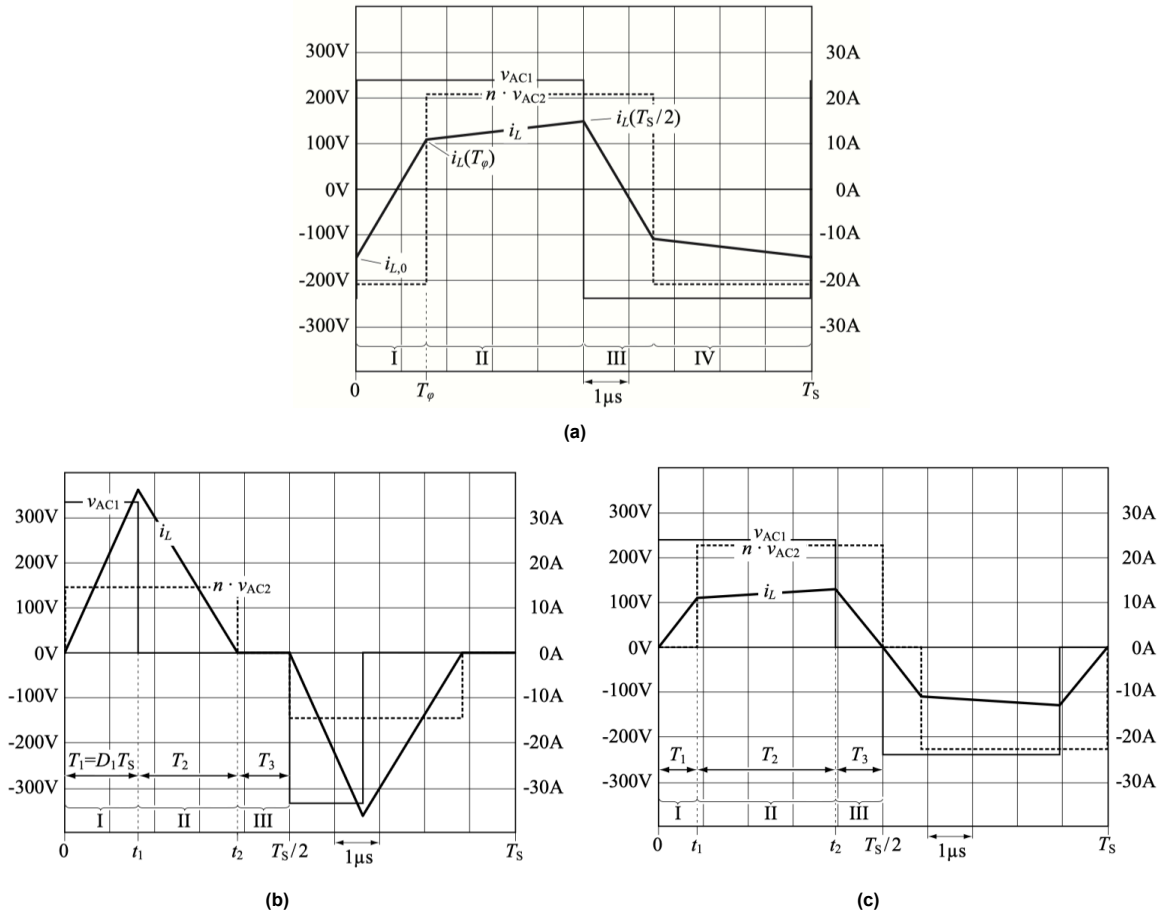


Figure 2.3: DAHB Modulation techniques (a) Single-Phase-Shift modulation (b) Triangular current phase shift modulation (c) Trapezoidal current phase shift mode modulation [19]

pared with SPS, decreasing transformer reactive power and curtailment of switching losses. Moreover, an arbitrary duty cycle introduces an extra dimension of control flexibility. According to the shape of the current flowing through the transformer, alternative modulation methods can be classified as triangular current mode phase shift modulation and trapezoidal current phase shift mode modulation. It should be noted that the SPS scheme and alternative modulations have similar conduction loss at rated power. When operating at a light power condition, alternative modulations significantly decrease switching losses due to the number of transistors involved in current switching.

Although alternative modulations can increase the overall efficiency, there are some limitations to implementation. The introduction of an additional circulating current leads to an augmentation in the RMS current of the transformer. Consequently, in cases where the conduction losses within the transformer are leading, there will result in a decline in efficiency. Another limitation is for half bridge IBDC since there are no H-bridges generating phase shifts between the switching legs. To broaden the realm of soft-switching for half-bridge IBDCs, adjustable switching frequency methods are proposed in [21]-[22]. In [21], a modulated technique with adjustable frequency based on the fixed ratio between the RMS and peak current is reported. However, the efficiency will reduce since it may result in a large amount of circulating current. To mitigate the RMS current of the transformer, an alternative modulated approach involving switching operations triggered at a predetermined current threshold is introduced [23]. Despite their ability to extend the ZVS range, these methodologies introduce intricacies in terms of both modeling and the execution of feedback mechanisms. [22] presents a hybrid control strategy that combines SPS and burst mode operation, which extends the ZVS range of switches and improves the efficiency under light load conditions as well.

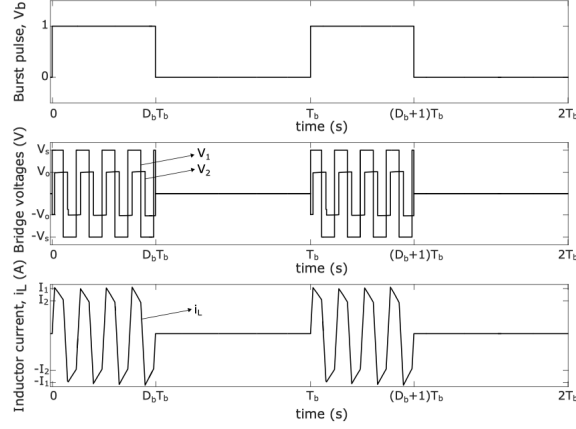


Figure 2.4: Waveforms of a DAB converter within the burst mode operation[22]

The waveforms of an ideal DAB converter within the burst mode operation are depicted in Fig.2.4. This allows DAB power output to be controlled using an additional degree of freedom by burst duty ratio. In fact, burst mode and phase-shift hybrid control have been used for LLC converters to extend ZVS range[24], but for DAB converters, researchers proposed the concept of phase shift control mode with a constant burst duty ratio, while concurrently suggesting the implementation of a burst duty control mode with a steady phase shift[22]. However, the utilization of dynamic burst mode in conjunction with phase shift control remains unexplored thus far.

2.1.3. State space modeling

The state-space averaging methodology is indeed widely used for modeling and designing converter controllers. It provides a convenient method for analyzing converter steady-state and dynamic behavior.

Different operating modes are divided into the converter in state-space averaging. The converter acts as a linear system during each subinterval of the switching cycle. It is thus thought of as a variable structure system with linear nonlinear equations in the state space. In each subinterval, the linear and time-invariant state space equations are represented as follows[25]:

$$\begin{aligned} \dot{x} &= A_I x + B_{II} u; y = C_I x + D_{II} u; 0 < t < dT \\ \dot{x} &= A_{II} x + B_{II} u; y = C_{II} x + D_{II} u; dT < t < T \end{aligned} \quad (2.1)$$

Here, x denotes the system's state vector, u signifies the vector encompassing independent inputs, and y represents the output. and A_j, B_j, C_j and D_j are state space matrices in sub-interval j . Considering the weight of the sub-interval associated with each, the averaged state space equation is derived.

$$\begin{aligned} \dot{x}_{avg} &= A_{avg} x + B_{avg} u \\ y_{avg} &= C_{avg} x + D_{avg} u \end{aligned} \quad (2.2)$$

where $A_{avg} = A_I d + A_{II}(1 - d)$, $B_{avg} = B_I d + B_{II}(1 - d)$, $C_{avg} = C_I d + C_{II}(1 - d)$ and $D_{avg} = D_I d + D_{II}(1 - d)$

Once the averaging equations are derived, small signal perturbations are introduced. X, Y, U , and D represent steady-state values and the terms $\tilde{x}, \tilde{y}, \tilde{u}$ and \tilde{d} are small signal perturbations. Substitute (2.3) into (2.2) and rearrange these terms as (2.4) and (2.5).

$$\begin{aligned} x &= X + \tilde{x} \\ y &= Y + \tilde{y} \\ u &= U + \tilde{u} \\ d &= D + \tilde{d} \end{aligned} \quad (2.3)$$

$$\begin{aligned} \tilde{\dot{x}} &= A_{avg}X + B_{avg}U \\ &+ A_{avg}\tilde{x} + B_{avg}\tilde{u} + [(A_I - A_{II})X + (B_I - B_{II})U]\tilde{d} + [(A_I - A_{II})\tilde{x} + (B_I - B_{II})\tilde{u}]\tilde{d} \end{aligned} \quad (2.4)$$

$$\begin{aligned} Y + \tilde{y} &= C_{avg}X + D_{avg}U \\ &+ C_{avg}\tilde{x} + D_{avg}\tilde{u} + [(C_I - C_{II})X + (D_I - D_{II})U]\tilde{d} + [(C_I - C_{II})\tilde{x} + (D_I - D_{II})\tilde{u}]\tilde{d} \end{aligned} \quad (2.5)$$

Considering the derivation of the steady state is zero and neglects higher order terms of (2.4) and (2.5), The obtained linearized small-signal state-space averaged model is as follows:

$$\begin{aligned} \tilde{\dot{x}} &= A_{avg}\tilde{x} + B_{avg}\tilde{u} + [(A_I - A_{II})X + (B_I - B_{II})U]\tilde{d} \\ \tilde{y} &= C_{avg}\tilde{x} + D_{avg}\tilde{u} + [(C_I - C_{II})X + (D_I - D_{II})U]\tilde{d} \end{aligned} \quad (2.6)$$

The duty cycle \tilde{d} to output \tilde{y} transfer functions can be obtained considering $\tilde{u} = 0$.

$$\frac{\tilde{y}(s)}{\tilde{d}(s)} = C_{avg}[sI - A_{avg}]^{-1}[(A_I - A_{II})X + (B_I - B_{II})U] + [(C_I - C_{II})X + (D_I - D_{II})U] \quad (2.7)$$

The input \tilde{u} to output \tilde{y} is derived considering $\tilde{d} = 0$.

$$\frac{\tilde{y}(s)}{\tilde{u}(s)} = C_{avg}[sI - A_{avg}]^{-1}B_{avg} + D_{avg} \quad (2.8)$$

2.1.4. Developing modeling of a DAHB

This phenomenon can be attributed to the null average of the transformer current. Similar to other slow system states, the AC signal contains a gradual-moving average, which ultimately attenuates to zero in a stabilized state. As a result of transient oscillations, capacitors will charge and discharge and the system possibly compelling the system to engage in hard switching mode, as discussed in [26]. Consequently, the conventional approach of state-space averaging modeling encounters inapplicability, given the zero average currents in a steady state. Thus, some developing existing modeling methods have been summarized.

1) **Reduced Order Modelling** Use the two-sided voltage of the transformer to represent the leakage inductor current. Then, the average model can be simplified without inductor current[27]-[28].

2) **Generalized Average Modelling** To indicate the intricacies of the current dynamics of the transformer series inductor, [29] employs the switching frequency components within the Fourier series of state variables. This method effectively illustrates the influence of the purely AC part of the inductor current, while both the real and imaginary components elevate the model's complexity.

3) **Discrete-Time Modelling** High-frequency dynamics are included in the discrete-time model for DAB[29]. A presumption is made that state variables are adjustable only at distinct temporal junctures. With discrete-time models, accurate models can be obtained, yet the trade-off resides in their inherent computational intricacy.

The aforementioned three modeling methodologies are simulated as detailed in [11] and summarized in Fig.2.5. The other two methods showcase great accuracy except for the generalized average modeling. The reduced-order model[28] is simplified to implementation and is recommended for the design of closed-loop controllers.

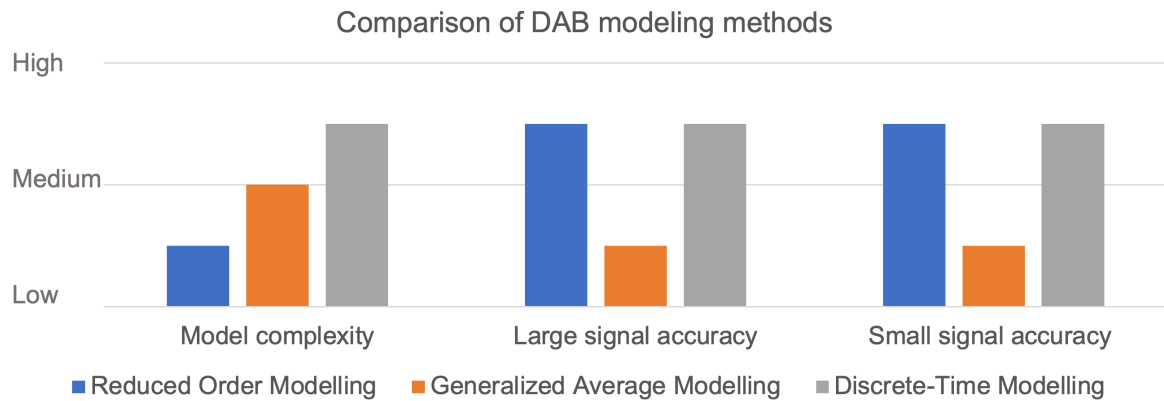


Figure 2.5: Comparison of DAB modeling methods

2.1.5. Control of a DAHB

To regulate output DC voltage, the control methods should be implemented. Since amount analysis [15]-[30] indicates that the DAB converter is a first-order system, feedback control with a proportional-integral (PI) compensator seems a candidate solution to regular the output voltage [30]. Another method uses an estimated phase-shift ratio and actual phase-shift modulating by a PI controller as the set point for the phase is presented [28] however, this method is sensitive for a load since the estimated phase-shift ratio is calculated by the load approximately resistance. Thus, an extra current sensor is needed when implementing variable load. In addition to this, other control methods developed in [29] and [29] are compared in terms of complexity, dynamic behavior, robustness, and the incurred costs of implementation, as indicated in Fig.2.6.

- **Linearization control:** Non-linear terms in DAB can be eliminated by linearizing the control. In addition to reducing sensitivity to load conditions and the reference voltage, the control can also increase stable margins. Nevertheless, in the case of a feedback-only control approach, the necessity for linearization might be obviated, provided that the output impedance and the closed-loop bandwidth exhibit consistency across varying output voltages or load scenarios.
- **Feedforward plus feedback control** It is a method combining feedforward and feedback to improve performance that can overcome the parameter sensitivity problem under unknown parameters, but its performance quickly deteriorates. In addition, under light loads, the loop gain is too low.
- **Disturbance observer-based control (DOBC)** Using the estimate generated by the observer, DOBC generates compensating total disturbances and uncertainties. As opposed to feedback-only control, DOBC has better load disturbance rejection capabilities and is insensitive to parameter variations. However, physical sensors increase cost while software sensors provide an online estimate of the unmeasured system state variable also affects accuracy.
- **Current mode control** In order to improve dynamic performance and limit the maximum transformer current, the transformer current is used in the feedforward current control. As with other peak current controls, the control is susceptible to noise. Predictive current control is another current control, but implementing DAB is a challenge since DAB converters have a wide range switching frequency.
- **Sliding mode control** A prominent benefit of employing SMC lies in its assurance of stability and resilience against uncertainties in parameters. Nevertheless, the efficacy of SMC diminishes when the implementation of an equivalent control action is undertaken.
- **Predictive control** This approach enhances dynamic performance, yet it comes with drawbacks such as large computational demands, elevated implementation expenses, and heightened intricacy.

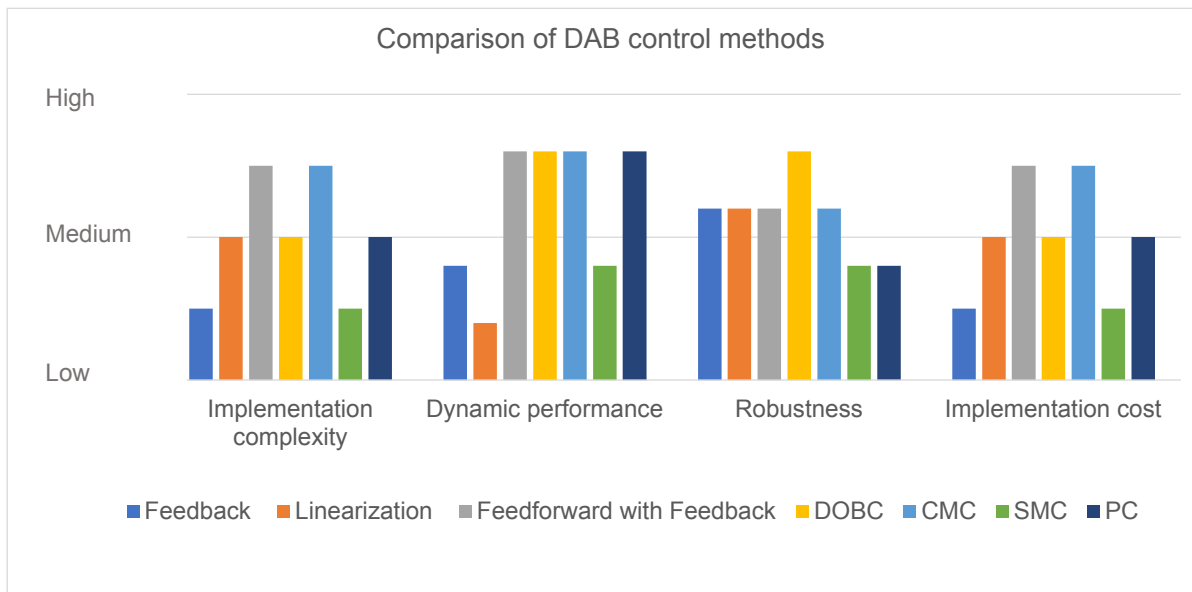


Figure 2.6: Comparison of DAB control methods

2.2. PV-based DC microgrid

2.2.1. Solar home System

Increasing the electrification ratio in rural areas can present unique challenges, particularly when it comes to grid expansion. Traditional expansion of the grid infrastructure may not be economically viable in regions with low and dispersed load requirements. This limitation has opened opportunities for renewable energy sources to play an important role in rural electrification, not only addressing energy needs but also contributing to international carbon emission targets.

In rural areas of Africa where the grid infrastructure may be limited or nonexistent, off-grid solar photovoltaic (PV) systems have become a popular choice for rural electrification. It offers several advantages, including increased energy efficiency, reduced transmission and distribution losses, and improved reliability.

Solar PV applications in rural areas can be categorized into decentralized and centralized solutions. Decentralized applications Solar Home Systems (SHS) typically consist of a photovoltaic module, a battery system for energy storage, and a charge controller to regulate the energy flow between the photovoltaic module, the battery, and the loads[31]. When exposed to sunlight, the PV module generates electricity, generating electrons that can be used by the connected loads. Excess power generated during periods of high solar irradiation can be stored in the battery system for later use when demand exceeds the available solar power. The size of the PV module is highly dependent on the total amount of energy needed by the PV generator. The general SHS topology is illustrated in Fig.2.7.

2.2.2. DC microgrid

Utility-interactive electrification

It should be noted that standalone SHSs are typically designed based on the lowest average peak sun hours per day, they are intended to provide enough power to meet the load requirements even under unfavorable sunlight conditions. However, when the sun intensity exceeds the lowest average value, the SHS generates more energy than can be stored within its designed system. This excess energy can be effectively utilized by implementing a utility-interactive electrification concept, which allows for the sharing of power between houses[32]. Instead of storing the surplus energy locally, it can be transmitted

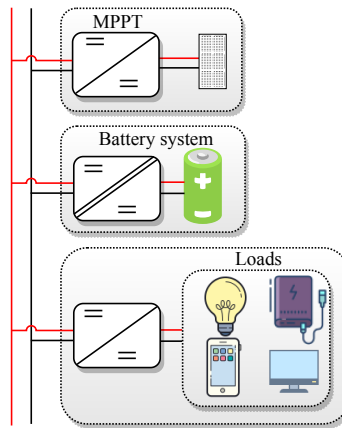


Figure 2.7: SHS consists of a single PV, MPPT converter, battery, and loads

to nearby homes, benefiting multiple households.

By interconnecting SHS and creating a shared power grid, the excess energy generated by one system can be utilized by another system or distributed among multiple homes. This approach helps optimize energy utilization, reduces the wastage of surplus power, promotes more efficient use of renewable energy resources, and supports small industrial appliances encouraging local commercial development. There are two common topologies. As depicted in Fig.2.8a, one configuration entails each SHS being linked to a shared public bus. Conversely, Fig.2.8b portrays a distinct point-to-point type interconnection scheme.[33].

From a comprehensive evaluation of total cost and efficiency, it is observed that in Fig.2.8a, the preferred topology is characterized by requiring the fewest number of converters and connections. This topology offers advantages in terms of cost reduction and improved overall efficiency. On the other hand, although the system in Fig.2.8b exhibits more robustness with its highly meshed structure, at the expense of increased converter count and reduced cost savings.

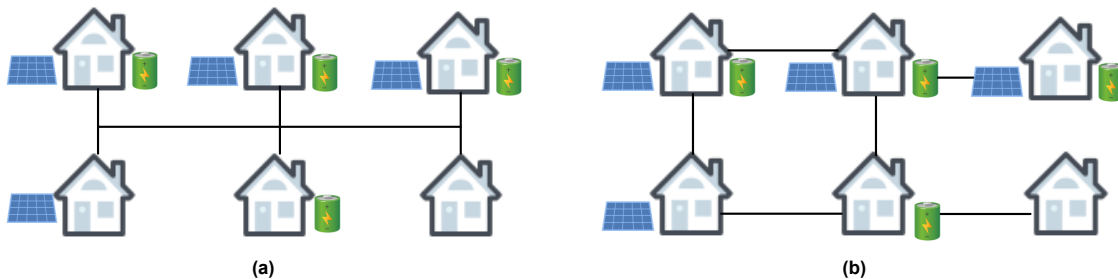


Figure 2.8: Common topologies used for power sharing grid (a)Point sharing (b) Point-to-point sharing

Low Voltage Direct Current Distribution Network

To enhance the stability of the utility-interactive system and facilitate power exchange between the grid and users, the implementation of a Low Voltage Direct Current Distribution Network (LVDCDN) is proposed[34]-[35]. The LVDCDN plays a crucial role in realizing efficient and reliable electricity distribution, particularly in rural areas, thereby increasing the electrification ratio.

The LVDCDN operates on a low-voltage DC distribution platform, which has lower conversion losses, high power quality, and enhanced compatibility with renewable energy sources such as solar photovoltaic systems. By integrating the SHS into the LVDCDN, users can both receive power from the grid when needed and contribute surplus power back to the grid when they have excess generation. This

two-direction power flow capability enables better utilization of distributed energy resources, reduces wastage, and enhances the overall efficiency of the system[36][11].

Moreover, the LVDCDN enhances the reliability and resilience of the utility-interactive system. It provides a decentralized distribution network that is less prone to single-point failures and cascading disruptions. The use of DC power distribution reduces the complexity of the system and improves fault detection and isolation capabilities, leading to quicker restoration of power in case of outages.

The LVDCDN can be implemented in two basic configurations: unipolar and bipolar[34]. Fig.2.9a illustrates there is only one voltage polarity throughout the distribution network. On the other hand, a bipolar system is composed of two interconnected unipolar systems as shown in Fig. 2.9b. Each unipolar system operates at a different voltage polarity, creating a series of connections between the positive and negative poles.

The advantages of bipolar systems are summarized as follows[37][38]:

- It offers three different voltage levels, positive to neutral, negative to neutral, and positive to negative.
- A highly reliable power supply is achieved by distributing the load-side converters evenly. This configuration remains unaffected by instantaneous short or long-term overload.
- DC distribution systems are suitable for DGs with DC outputs and energy storage systems. System efficiency increases if the load requires DC power.
- This system can maintain a continuous supply of electric power even in the event of an accident within the utility grid. Reconnecting to the utility grid is also seamless.

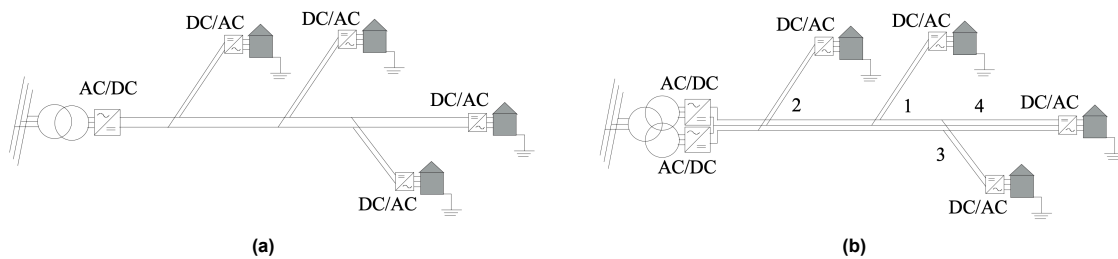


Figure 2.9: Example of LVDC distribution system: (a)an unipolar LVDC distribution system (b) a bipolar LVDC distribution system[35]

There is a need for DC voltage balance control when there is a large difference between two line voltages. A voltage balancing converter is introduced in [37]. In general, it can be put on source side or load side. A buck-boost-type voltage balancer is the most commonly used type, which regulates inductor current to charge and discharge two capacitances[39].

To reduce power devices' voltage stress and avoid the shoot-through problem, several alternative voltage balancer configurations have been proposed, including the dual-buck half-bridge circuit[40], three-level circuit[41], and other converters summarized in [42]. These topologies, however, necessitate significant filtering capacitance to filter current oscillation. Consequently, to mitigate this issue, it has been recommended to employ multiple voltage balancers operating in an interleaved manner. This approach leads to smoother output current and significantly reduces the required capacitance. Nevertheless, it is worth noting that all of these voltage balancers introduce additional circuitry, resulting in extra semiconductor components, increased power losses, elevated costs, and heightened complexity.

2.2.3. Decentralized control

Various strategies can be employed to regulate essential aspects of DC systems. In decentralized control, individual converters independently determine their actions without engaging in communication with other devices.

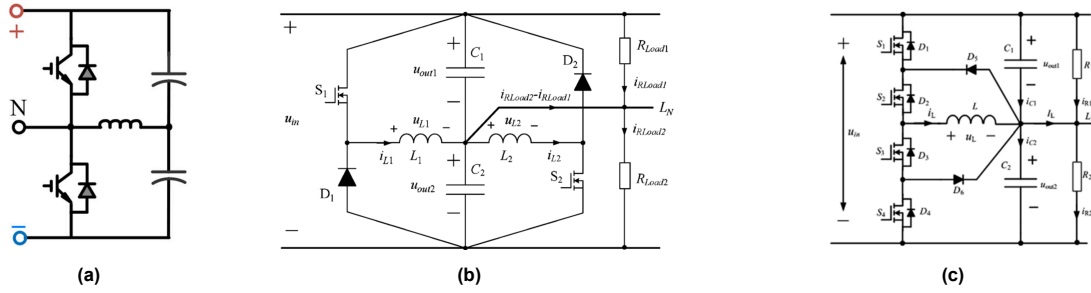


Figure 2.10: Voltage balancing converter(a)Buck-boost topology[39] (b)Dual-Buck Half-Bridge topology [40] (c)Three-level topology[41]

In the context of DC distribution systems, a hierarchical control scheme is commonly used. Fig.2.11 illustrates the typical layers comprising a hierarchical control system. The initial layer, referred to as the physical layer, encompasses converters, distribution lines, and other network components. The subsequent layer, known as decentralized control, relies solely on locally accessible information. The third layer, coordinated control, involves control schemes that employ communication to facilitate functionalities such as power sharing and stability. Lastly, the management focuses also on complex auxiliary goals such as power flow control. A low-voltage optimal regulation can be achieved with this scheme, but it also increases the cost due to coordinated control and management.

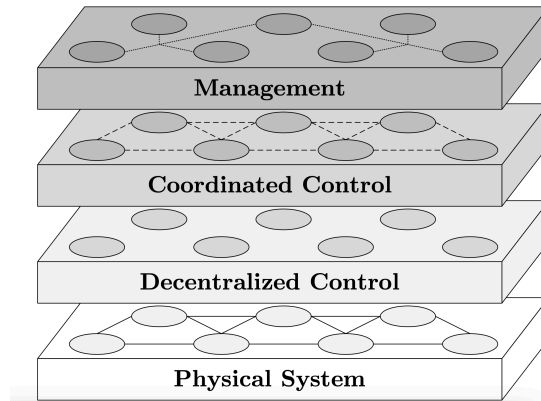


Figure 2.11: System hierarchical control structures[43]

Droop control

Droop-based control is one of the decentralized strategies. A buffer between the rated working state and the closed state can be guaranteed with droop control[43]. In an islanded DC Microgrid with a limited number of components, the primary focus is on power balancing, achieved through appropriate voltage regulation. Fig.2.12 shows an example of controlling the full operation range of a storage system, including current limit, constant power, and droop control without the converter.

Droop control aims to reduce the output voltage of converters as the current increases, thereby introducing a resistive characteristic to the system. In [44], a physical impedance is used as the droop resistance, however, this approach involves the use of a filter, which results in higher power losses and increased investment costs. As an alternative, virtual resistance is often employed. By incorporating an additional virtual loop, power converters can effectively emulate the characteristics of a real inductor or filter, offering a more efficient and cost-effective solution.

$$V_{out} = V_0 - I_{out} \times R_{droop} \tag{2.9}$$

Where V_{out} , I_{out} , and V_0 are the converter reference output voltage, converter current output, and nominal voltage. System voltage is maintained within the specified value by adjusting the droop control parameters.

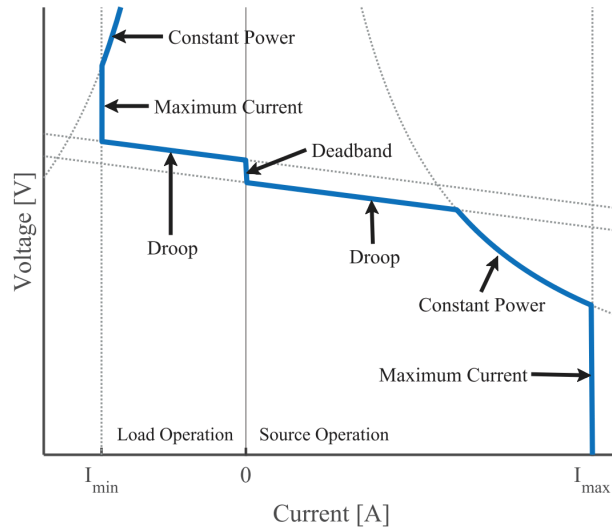


Figure 2.12: Possible current-voltage characteristic for the local control of a storage converter[45]

MPPT converter

In PV power systems, maximum power point trackers (MPPTs) are important because they can ensure converter work at the highest efficiency. A number of MPPT algorithms have been proposed, and their performance is qualified by the MPPT efficiency and implementation complexity[46]. Fig.2.13 shows the comparison of MPPT algorithms.

- **Perturb and Observe (P&O) Algorithm:** The P&O method is frequently employed in practical applications due to its straightforward implementation. Nonetheless, it can become unpredictable if there are sudden changes in light conditions.
- **Incremental Conductance:** Calculating the appropriate direction to perturb the operating point of the PV array to reach maximum power is provided by the system. In addition, it reduces oscillation around the MPP in rapidly changing conditions. Nevertheless, its implementation can be more intricate.
- **Constant Voltage Control:** While the application of this technique is uncomplicated, its effectiveness is relatively modest in contrast to alternative approaches. Measuring the V_{max} and V_{oc} of the PV array is essential, but disconnecting the PV for V_{oc} assessment can lead to diminished tracking efficiency.
- **Parasitic Capacitance:** While model-based MPPT approaches may appear promising, they are typically impractical due to uncertainties associated with the precise values of cell parameters. These parameters can vary significantly even among cells produced in the same manufacturing run. In addition, this scheme is economically unfeasible due to the high cost and accuracy of the light sensors involved.

Battery converter

This adjustment serves to maintain the stability and optimal operation of the system. Some authors proposed stored energy by adjusting the virtual resistance in droop controllers, however, centralized supervisory control is required[47]. An adjustable droop method is introduced for a decentralized system.[48]. However, the strategy only discusses the scenario that batteries are in discharging mode. [49] proposed a fuzzy logic to adjust the droop resistor of converters, however, it only considers one voltage level. In [50], an adjustable droop method is designed for a multiple-voltage level DC microgrid. Virtual resistance adjustments were utilized to enable the passive transmission of voltage-based information within the SHS and the microgrid.

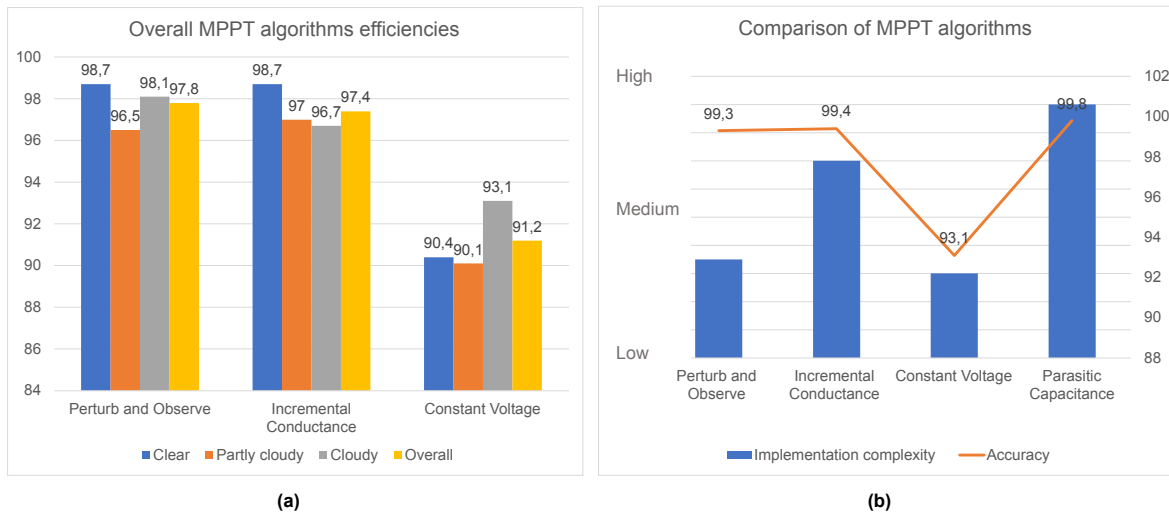


Figure 2.13: Comparison of MPPT algorithms (a) Efficiencies under different sky conditions (b) Accuracy and implementation complexity[35]

The modeling of DC microgrids in simulation

To enable real-time energy harvesting of a PV system, a Simulink PV array model is integrated into the DC microgrid. The incorporation of series-connected PV panels generates higher voltage, while parallel-connected PV panels produce higher current[51]. Consequently, the PV array can be appropriately sized to meet the total power demand based on the load requirements.

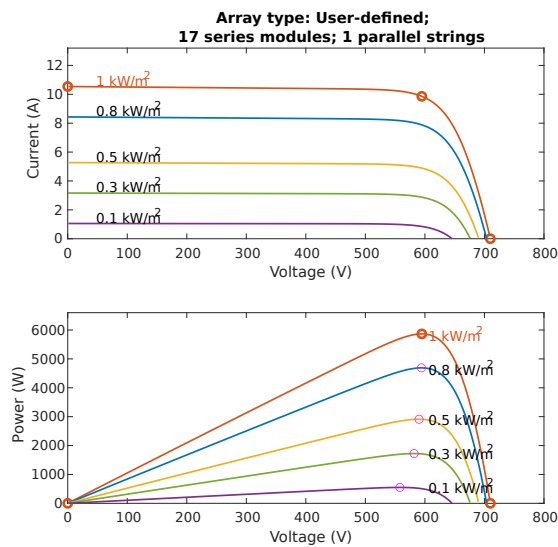


Figure 2.14: P-V and I-V curves of an ideal PV panel

The battery block in Matlab/Simulink is a widely used representation of various rechargeable battery types in a generic dynamic model. The State of Charge (SoC) indicates the usable capacity and is commonly expressed as a percentage (0% = empty; 100% = full). And the estimation of SoC is critical for taking different actions such as charging and discharging. It's important to note that battery voltage fluctuates depending on the SoC, thus, SoC can be estimated based on V_{oc} . Fig.2.15 shows the influence of the two factors mentioned.

Grid impedance is a crucial element in grid modeling, as it plays a significant role in enhancing con-

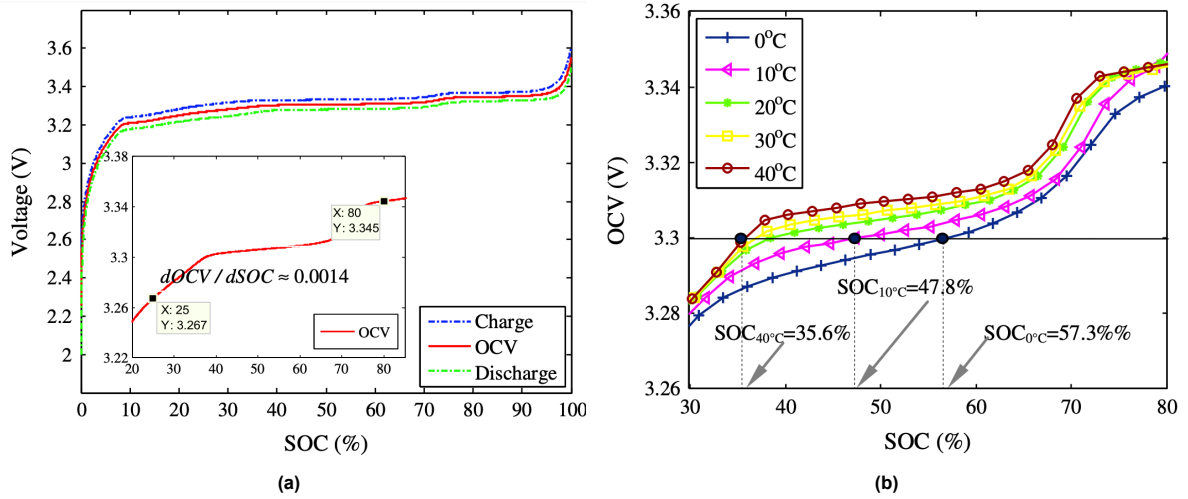


Figure 2.15: OCV Vs.Soc(a)The effect of Soc on Voc (b) The effect of temperature on Voc [52]

troller stability and protection. The analysis of transmission and distribution lines commonly involves the incorporation of electromagnetic properties that govern their behavior. Lumped element models, depicted in Fig.2.16, are frequently utilized to represent these lines. Despite the distribution of passive components along lines, this simplification satisfies accuracy when the wavelength of the signal is greater than the length of the line.

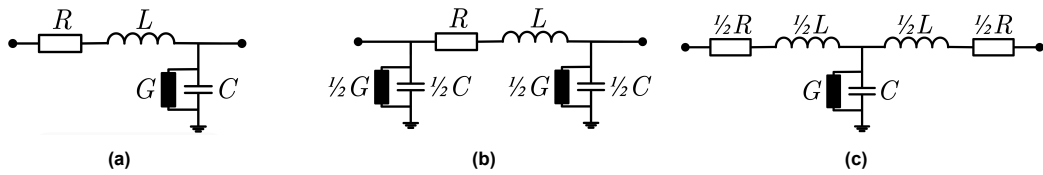


Figure 2.16: Lumped element models for a line (a) Gamma model (b) Pi model (c) T model[43]

It is worth noting that the models presented in Fig.2.16 pertain to a unipolar DC system. Due to their tendency to induce corrosion, DC ground currents are generally discouraged. Conversely, in situations involving multiple conductors, mutual couplings emerge between them, manifesting as mutual inductance, conductance, and capacitance. These interconnected influences can substantially impact the system's performance. Fig.2.17 illustrates an example of a bipolar system that incorporates above mentioned mutual couplings.

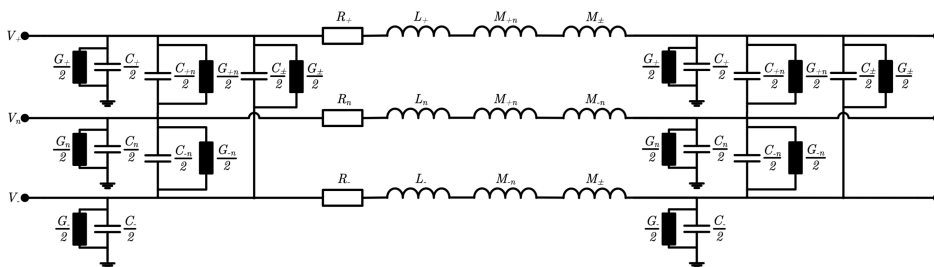


Figure 2.17: Bipolar system line impedance model[43]

3

Modeling of Dual-Active-Half-Bridge DC/DC Converter

3.1. Overview

In this chapter, the mathematical model of a dual-active-half-bridge converter's steady-state and dynamic behavior is fully examined. The values of the components used in the modeling and simulation are carefully chosen to correlate with those seen in actual converters to guarantee the correctness and dependability of our study. Additionally, the closed system's stability is evaluated using a zero-pole map, and the PI controller's settings are adjusted depending on the bode plot. Additionally, we examine the effects of the clamping circuits and determine whether they can reduce output current peaks. Finally, we go through the requirements for preserving Zero Voltage Switching (ZVS), a crucial aspect of the converter's functionality.

3.2. Topology

3.2.1. Comparison with a conventional DAB converter

The DAHB configuration has the ability to facilitate bidirectional power flow, making it a common choice for grid interfaces where both sides require energy access. However, the traditional implementation of the DAHB converter faces inefficiency due to the lengthy reverse recovery times demanded by Si MOSFET devices. Consequently, this results in extended switching periods and heightened switching losses. Additionally, while symmetrical DAHB converters excel in high-voltage applications, they prove less suitable than push-pull converters in situations involving low voltage, such as driving SHS. To address these challenges, a modified DAHB topology that combines the strengths of both aforementioned converter types has been devised to enhance energy access capabilities.

The advantages of the proposed modified DAB topology are summarized:

- 1) The structure is simplified, and the number of switches is reduced owing to the half-bridge.
- 2) The transformer turns ratio is reduced since the half-bridge doubles the voltage of the transformer winding
- 3) Withstand low voltage and high current since the push-pull converter realizes the current shunting.
- 4) Low switching and conduction losses improve efficiency. On the one hand, GaN devices decrease

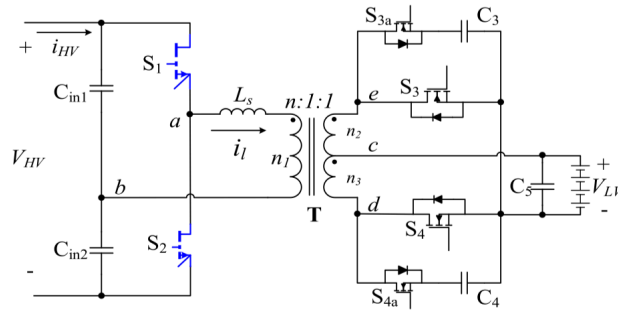


Figure 3.1: A modified DAB topology used in energy access[16]

the switching loss due to there being no reverse recovery charge.

3.2.2. Active clamp circuit

Nonetheless, during the dead time of the secondary side switches, the energy stored in L_{s2} gets transferred to charge the output capacitance, leading to a voltage spike. To mitigate this, an active clamp circuit is implemented to resonate with L_{s2} and curtail the voltage spike. Another benefit is that the active clamping circuit curbs the MOSFET turn-off current by injecting reverse current into the main switches.

Figs.3.2 and 3.1 and illustrate the operation of the active clamp. In the dead time of the secondary side switches when S3 and S4 are off, the secondary leakage inductance charges C3 through S3a's body diode. Once the capacitance voltage reaches the low voltage V_{LV} , the charge ends. C3 remains constant following the activation of S4. Upon turning on S3a, the current in L_{s2} is reflected in L_{s3} , which is opposite to the i_4 , making S4 turn-off less current intensive.

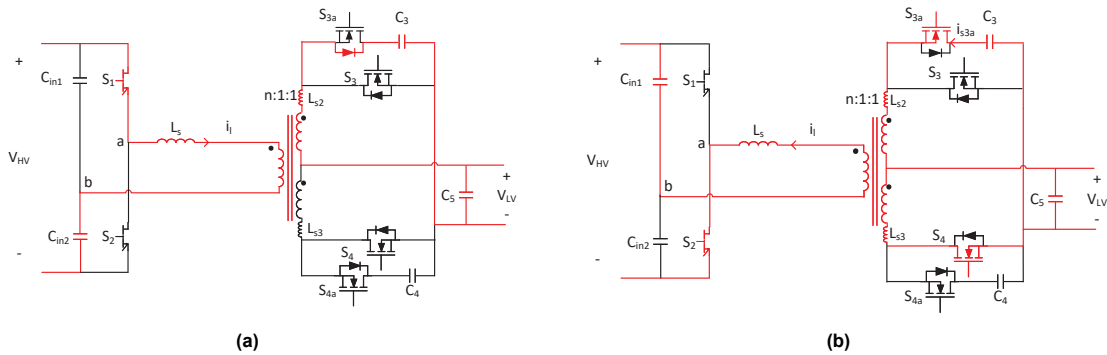


Figure 3.2: Equivalent circuit of the active damping circuit (a) First operation of active damping circuit (b) Second operation of active damping circuit

From KCL and KVL, the current and voltage relation is obtained

$$\begin{aligned} i_{Ls2} &= i_{s3a} = i_{C3} \\ V_{Ls2} &= V_{s3a} - V_{C3} - V_{LV} - V_{transformer,sec} \\ V_{t,sec} &= V_{LV} \end{aligned} \quad (3.1)$$

Where $V_{t,sec}$ represents the voltage across the secondary transformer. Combining (3.1) and solving the differential equation by applying Euler's formula, the optimal t_{on} is $\pi/(2\omega)$ [16]. As mentioned before, the values used in the simulation correspond to those observed in actual converters, where the Leakage inductance is chosen as $0.4\mu H$, thus, turn-on time is $0.11\mu s$. A comparison in Fig.3.3c and Fig.3.3a illustrates that snubber significantly reduces the spike of turn-off current from 7.52A to 2.78A in charging mode. In discharging mode, Fig.3.3d and Fig.3.3b show the same results where the maximum current is decreased from 20.09A to 18.94A.

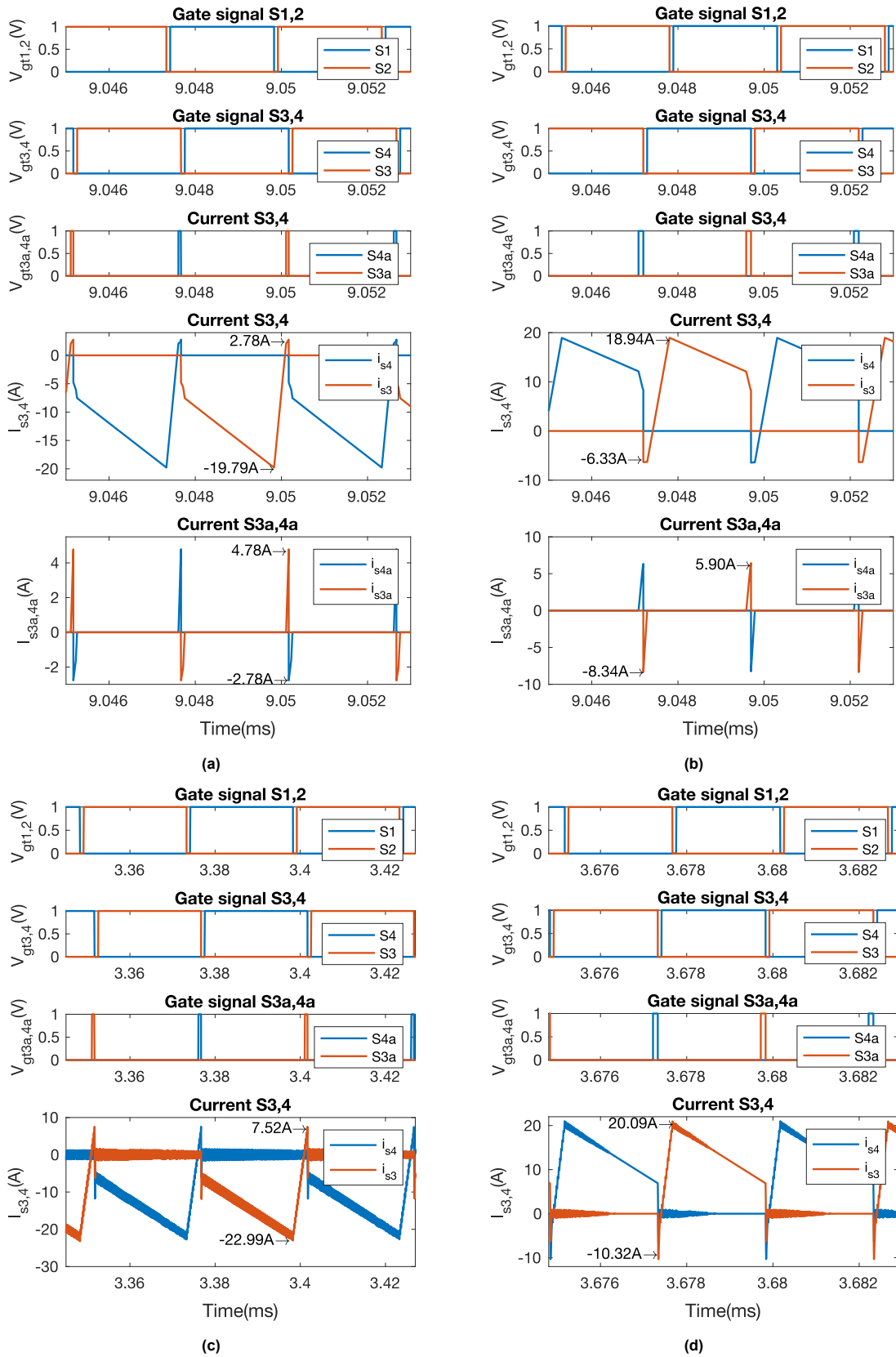


Figure 3.4: DAHB gate signal and output results (a)Charging mode without snubber (b)Discharging mode without snubber (c)Charging mode with snubber (d)Discharging mode with snubber

3.3. Power transfer Characteristics

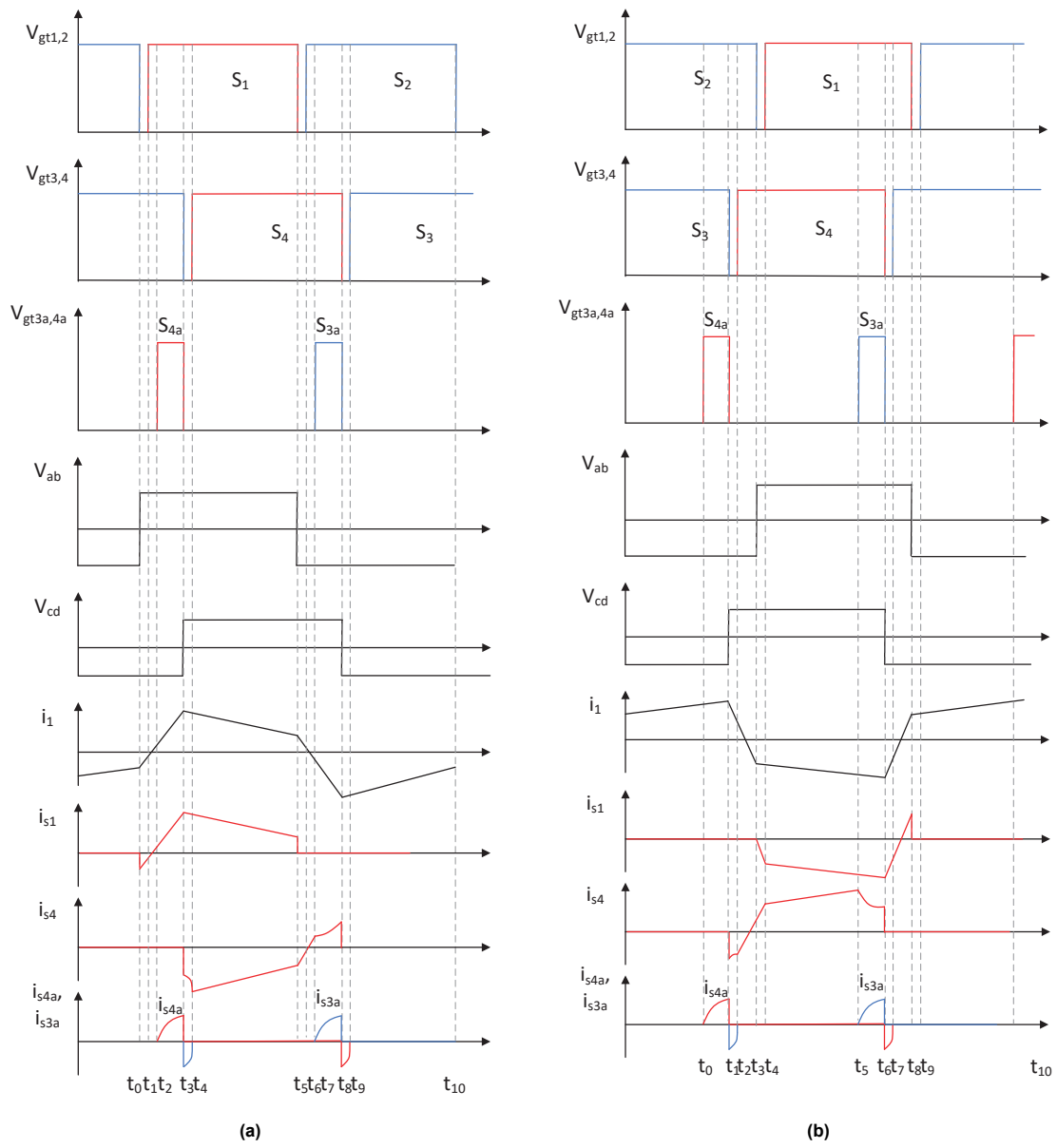
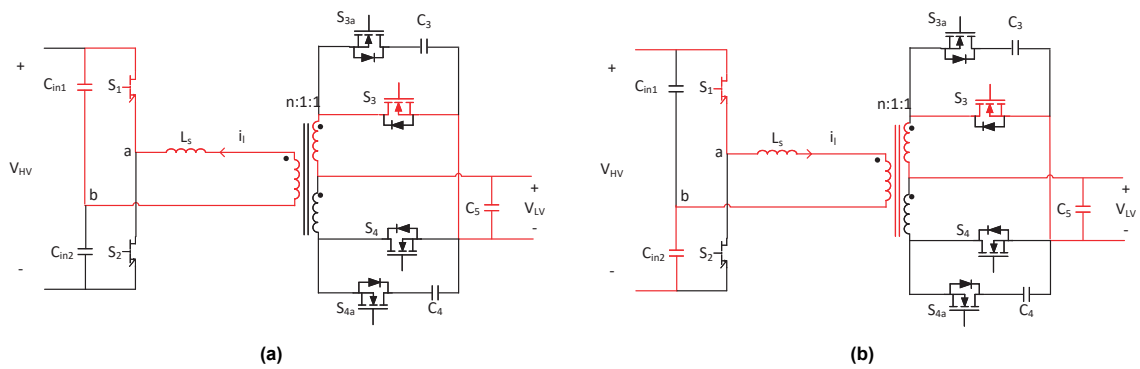


Figure 3.5: Theoretical waveforms of the converter (a) Charging mode waveforms (b) Discharging mode waveforms



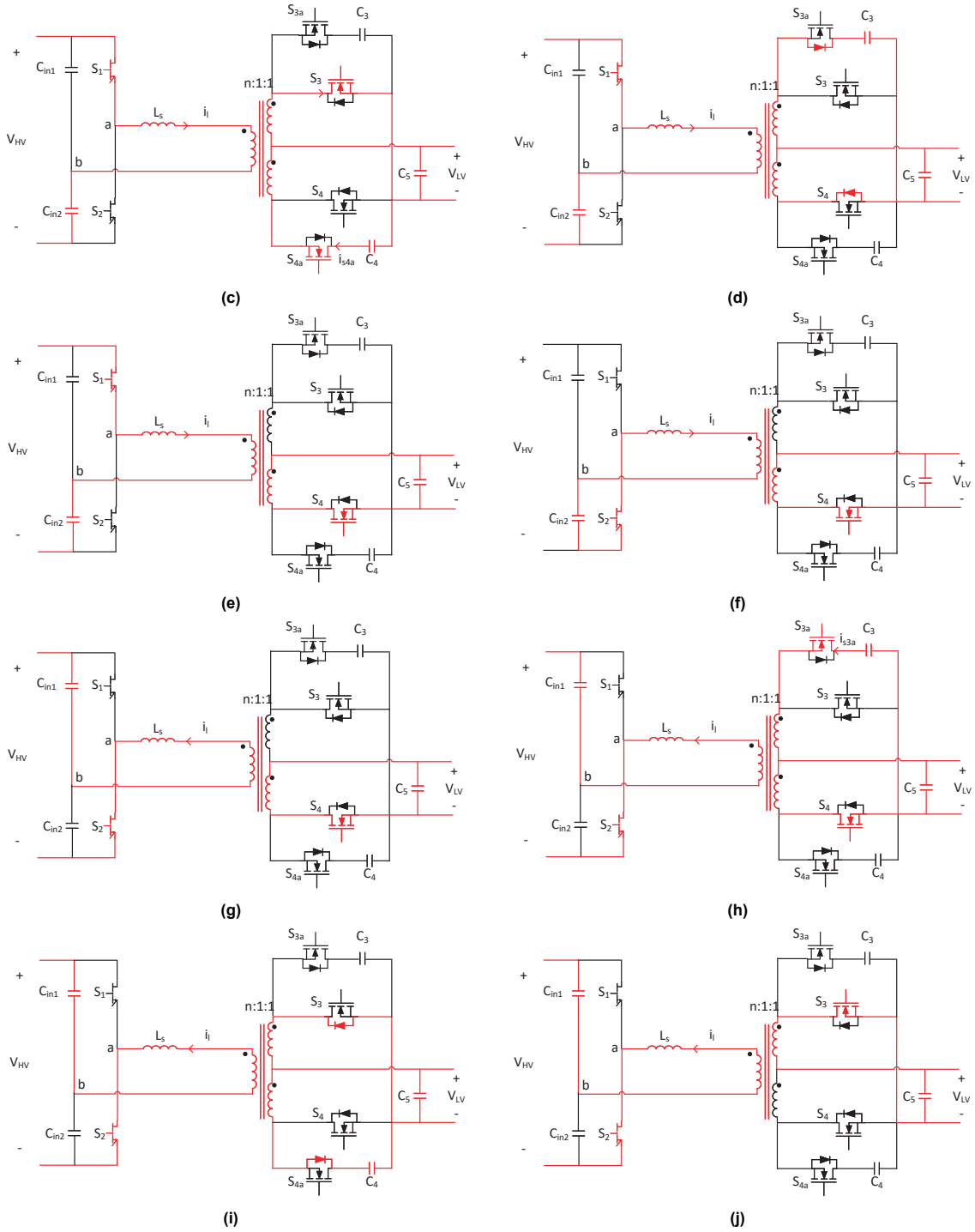


Figure 3.6: Equivalent circuit during various intervals (a) t_0-t_1 (b) t_1-t_2 (c) t_2-t_3 (d) t_3-t_4 (e) t_4-t_5 (f) t_5-t_6 (g) t_6-t_7 (h) t_7-t_8 (i) t_8-t_9 (j) t_9-t_{10}

3.3.1. Charging operation principles

The charging mode ideal waveforms are shown in Fig.3.5a. The first interval is from t_0 to t_3 . The current in L_s can be calculated.

$$L_s \frac{di_l}{dt} = v_{ab} + v_{vd} \tag{3.2}$$

Where $v_{ab} = \frac{V_{HV}}{2}$ and $v_{cd} = nV_{LH}$, V_{HV} and V_{LH} are the high voltage and the low voltage, respectively. n is the transformer ratio and i_l is the current in L_s .

During t_3 to t_5 . The primary side voltage charges the leakage inductance, while the low side discharges it; thus, the current is

$$L_s \frac{di_l}{dt} = v_{ab} - v_{vd} \quad (3.3)$$

The direction of i_l during the third and fourth intervals is opposite to that in the first and second intervals, and this calculation is provided below.

$$L_s \frac{di_l}{dt} = -v_{ab} - v_{vd} \quad (3.4)$$

$$L_s \frac{di_l}{dt} = -v_{ab} + v_{vd} \quad (3.5)$$

Fig.3.6 illustrates the conduction of the switches in each subinterval, and the analysis is as follows.

- **Subinterval t_0 - t_1 :** S2 turns off at t_0 . Since the GaN device can operate as a diode due to the symmetric structure, L_s discharges the capacitance C_{s1} .
- **Subinterval t_1 - t_2 :** At t_1 , S1 turns on in ZVS. The voltage across leakage inductance remains, hence, (3.2) still holds. The same result can be found in Fig.3.1, where the slope of leakage current is unchanged at t_1 .
- **Subinterval t_2 - t_3 :** Activation of S4a occurs before S3 turns off. Snubber capacitance C_4 will resonate with L_{s2} . As a result, this resonance current is reflected to the main switch S3 by the transformer, thereby reducing the turn-off current. (3.2) holds good for leakage inductance.
- **Subinterval t_3 - t_4 :** S3 goes into the dead zone of the secondary side switch, and S3a's body diode automatically illuminates. C_3 is charged by the L_{s2} . The resonant subinterval will end until the capacitor voltage equals V_{LV} .
- **Subinterval t_4 - t_5 :** S4 turns on in ZVS, transfers the secondary leakage inductance to the primary side, and the current flow through leakage inductance can be calculated as (3.3).
- **Subinterval t_5 - t_6 :** the negative half-cycle starts at t_5 . The energy stored in leakage inductance L_s discharge the capacitance C_{s2} . The leakage inductance current can be calculated as
- **Subinterval t_6 - t_7 :** S2 activates with ZVS. Despite this, V_{L_s} persists, ensuring that (3.4) remains applicable.
- **Subinterval t_7 - t_8 :** S3a turns on at t_7 , and C_4 resonates with the secondary leakage inductance of the transformer generating a resonance current. Due to the transformer, the resonance current will be transferred to the S4, thus, the turn-odd current of S4 is decreased.
- **Subinterval t_8 - t_9 :** The body diode of S4a activities. L_{s3} charges C_4 through S4a. The leakage inductance current can be calculated as (3.5).
- **Subinterval t_9 - t_{10} :** S3 turns on in ZVS, i_{L_s} remains the same result as (3.5).

3.3.2. Discharging operation principles

The discharge mode is shown in Fig.3.5b. The work principles are similar to the previously mentioned charging mode. Subinterval 1:

$$L_s \frac{di_l}{dt} = -v_{ab} - v_{cd} \quad (3.6)$$

Subinterval 2:

$$L_s \frac{di_l}{dt} = -v_{ab} + v_{cd} \quad (3.7)$$

Subinterval 3:

$$L_s \frac{di_l}{dt} = v_{ab} + v_{cd} \quad (3.8)$$

Subinterval 4:

$$L_s \frac{di_l}{dt} = v_{ab} - v_{cd} \quad (3.9)$$

3.4. Steady-state analysis

3.4.1. boundary conditions

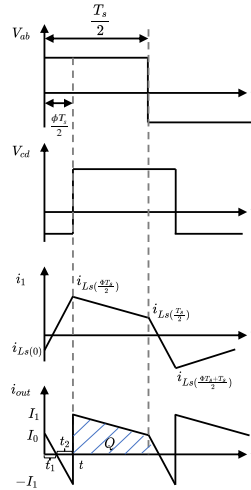


Figure 3.7: Operation modes of SPS control and output current

To simplify the calculation, substitute $\phi = \Phi/180$.

Taking charging mode as an example, ϕ is the phase shift and T_s is the switching period.

Referring to Fig.3.7, when the duty cycle of V_{ab} and V_{cd} is 50%, the initial states $I_{LS}(0)$, $I_{LS}(\frac{\phi T_s}{2})$, $I_{LS}(\frac{T_s}{2})$ and $I_{LS}(\frac{\phi T_s}{2} + \frac{T_s}{2})$ and during one complete switching cycle can be derived based on the boundary conditions

$$\begin{aligned} I_{LS}(0) &= -I_{LS}(\frac{T_s}{2}) \\ I_{LS}(\frac{\phi T_s}{2}) &= -I_{LS}(\frac{\phi T_s}{2} + \frac{T_s}{2}) \end{aligned} \quad (3.10)$$

3.4.2. Output characteristics

As mentioned above, both v_{ab} and v_{cd} refer to the primary side of the transformer; thus, the same slope as the leakage current can be defined.

$$\begin{aligned} I_0 &= t_1 \frac{V_{ab} + V_{cd}}{L_s} \\ I_1 &= t_2 \frac{V_{ab} + V_{cd}}{L_s} \\ I_1 + I_0 &= \frac{\phi T_s}{2} \frac{V_{ab} + V_{cd}}{L_s} \\ I_0 - I_1 &= (\frac{T_s}{2} - \frac{\phi T_s}{2}) \frac{V_{ab} - V_{cd}}{L_s} \end{aligned} \quad (3.11)$$

where $I_0 = |I_{Ls}(0)|, I_1 = |I_{Ls}(\frac{\phi T_s}{2})|$.

From (3.10) and (3.11), the initial current and the maximum current in the steady state can be calculated during a switching cycle.

$$\begin{aligned} I_{Ls}(0) = -I_0 &= \frac{T_s}{4L_s}[(1-2\phi)V_{cd} - V_{ab}] = \frac{1}{4f_s L_s}[(1-2\phi)V_{cd} - V_{ab}] \\ I_{Ls}(\frac{\phi T_s}{2}) = I_1 &= \frac{T_s}{4L_s}[(2\phi-1)V_{ab} + V_{cd}] = \frac{1}{4f_s L_s}[(2\phi-1)V_{ab} + V_{cd}] \end{aligned} \quad (3.12)$$

Q represents the area enclosed by the current and the time axis in half a cycle. Substitute (3.11), so that the area Q shown in Fig.3.7 can be calculated as

$$\begin{aligned} Q &= \frac{1}{2}(I_0 + I_1)(\frac{T_s}{2} - \frac{\phi T_s}{2}) + \frac{1}{2}t_1 I_0 - \frac{1}{2}t_2 I_1 \\ &= \frac{1}{2} \frac{\phi T_s}{2} \frac{V_{ab} + V_{cd}}{L_s} (\frac{T_s}{2} - \frac{\phi T_s}{2}) + \frac{1}{2} \frac{I_0^2 L_s}{V_{ab} + V_{cd}} - \frac{1}{2} \frac{I_1^2 L_s}{V_{ab} + V_{cd}} \\ &= \phi \frac{T_s}{4} \frac{V_{ab} + V_{cd}}{L_s} (\frac{T_s}{2} - \frac{\phi T_s}{2}) + \frac{1}{2} \frac{L_s}{V_{ab} + V_{cd}} (I_0^2 - I_1^2) \\ &= \phi \frac{T_s}{4} \frac{V_{ab} + V_{cd}}{L_s} (\frac{T_s}{2} - \frac{\phi T_s}{2}) + \phi \frac{T_s}{4} (\frac{T_s}{2} - \phi \frac{T_s}{2}) (\frac{V_{ab} - V_{cd}}{L_s}) \\ &= \phi \frac{T_s}{2L_s} (\frac{T_s}{2} - \frac{\phi T_s}{2}) V_{ab} \end{aligned} \quad (3.13)$$

The average output current I_{out} is calculated by substituting $V_{ab} = \frac{V_{HV}}{2}$ in (3.13).

$$I_{out} = n I_{outpri} = n \frac{Q}{T_s} = n \frac{V_{ab} \phi T_s (1 - \phi)}{2L_s} = \frac{n V_{HV} \phi T_s (1 - \phi)}{4L_s} \quad (3.14)$$

$T_s = \frac{1}{f_s}$, thus, the total power is given.

$$P_o = I_{out} V_o = \frac{n V_{HV} \phi T_s (1 - \phi)}{4L_s} V_{LV} = \frac{n V_{HV} V_{LV} \phi (1 - \phi)}{4f_s L_s} \quad (3.15)$$

The output power is valid for both directions. The only difference is that the phase shift is positive for the charge mode and negative for the discharge mode. Thus, the bidirectional output power is

$$P_o = \frac{n V_{HV} V_{LV} \phi (1 - |\phi|)}{4f_s L_s} \quad (3.16)$$

P_o can be normalized as

$$P_{unit} = \frac{P_o}{P_{base}} = \frac{\frac{n V_{HV} V_{LV} \phi (1 - |\phi|)}{4f_s L_s}}{\frac{V_{ab}^2}{4f_s L_s}} = 4\phi(1 - |\phi|) \frac{n V_{LV}}{V_{HV}} \quad (3.17)$$

Fig.3.8 illustrates the bidirectional output power versus phase shift. In charging mode, the maximum power occurs when the phase shift $\phi = 0.5$. The nominal output power can be achieved when $\Phi =$

0.276(49.68°). On the other hand, opposite results can be found in discharging mode. Apart from this, Fig.3.8 illustrates that the topology shares identical power characteristics with the conventional DAB. As a result, the same control strategy can be seamlessly applied.

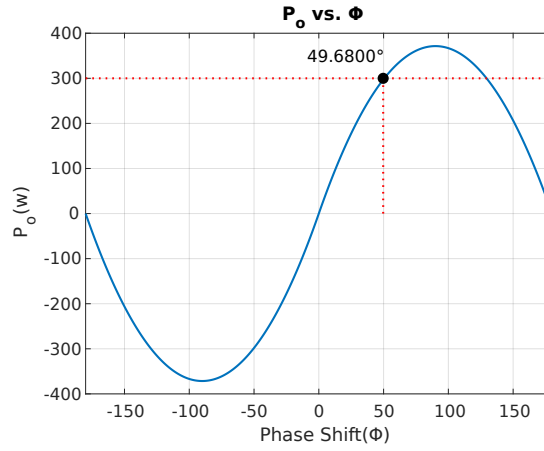


Figure 3.8: Output power versus phase shift

3.4.3. ZVS

Fig.3.9a shows the variation of output power with respect to ϕ across distinct voltage ratios (M) for two operational modes. Complete ZVS can be sustained throughout the entire range of ϕ when M equals 1. Conversely, in both quadrants, the ZVS range diminishes unless M equals 1. The condition to achieve ZVS is shown in this section. Considering that the voltage ratio is $M = V_{cd}/V_{ab}$, substitute M for initial conditions in (3.12).

$$|I_{Ls(0)}| = \frac{V_{ab}}{4f_s L_s} (2\phi M + 1 - M) \quad (3.18)$$

$$|I_{Ls(\frac{\phi T_s}{2})}| = \frac{V_{ab}}{4f_s L_s} (2\phi - 1 + M)$$

The necessary condition to achieve ZVS is that both $I_{Ls(0)}$ and $I_{Ls(\frac{\phi T_s}{2})}$ are larger than zero if M is not equal to 1. Thus, the following expressions are fulfilled

$$\phi > \frac{1 - M}{2} \quad (3.19)$$

$$\phi > \frac{M - 1}{2M}$$

Substitute (3.19) to (3.17). The two dashed lines represent the ZVS threshold for the two side power transistors in Fig.3.9a. The green zone represents the ZVS range.

The above analysis assumes an ideal situation. When considering transformer magnetizing inductance and device parasitic capacitors, the $I_{Ls(0)}$ and $I_{Ls(\frac{\phi T_s}{2})}$ are not only larger than zero but also larger than a certain value. As a consequence, the sufficient condition is that the stored energy in the leakage inductance at the moment of switching one full bridge must be greater than the stored energy in the transistors that comprise the full bridge. The boundary is modified as Fig.3.9b shows[53].

$$\phi > \frac{M - 1}{2M} + \frac{2\sqrt{L_s C_{eqi}}}{TM} \quad (3.20)$$

$$\phi > \frac{1 - M}{2} + \frac{2Mn\sqrt{L_s C_{eqo}}}{T}$$

where C_{eq_i} and C_{eq_o} are the equivalent values of the parasitic capacitances of the transistor of the bridge.

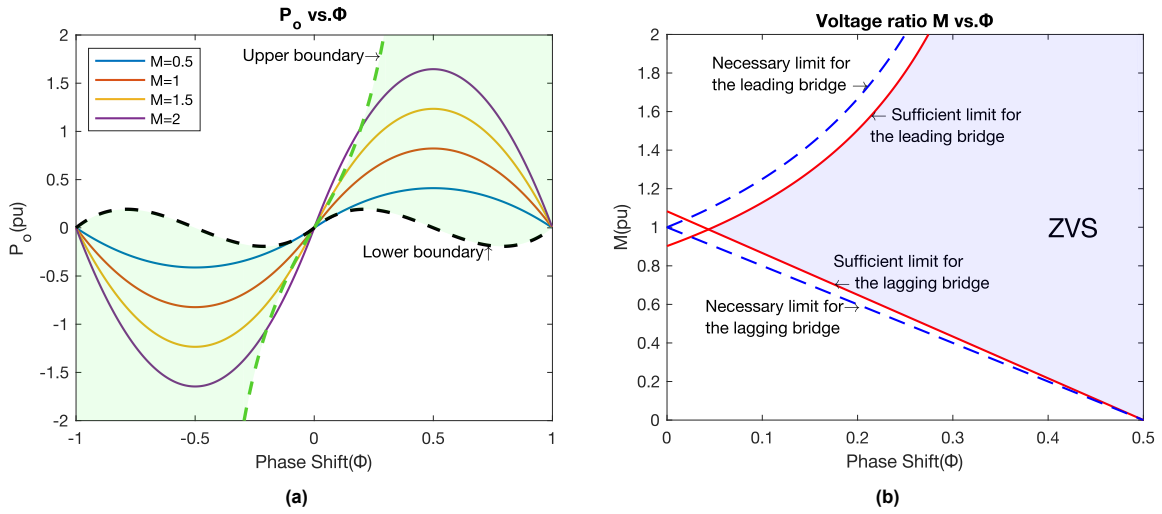


Figure 3.9: ZVS range (a) Family of P_o vs phase shift, with M (voltage ratio) as a parameter. (b) n vs phase shift

3.5. Dynamic analysis

Before designing the controller, mathematical modeling on the physical structure is necessary. State-space averaging technique is the widely used modeling methodology. There are two important assumptions: (1) Small AC changes of the state quantities; (2) The cross-over frequency is less than the switching frequency. Since the i_{L_s} is an AC current, the accuracy will be lost if state-space averaging is applied. [15] summarizes the classification of modeling methods such as the Generalized average model, Reduced-order model, and Discrete-time model. The reduced order model is recommended for DAHB modeling after comparing the results both with large signal and small signal.

3.5.1. Mathematical model derivation

According to Fig.3.1 and Fig.3.6, active clamp circuits have no impact on the main switches, thus, they can be ignored when building the mathematical model. The ten operation modes can be combined into four main modes, corresponding to (3.2)-(3.5).

The state variables of the dynamic system are chosen to be the leakage inductance current i_l , capacitor voltage v_1, v_2 and v_{5p} . All of the variables are converted to the primary side, thus,

$$\begin{aligned} v_{5p} &= nV_5 \\ C_{5p} &= \frac{C_5}{n^2} \\ R_{op} &= n^2 R_o \end{aligned} \quad (3.21)$$

Operation mode 1

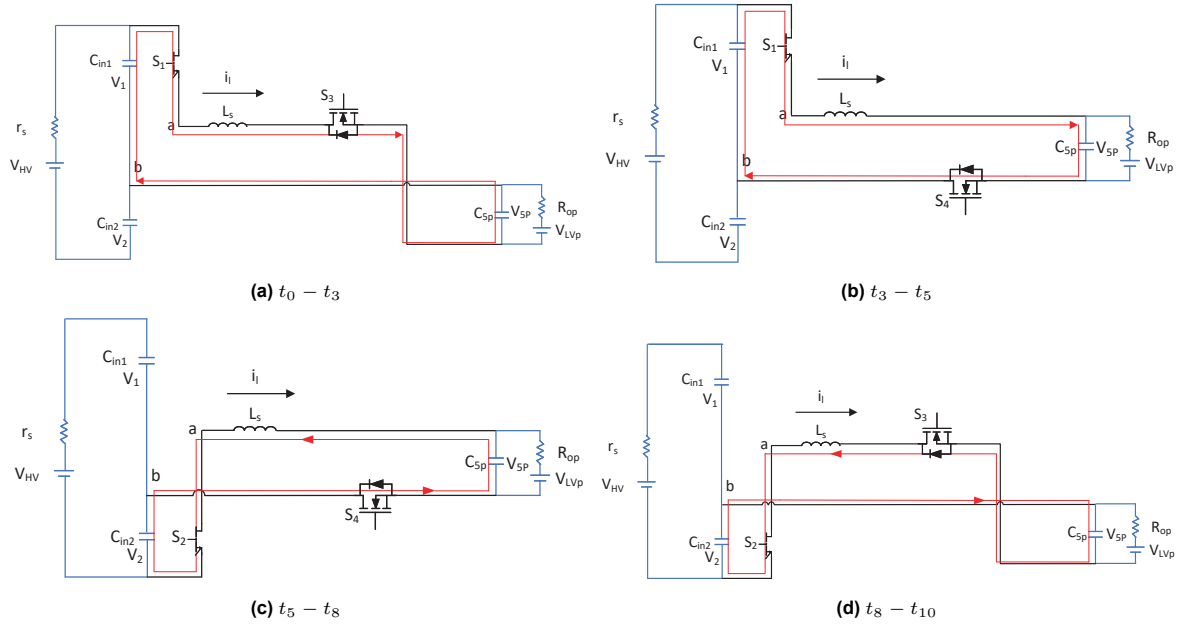


Figure 3.10: The simplified circuit of the proposed DAB

$$\begin{bmatrix} \frac{di_l}{dt} \\ \frac{dv_1}{dt} \\ \frac{dv_2}{dt} \\ \frac{dv_{5p}}{dt} \end{bmatrix} = \begin{bmatrix} 0 & \frac{1}{L_s} & 0 & \frac{1}{L_s} \\ -\frac{1}{C_{in1}} & -\frac{1}{C_{in1}r_s} & -\frac{1}{C_{in2}r_s} & 0 \\ 0 & -\frac{1}{C_{in1}r_s} & -\frac{1}{C_{in2}r_s} & 0 \\ -\frac{1}{C_{5p}} & 0 & 0 & -\frac{1}{C_{5p}R_{op}} \end{bmatrix} \begin{bmatrix} i_l \\ v_1 \\ v_2 \\ v_{5p} \end{bmatrix} + \begin{bmatrix} 0 & 0 \\ \frac{1}{C_{in1}r_s} & 0 \\ \frac{1}{C_{in2}r_s} & 0 \\ 0 & \frac{1}{C_{5p}R_{op}} \end{bmatrix} \begin{bmatrix} V_{HV} \\ V_{LVP} \end{bmatrix} \quad (3.22)$$

Operation mode 2

$$\begin{bmatrix} \frac{di_l}{dt} \\ \frac{dv_1}{dt} \\ \frac{dv_2}{dt} \\ \frac{dv_{5p}}{dt} \end{bmatrix} = \begin{bmatrix} 0 & \frac{1}{L_s} & 0 & -\frac{1}{L_s} \\ -\frac{1}{C_{in1}} & -\frac{1}{C_{in1}r_s} & -\frac{1}{C_{in2}r_s} & 0 \\ 0 & -\frac{1}{C_{in1}r_s} & -\frac{1}{C_{in2}r_s} & 0 \\ \frac{1}{C_{5p}} & 0 & 0 & -\frac{1}{C_{5p}R_{op}} \end{bmatrix} \begin{bmatrix} i_l \\ v_1 \\ v_2 \\ v_{5p} \end{bmatrix} + \begin{bmatrix} 0 & 0 \\ \frac{1}{C_{in1}r_s} & 0 \\ \frac{1}{C_{in2}r_s} & 0 \\ 0 & \frac{1}{C_{5p}R_{op}} \end{bmatrix} \begin{bmatrix} V_{HV} \\ V_{LVP} \end{bmatrix} \quad (3.23)$$

Operation mode 3

$$\begin{bmatrix} \frac{di_l}{dt} \\ \frac{dv_1}{dt} \\ \frac{dv_2}{dt} \\ \frac{dv_{5p}}{dt} \end{bmatrix} = \begin{bmatrix} 0 & 0 & -\frac{1}{L_s} & -\frac{1}{L_s} \\ 0 & \frac{1}{C_{in1}r_s} & -\frac{1}{C_{in2}r_s} & 0 \\ \frac{1}{C_{in2}} & -\frac{1}{C_{in1}r_s} & -\frac{1}{C_{in2}r_s} & 0 \\ \frac{1}{C_{5p}} & 0 & 0 & -\frac{1}{C_{5p}R_{op}} \end{bmatrix} \begin{bmatrix} i_l \\ v_1 \\ v_2 \\ v_{5p} \end{bmatrix} + \begin{bmatrix} 0 & 0 \\ \frac{1}{C_{in1}r_s} & 0 \\ \frac{1}{C_{in2}r_s} & 0 \\ 0 & \frac{1}{C_{5p}R_{op}} \end{bmatrix} \begin{bmatrix} V_{HV} \\ V_{LVP} \end{bmatrix} \quad (3.24)$$

Operation mode 4

$$\begin{bmatrix} \frac{di_l}{dt} \\ \frac{dv_1}{dt} \\ \frac{dv_2}{dt} \\ \frac{dv_{5p}}{dt} \end{bmatrix} = \begin{bmatrix} 0 & 0 & -\frac{1}{L_s} & \frac{1}{L_s} \\ 0 & \frac{1}{C_{in1}r_s} & -\frac{1}{C_{in2}r_s} & 0 \\ \frac{1}{C_{in2}} & -\frac{1}{C_{in1}r_s} & -\frac{1}{C_{in2}r_s} & 0 \\ -\frac{1}{C_{5p}} & 0 & 0 & -\frac{1}{C_{5p}R_{op}} \end{bmatrix} \begin{bmatrix} i_l \\ v_1 \\ v_2 \\ v_{5p} \end{bmatrix} + \begin{bmatrix} 0 & 0 \\ \frac{1}{C_{in1}r_s} & 0 \\ \frac{1}{C_{in2}r_s} & 0 \\ 0 & \frac{1}{C_{5p}R_{op}} \end{bmatrix} \begin{bmatrix} V_{HV} \\ V_{LVp} \end{bmatrix} \quad (3.25)$$

3.5.2. Average model

To simplify the operation mode equations, some variables will be replaced. From the circuit analysis, $C_{in1} = C_{in2}$, thus, in the subsequent calculations, it will be uniformly represented by C_{in} . Moreover, $v_1 = v_2$ exists when the PWM duty cycle is 0.5. As mentioned before, V_{ab} and V_{cd} represent the voltage of the two sides of the transformer in the primary referenced equivalent circuit, thus, capacitance-voltage v_1 and v_2 can be replaced by V_{ab} and V_{cd} .

i_l exhibits the highest rate of change among the state variables, the system is partitioned into two subsystems: one focusing on the fast variable system and the other on the slower variable system.[28]. The slow state variables can be regarded as constants, while the fast variables can be eliminated with the average output current (3.14). This operation is possible because research indicates that the DAB's dynamic response remains unaffected by leakage inductance. [29] finds perturbations in leakage inductance current, stemming from disturbances like alterations in input voltage or phase-shift ratio, do not propagate to the output side according to research. In the before analysis, the symmetry of the system is demonstrated, thus only positive half-cycle expressions are given. Rewrite the expressions for low variables and averaging V_{ab} and V_{cd} in $[0, T_s]$.

$$\begin{aligned} C_{in} \frac{dV_{abavg}}{dt} &= \frac{V_{HV}}{r_s} - \frac{V_{abavg}}{r_s} + \frac{\Phi^2 - \Phi}{2Lf_s} V_{cdavg} \\ C_{5p} \frac{dV_{cdavg}}{dt} &= -\frac{\Phi^2 - \Phi}{2Lf_s} V_{abavg} - \frac{V_{cdavg}}{R_{op}} + \frac{V_{LVp}}{R_{op}} \end{aligned} \quad (3.26)$$

The steady-state is solved from (3.26). In charging mode, $V_{abavg} = 175V$, V_{cdavg} in primary equivalent circuit is $V_{cdavg} = 145.5V$. In discharging mode, $V_{abavg} = 159V$, $V_{cdavg} = 145.5V$.

3.5.3. Small signal model

Introduce small perturbations in phase-shift ratio and voltage. $v_{HV} = V_{HV} + \Delta v_{HV}$, $v_{LV} = V_{LV} + \Delta v_{LV}$, $\phi = \Phi + \Delta\phi$, $v_{ab} = V_{ab} + \Delta v_{ab}$, $v_{cd} = V_{cd} + \Delta v_{cd}$. In the charging mode, assume there is a current source placed across the nominal load $i_o = 0 + \Delta i_o$. $(\Delta v_{HV}, \Delta i_o, \Delta\phi)$ is chosen as control inputs and $(\Delta v_{ab}, \Delta v_{cd})$ as state variables, Δv_{cd} as control output, state equations can be linearized from (3.26).

Charging mode:

$$\begin{bmatrix} \frac{d\Delta v_{ab}}{dt} \\ \frac{d\Delta v_{cd}}{dt} \end{bmatrix} = \begin{bmatrix} -\frac{1}{r_s C_{in}} & \frac{\Phi^2 - \Phi}{2L_s f_s C_{in}} \\ -\frac{\Phi^2 - \Phi}{2L_s f_s C_{5p}} & -\frac{1}{R_{op} C_{5p}} \end{bmatrix} \begin{bmatrix} \Delta v_{ab} \\ \Delta v_{cd} \end{bmatrix} + \begin{bmatrix} \frac{1}{r_s C_{in}} & 0 \\ 0 & \frac{1}{C_{5p}} \end{bmatrix} \begin{bmatrix} \frac{2\Phi - 1}{2L_s f_s C_{in}} V_{cdavg} \\ \frac{2\Phi + 1}{2L_s f_s C_{5p}} V_{abavg} \end{bmatrix} \begin{bmatrix} \Delta v_{HV} \\ \Delta i_o \\ \Delta\phi \end{bmatrix} \quad (3.27)$$

$$\Delta v_o = \begin{bmatrix} 0 & 1 \end{bmatrix} \begin{bmatrix} \Delta v_{ab} \\ \Delta v_{cd} \end{bmatrix}$$

In discharging mode, the output resistance can be calculated as $R_o = V_{HV}^2 / P_o$. The inner resistance

of the low side voltage source should be referenced to the primary side r_{sp} . Assume a current source is placed across the nominal load, Δv_{ab} as control output.

Discharging mode:

$$\begin{bmatrix} d\frac{\Delta v_{ab}}{dt} \\ d\frac{\Delta v_{cd}}{dt} \end{bmatrix} = \begin{bmatrix} -\frac{1}{R_o C_{in}} & \frac{\Phi^2 - \Phi}{2L_s f_s C_{in}} \\ -\frac{\Phi^2 - \Phi}{2L_s f_s C_{5p}} & -\frac{1}{r_{sp} C_{5p}} \end{bmatrix} \begin{bmatrix} \Delta v_{ab} \\ \Delta v_{cd} \end{bmatrix} + \begin{bmatrix} \frac{1}{C_{in}} & 0 & \frac{2\Phi - 1}{2L_s f_s C_{in}} V_{cdavg} \\ 0 & \frac{1}{r_{sp} C_{5p}} & \frac{-2\Phi + 1}{2L_s f_s C_{5p}} V_{abavg} \end{bmatrix} \begin{bmatrix} \Delta i_o \\ \Delta v_{LV} \\ \Delta \phi \end{bmatrix} \quad (3.28)$$

$$\Delta v_o = \begin{bmatrix} 1 & 0 \end{bmatrix} \begin{bmatrix} \Delta v_{ab} \\ \Delta v_{cd} \end{bmatrix}$$

Tab.3.1 shows the designed parameters:

Table 3.1: DAHB modeling parameters

Sign	Parameter	Nominal value
P_o	Output power	300w
n	Transformer turns ratio	6
f_s	Switching frequency	200kHz
V_{HV}	High side voltage source	350V
V_{LV}	Low side voltage source	24V
R_o	Output resistance	1.92Ω for charging mode 408Ω for discharging mode
L_s	Leakage inductance	21.2μH
C_{in}	High side capacitance	15μF
C_5	Output capacitance	165μF

From Fig.3.8, $\Phi = 0.11$ is selected for charging mode, and $\Phi = -0.11$ is for discharging mode.

Charging mode

The output voltage to output current is:

$$T_{vo-io}(s) = \frac{\Delta v_o}{\Delta i_o} = \frac{2.187 \times 10^{11}}{s^2 + 6.667 \times 10^7 s + 2.104 \times 10^{11}} \quad (3.29)$$

The input-to-output transfer function is:

$$T_{vo-vin}(s) = \frac{\Delta v_o}{\Delta v_{in}} = \frac{2.182 \times 10^5 s + 1.455 \times 10^{13}}{s^2 + 6.667 \times 10^7 s + 2.104 \times 10^{11}} \quad (3.30)$$

The control-to-output transfer function is as follows:

$$T_{vo-\phi}(s) = \frac{\Delta v_o}{\Delta \phi} = \frac{3.152 \times 10^6 s^3 + 4.202 \times 10^{14} s^2 + 1.401 \times 10^{22} s + 4.422 \times 10^{25}}{s^4 + 1.333 \times 10^8 s^3 + 4.445 \times 10^{15} s^2 + 2.806 \times 10^{19} s + 4.429 \times 10^{12}} \quad (3.31)$$

Discharging mode

The output voltage to output current is:

$$T_{vo-io}(s) = \frac{\Delta v_o}{\Delta i_o} = \frac{6.667 \times 10^4 s + 4.04 \times 10^{11}}{s^2 + 6.061 \times 10^6 s + 9.955 \times 10^8} \quad (3.32)$$

The input-to-output transfer function is:

$$T_{v_o-vin}(s) = \frac{\Delta v_o}{\Delta v_{in}} = \frac{8.219 \times 10^9}{s^2 + 6.061 \times 10^6 s + 9.955 \times 10^8} \quad (3.33)$$

The control-to-output transfer function is:

$$T_{v_o-\phi}(s) = \frac{\Delta v_o}{\Delta \phi} = \frac{-1.472 \times 10^6 s^3 - 1.783 \times 10^{13} s^2 - 5.402 \times 10^{19} s - 8.872 \times 10^{21}}{s^4 + 1.212 \times 10^7 s^3 + 3.673 \times 10^{13} s^2 + 1.207 \times 10^{16} s + 9.91 \times 10^{17}} \quad (3.34)$$

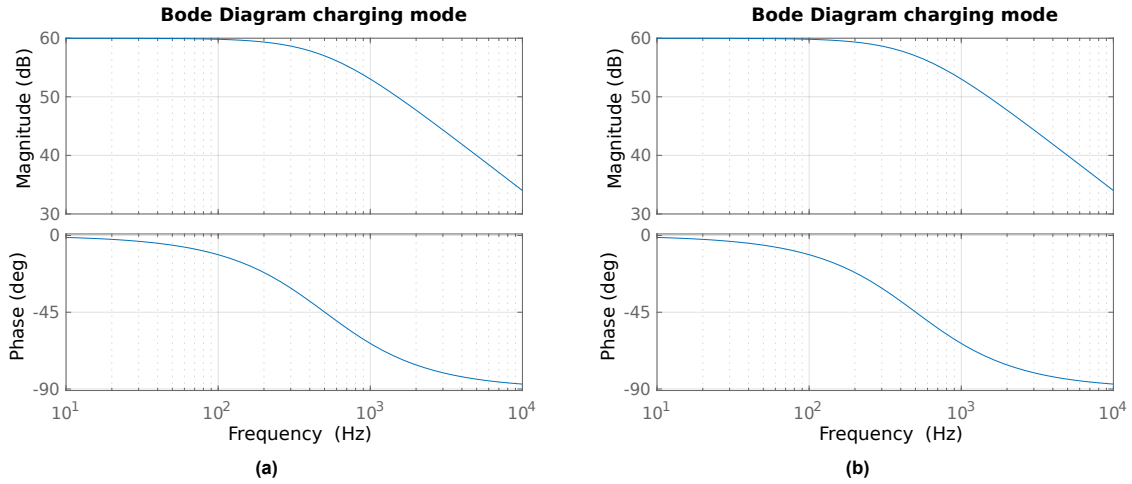


Figure 3.11: Output to control bode plot (a) Charging mode (b) Discharging mode

3.5.4. Control system design

The configuration of the control system is in Fig.3.12. Proportional integral (PI) controllers are one of the most widely used controllers and are commonly used in control system design[29]. A PI controller that is capable of ensuring a zero steady-state error and responding rapidly is considered to obtain an accurate tracking of the input reference. As shown in Fig.3.12, the DAB is fed by the regulated phase shift from PI controller.

Since the proportional component has the effect of reducing the rise time and the integral component has the capability to eliminate the steady-state error, they are totally independent[54]. Thus, K_i can be set to 0 when analyzing the influence of K_p , and vice versa.

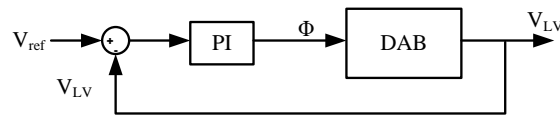


Figure 3.12: Block diagram of feedback control

Charging mode

Before tuning the PI controller, the stability of the system should be verified. Consequently, it is necessary to derive the transfer function of the closed-loop system and analyze the bode plot of the open-loop system.

The frequency at which the gain is equal to 0 dB is called crossover frequency. This frequency is extended to the phase plot to estimate the phase of the cross-over frequency away from -180° , resulting

in a phase margin. Similarly, the gain margin is determined by the point where phase equals -180° meets the magnitude plot and the gain required from that point to reach 0 dB. Fig.3.13a shows some observations based on the variable of K_p . As a rule of thumb, the crossover frequency should be no more than one-tenth of the set switching frequency of the switch-mode power supply, which is 200kHz in this project. Thus, K_p should be at least smaller than 0.04 shown in Tab.3.2. On the other hand, a phase margin (45° - 60°) and a gain margin from 2-10 dB are expected to be maintained for a stable system. This reserve of phase margin ensures that the system remains stable even after the loop is closed due to the delay included in the feedback path and due to any effects of sampling time on the delay.

Parameters	Test 1	Test 2	Test 3	test 4	Test 5
K_p	0.01	0.025	0.04	0.05	0.1
K_i	0	0	0	0	0
Crossover frequency(kHz)	4.99	12.5	20.1	25.1	50.2
Phase margin(deg)	82.3	58.5	37.3	23.4	-44.8
Gain margin(dB)	16.5	8.57	2.55	4.49	-3.47

Table 3.2: Stable margin with variable K_p for charging mode

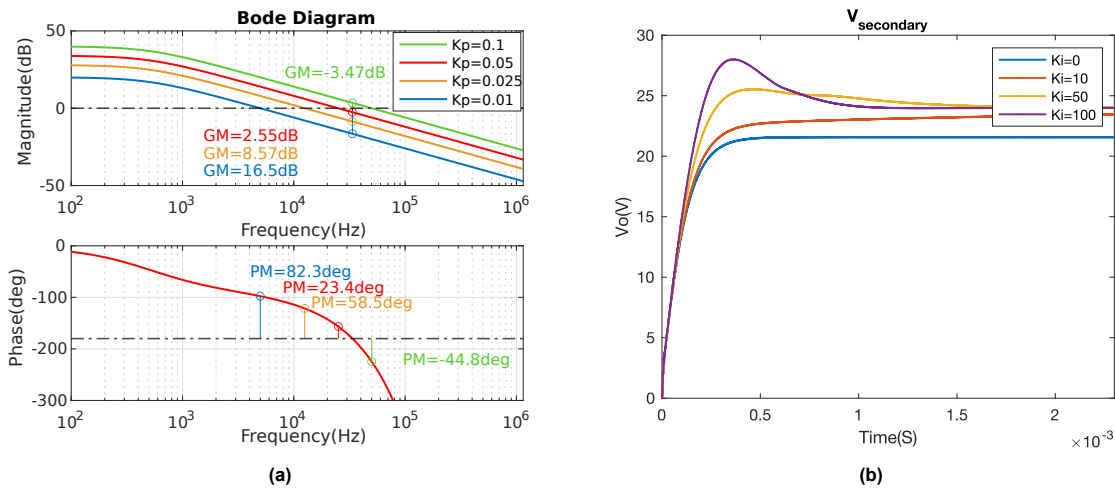


Figure 3.13: Output results with variable K_p and K_i (a) Bode plot with variable K_p (b) Output voltage with variable K_i

Fig.3.13b illustrates the effects of adding integral. The output voltage with variable K_i is compared. In order to maintain the output voltage equal to 24V, K_i is selected as 10.

So far, $K_p=0.02$ and $K_i=10$ are selected. The open loop system has 65.8° phase margin with the PI controller shown in Fig.3.14a. Fig.3.14b demonstrates that all poles are situated in the left-half-plane, confirming the stability of the closed-loop system.

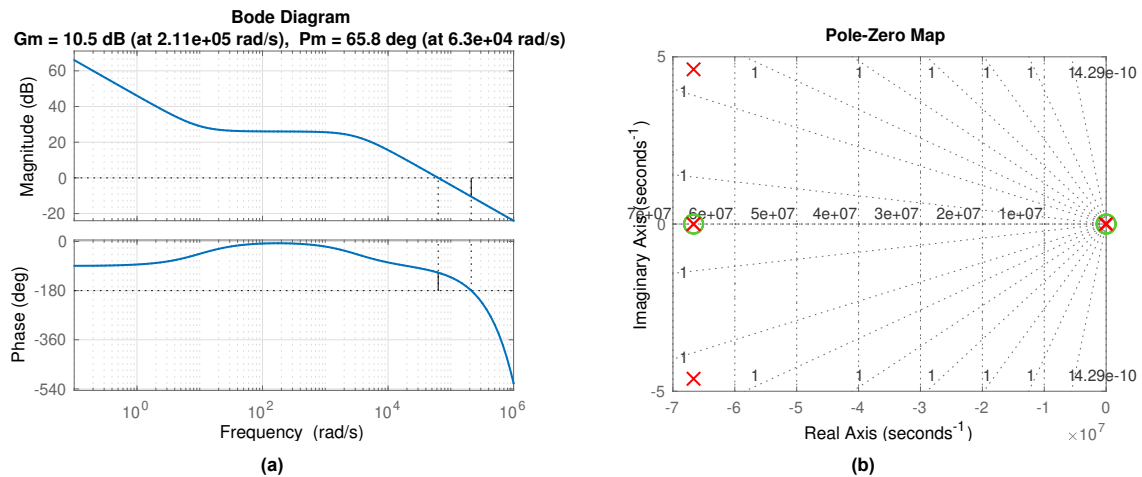


Figure 3.14: Stability analysis (a) Open loop bode diagram with PI controller (b) Pole-Zero map

The stability of the control system is verified in PLECS. At 0.03s, V_{HV} drops from 350V to 355V; at 0.06s, the load power decrease from 300W to 150W. A 2V spike can be observed in Fig.3.15.

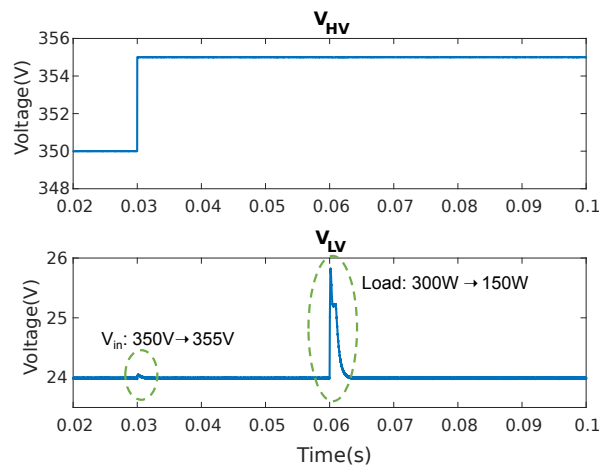


Figure 3.15: Two disturbing tests(0.03s: V_{in} changes from 350v to 355v 0.06s: Rload is doubled)

Discharging mode

For discharging mode, similarly, a PI controller is tuned considering crossover frequency less than 25kHz and phase margin around 45° - 60° and gain margin in 2-10dB. Tab3.3 and Fig.3.16a illustrate that $K_p = -0.07$ can satisfy the stability requirements. Additionally, integration of the K_i component affects the steady-state value, so to operate without steady-state error, $K_i = -0.45$ is selected as shown in Fig.3.16b.

Parameters	Test 1	Test 2	Test 3	Test 4
Kp	-0.05	-0.085	-0.1	-0.2
Ki	0	0	0	0
Crossover frequency(kHz)	11.7	19.9	23.4	46.8
Phase margin(deg)	58.5	36.4	26.9	-36.3
Gain margin(dB)	9.1	4.49	3.08	-2.94

Table 3.3: Stable margin with variable Kp for discharging mode

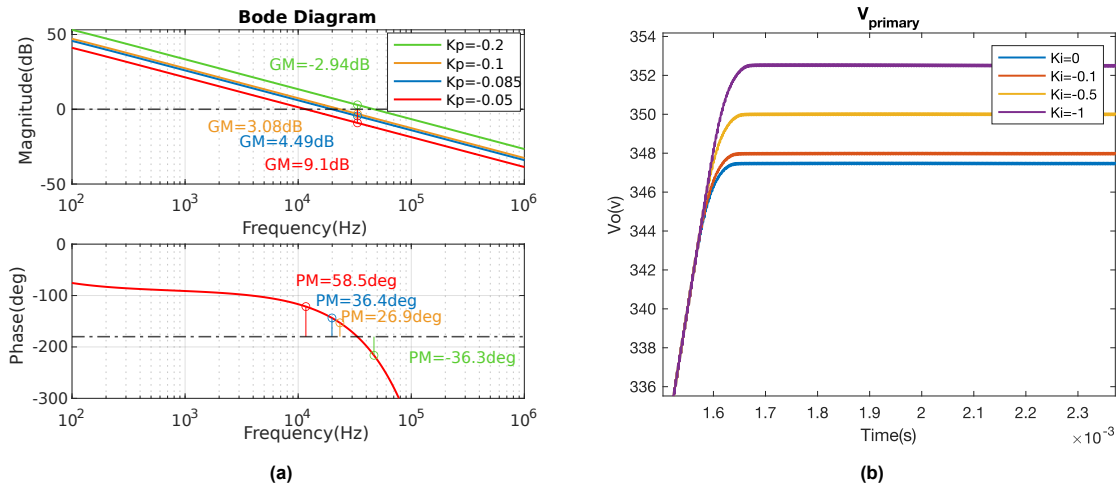


Figure 3.16: Output results with variable K_p and K_i (a) Bode plot with variable Kp (b) Output voltage with variable Ki

In fig.3.17a, the bode plot of the open-loop system is depicted, utilizing $K_p=-0.05$ and $K_i=-0.5$. The crossover frequency is 11.7kHz, the phase margin is 58.5° and the gain margin is 9.1dB. Fig.3.17b shows the pole-zero map, since one pair of pole and zero are in the same location on the right plane, the system remains stable.

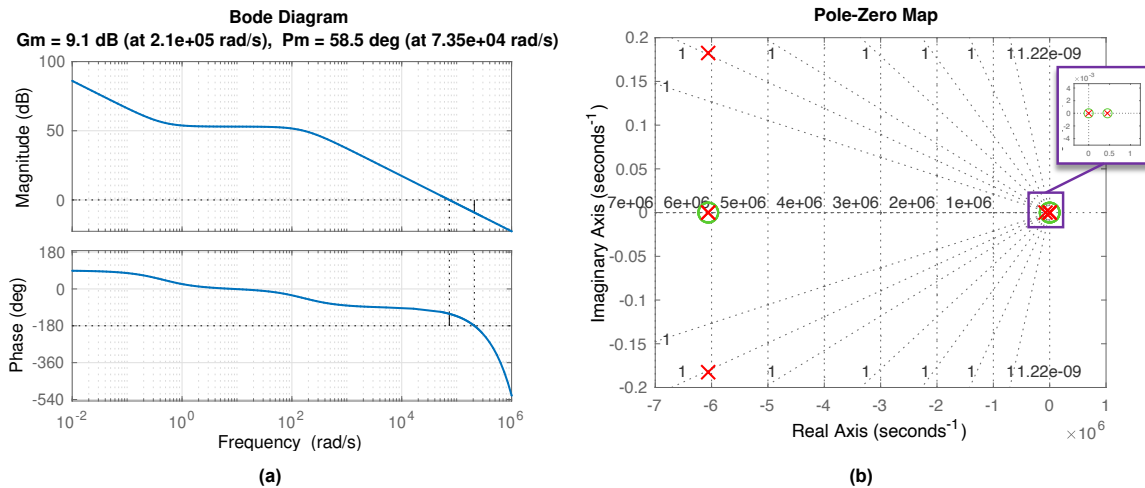


Figure 3.17: Stability analysis (a) Open loop bode diagram with PI controller (b) Pole-Zero map

Two disturbing cases are tested: the input voltage changing from 24V to 20V at $t=0.03s$; and the load power reduction from 300W to 150W at $t=0.06s$. A seamless transition with input voltage change and a 2V spike at $t=0.06s$ is seen in Fig.3.18 illustrates the rationality of controller design.

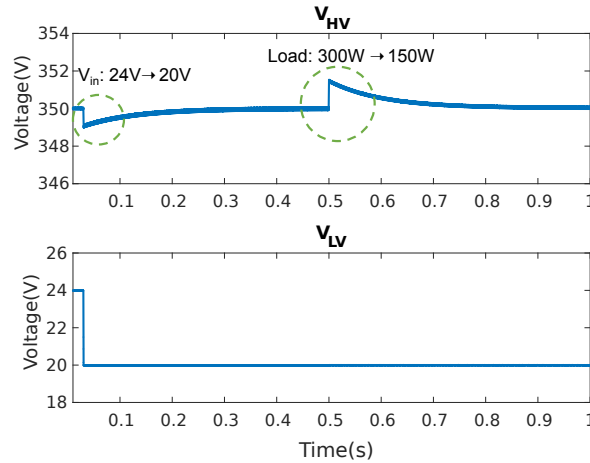


Figure 3.18: Two disturbing tests(0.03s: V_{in} changes from 24v to 20v 0.06s: Rload is doubled)

3.6. Conclusion

The modeling of a DAHB converter is analyzed in this chapter. Since the modeling is based on an existing converter, the values of the components used in the modeling and simulation are chosen to be the same as those seen in actual converters. Firstly, the advantages of this developed half-bridge push-pull converter are compared with a conventional DAB converter. Then, the effect of the active clamping circuit is analyzed, and from the simulation results, it can be observed that utilizing of active clamping circuit can significantly reduce the spike of the secondary side switch current.

Moreover, analyzes the power transfer characteristics by considering all equivalent circuits within various intervals of a single period. This comprehensive examination includes an investigation of the steady-state behavior, which allows for the derivation of the output power equation. By establishing a relationship between the output power and the phase shift, the range of ZVS is constrained under single phase shift modulation.

Furthermore, the dynamic state of the system is also analyzed. This needs deriving the transfer function for bidirectional operation through the utilization of mathematical models. Subsequently, the open-loop system's Bode plot is constructed. A PI controller is implemented to guarantee that the converter possesses an adequate phase margin and gain margin. To assess the stability of the system, bode plots, and zero-pole maps are examined.

Last but not least, in order to corroborate the design derived from mathematical models, the model is built in PLECS, and disturbance tests are performed. These experimental tests validate the mathematical design by subjecting the model to various disturbances, ensuring that the system exhibits the desired performance characteristics.

4

Modeling and Droop Control of DC Microgrid

4.1. Overview

While many researchers have built basic DC microgrids, most have focused on improving the modeling of one converter in the grid, resulting in a relatively simple grid structure, such as an MPPT converter, a battery with a bidirectional converter, and a DC load connecting to a unipolar grid. This chapter presents the modeling of a 350V bipolar DC microgrid used for energy access which has the same configuration as the existing grid in the green village. In this context, the DAHB converter modeled aforementioned serves as a bridge connecting the SHS and the grid. Firstly, the grid is built in Matlab/Simulink, then, each converter implements a local control utilizing a droop V-I characteristic and a PI controller. To enhance the robustness of the MPPT converter, an adaptive step size algorithm is employed in the MPPT algorithm. Additionally, the battery buck-boost converter utilizes an adaptive control strategy based on State of Charge (SoC) considerations.

4.2. Schematic

In this chapter, a 350V bipolar DC microgrid is designed and connected to the dual active half-bridge converter that was previously modeled. To produce solar energy, two separate and independent PV strings are connected to an MPPT converter. To balance the voltage from positive to neutral and from neutral to negative under unbalanced load conditions or unbalanced solar energy conditions, a balancing converter is linked to +350V, 0, and -350V. Two DC loads are respectively linked to the positive pole between the neutral pole, and the neutral pole between the negative pole. An EV charger is represented by a DC load with a DC/DC converter, and an AC load with an AC/DC converter represents the capability of the system to transition from isolated grid mode to the AC grid. A battery discharge when solar energy is insufficient and charge when photovoltaic energy is at rest. The DAHB that was previously modeled connects this microgrid and a 24V SCS. The SCS uses a single PV panel and a battery as renewable energy sources. In the case that there is no photovoltaic energy and the battery is empty, the grid acts as a backup source of energy. To ensure the battery operates safely, a circuit breaker is connected to it. The sole load in the SCS is a 60W power bank.

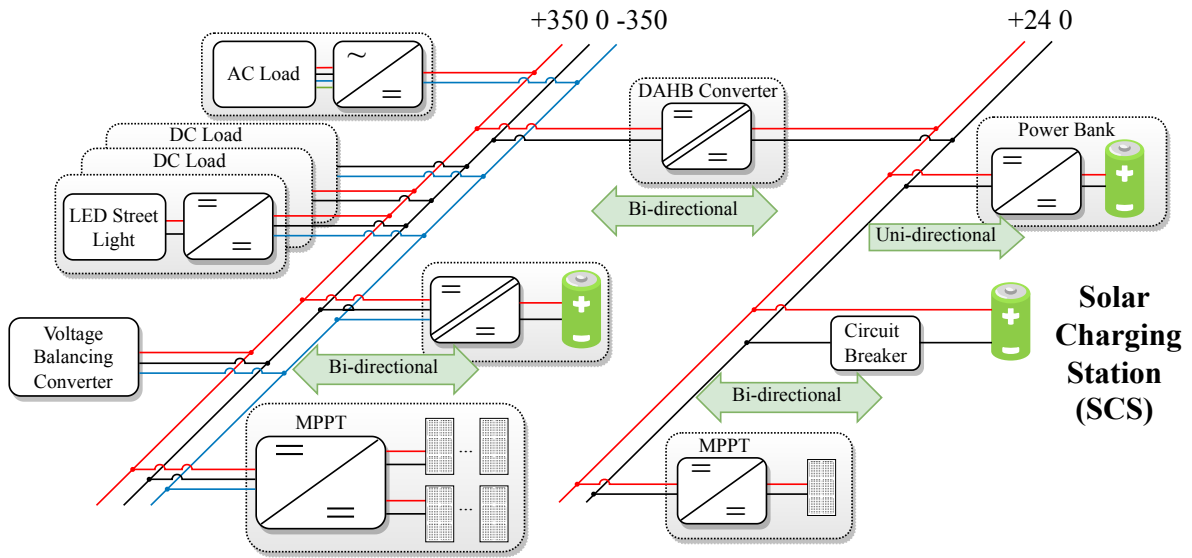


Figure 4.1: Schematic of a DC microgrid

4.3. Components modeling

4.3.1. MPPT converter

Solar energy is immediately converted into electricity by solar cells. Its operation is dependent on the solar cell's photovoltaic effect. Power production from PV panels is dependent on the environment. Fig.4.2a shows the relationship of output voltage and power. To maximize the efficiency, PV panels should be operated at a point where they produce the most power.

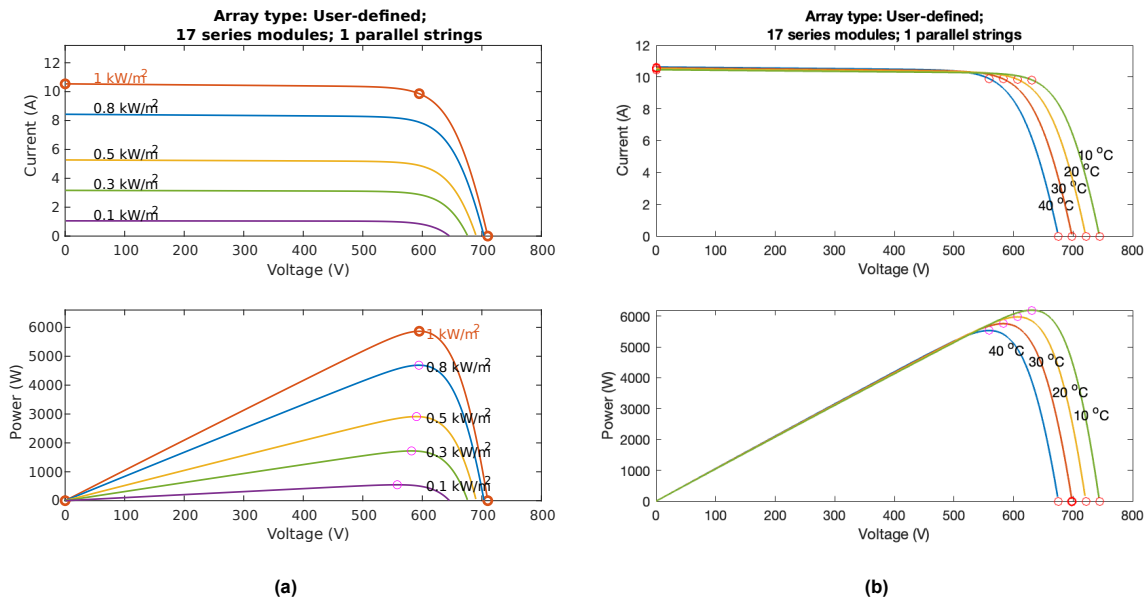


Figure 4.2: I vs V and P vs V characteristics (a) with different irradiance (b) with different temperature

In MPPT converters, maximum power is obtained. The topology of the MPPT converter used in this project is shown in Fig.4.3. This topology is capable of balancing input voltage if the difference between V_{pv1} and V_{pv2} is not large.

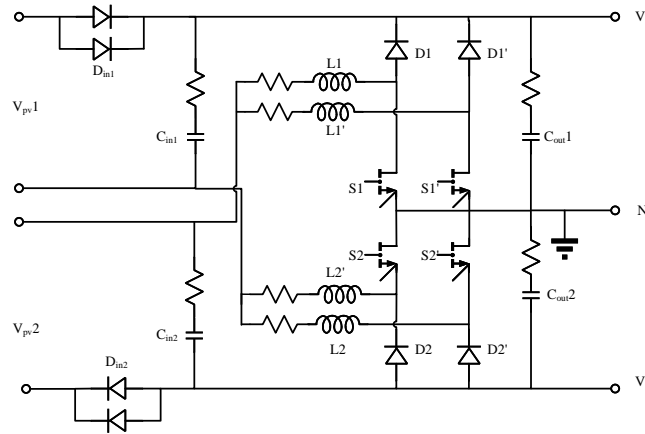


Figure 4.3: MPPT converter topology

Implementation of control

A cascaded PI control strategy is designed for the previous MPPT converter. In MPPT control algorithm inner loop, the input current set point is provided by the comparison of the input voltage and reference voltage generated from the MPPT control algorithm. On the other hand, the input current set point in the droop control inner loop is calculated by the input power. The MPPT converter’s control characteristic is represented by the orange line in Fig.4.7, and it is possible to determine the output current set point from the droop curve. Once the output power is obtained, the input current set point can then be determined. The MPPT converter’s input and output variables V_{pv} , i_{pv} , i_o , and i_o are then passed to a state machine, which decides whether to use the MPPT or the droop control based on the generated power and input power. An outer PI controller then generates the duty cycle as the gate signal of an MPPT converter based on the difference between $I_{in_setpoint}$ and input current i_{pv} . This cascade control strategy improves system stability and robustness. The following section will discuss the implemented MPPT control and droop control, respectively.

MPPT control

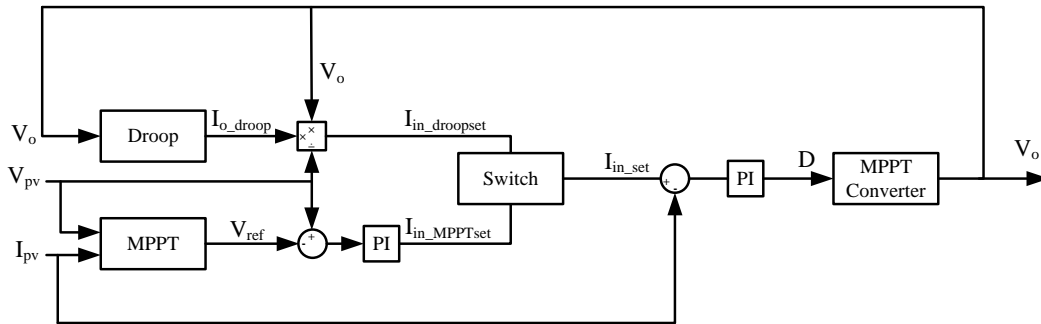


Figure 4.4: Cascade PI Control for the MPPT converter

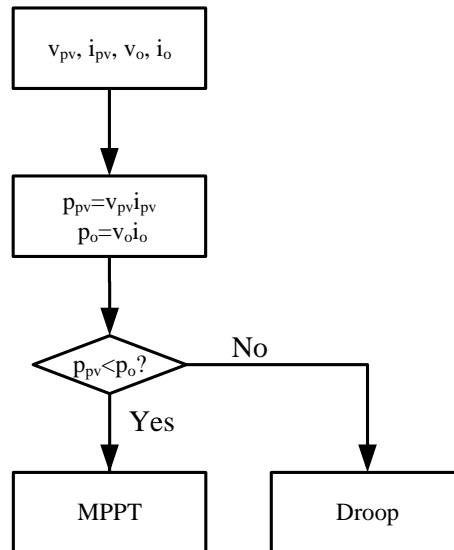
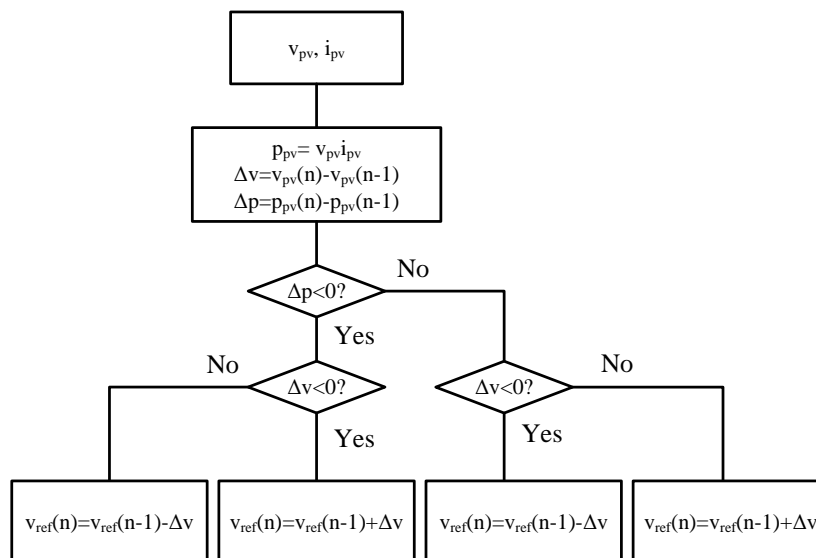


Figure 4.5: State machine flowing chart

The flowing chart of the Perturb and Observe (P&O) algorithm is shown in Fig.4.6a. It should be noted that with the P&O algorithm, the converter can be controlled quite easily, however, it will have some drawbacks such as oscillating around the maximum power point and slowly tracking rapid changes in irradiance. In order to solve this problem, an improved P&O with an adaptive step size algorithm is developed in Fig.4.6b. From Fig.4.6a, V_{ref} always plus a Δv if Δv and Δp has the same sign, otherwise, subtract Δv . As a result, a StepFactor may be added based on the algorithm's operating frequency, and the change in the reference voltage is determined by the product of StepFactor and the ratio between Δv and Δp . This advanced MPPT P&O algorithm increases the robustness of the simple P&O algorithm as well as responds much more quickly than the P&O algorithm



(a)

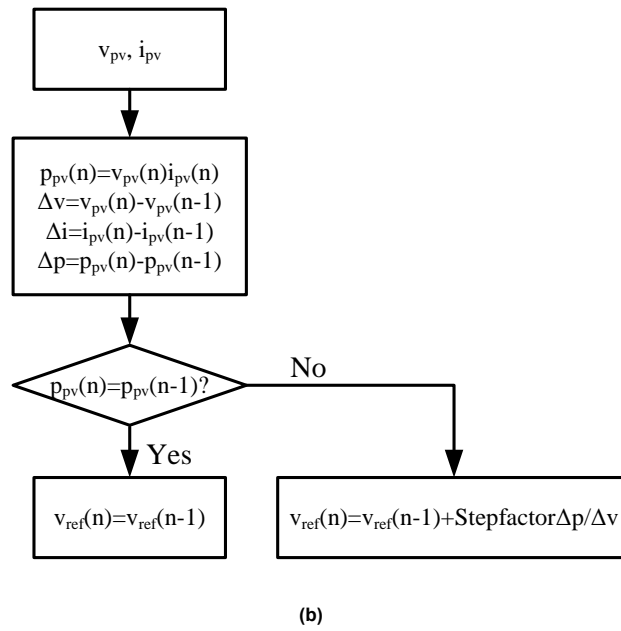


Figure 4.6: MPPT algorithms (a) Perturb and Observe MPPT algorithm (b) Perturb and Observe MPPT with adaptive step size algorithm

Droop control

In order to maintain high efficiency, the MPPT converter generally operates in MPPT control operations. However, when the generated power exceeds the grid's capacity, the PV system should operate in droop control, as illustrated in Fig.4.5. The drooping curve is depicted in Fig.4.7 in which the MPPT converter operates in MPPT mode if the grid voltage is lower than 375V, and in droop mode if the grid voltage is higher than 375V. Otherwise, the reference current is set at 0A.

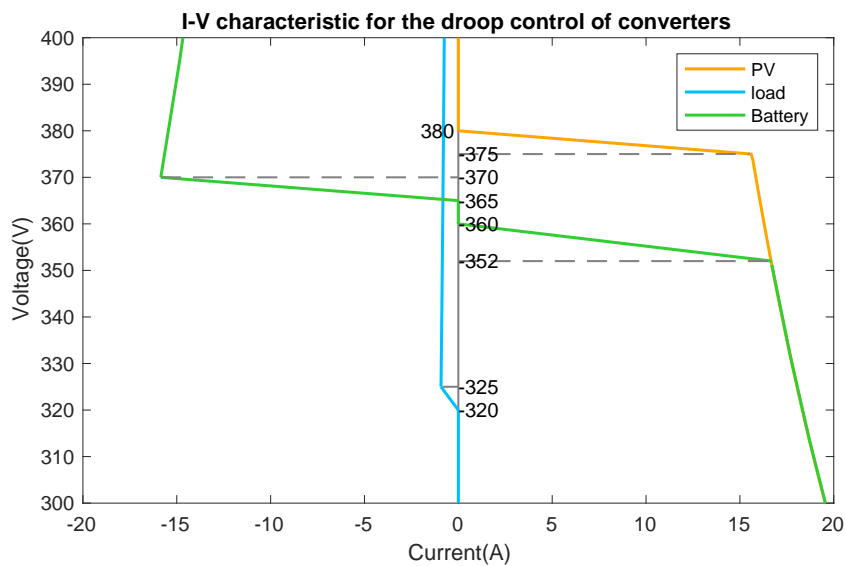


Figure 4.7: I-V characteristic for the droop control of converters

Fig.4.8 illustrates the simulation results of the control. Depending on the radiance, the current varies. It is verified that the generated power is more than 95% efficient when compared to the reference power.

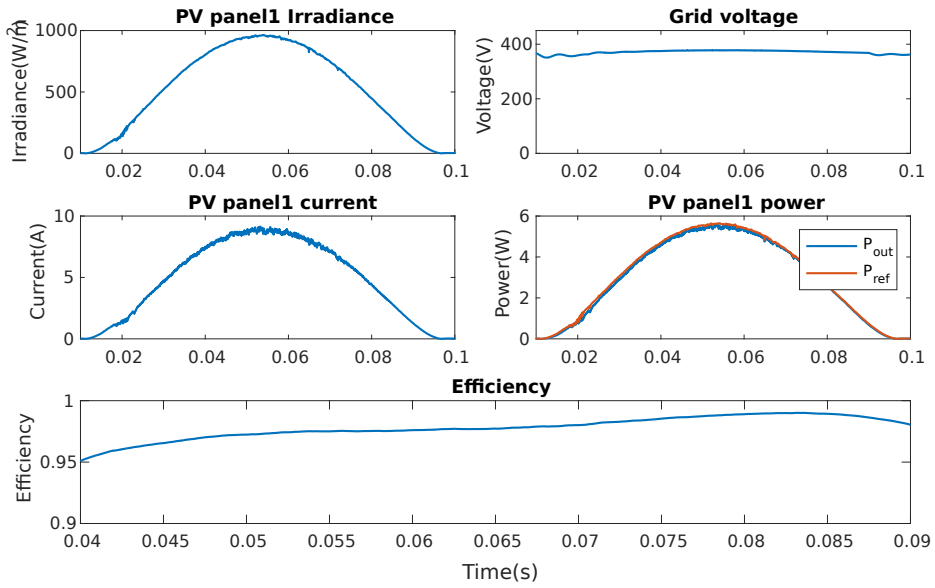


Figure 4.8: Simulation results of MPPT algorithms with a variable irradiance

4.3.2. Voltage balancing converter

As mentioned before, voltage balancing parallels to balance bipolar voltages. Fig.4.1 shows one of the generally used topology. When the two polar are unbalanced, two capacitors are charged and discharged to balance the grid.

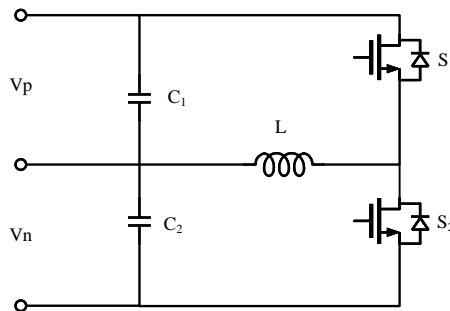


Figure 4.9: Voltage balancing converter topology

Fig.4.10a illustrates the control strategy, positive voltage represented by V_p , and the other is V_n . The inner loop set point is provided by the output results of a droop function shown in Fig.4.10b. The set point is limited to 20A if V_p/V_n is larger than 1.02 or smaller than 0.98. In the range of 0.98 to 0.99 and 1.01 to 1.02, the reference current is set based on the voltage ratio. when V_p/V_n is between 0.99 and 1.01, the reference current is set to 0. The difference between the set point and inductance current passes a PI controller and generates a duty cycle to drive the voltage balancing converter.

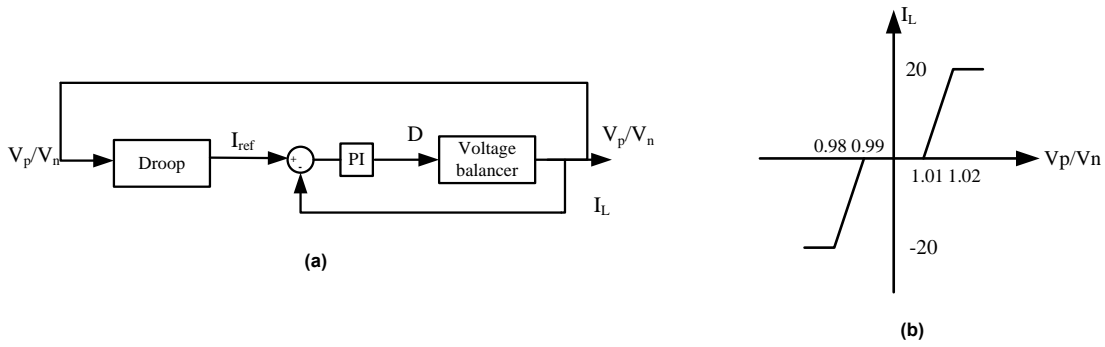


Figure 4.10: Droop control for the voltage balancing converter (a) Block diagram (b) Droop definition

Fig.4.11 illustrates the effect of the balancing converter defined. The irradiation of the PV pane 1 drops from $1000W/m^2$ to $800W/m^2$ at 0.02s and irradiation of the PV panel 2 drops from $1000W/m^2$ to $500W/m^2$ at 0.04s. The Second sub-figure shows the grid voltage without a balancing converter. It can be seen that when the radiance of two photovoltaic panels is within a certain range, MPPT topology is capable of balancing bus voltage, but after 0.032s, the difference in radiance between two photovoltaic panels is too great, so the MPPT converter cannot maintain the same bus voltage. According to the third sub-figure, the grid can always maintain a balanced voltage with a voltage-balancing converter.

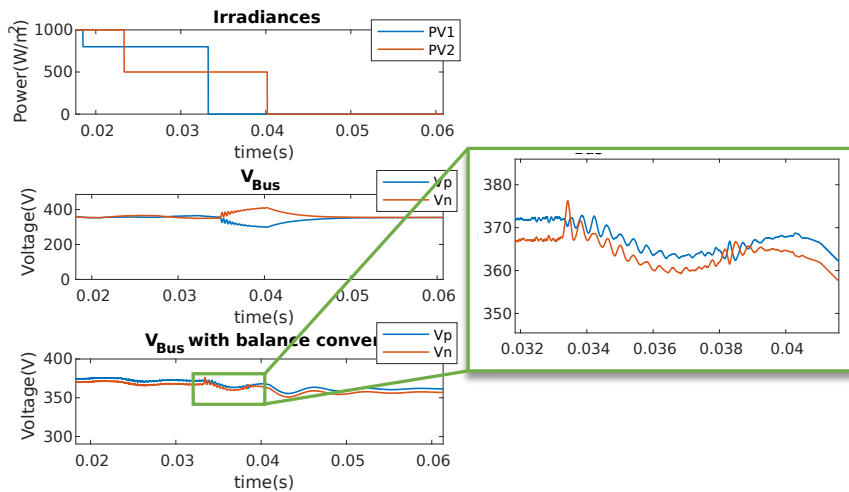


Figure 4.11: Effect of a voltage balancing converter in the bipolar DC microgrid

4.3.3. DC load

Inverted buck converters are commonly used when the load doesn't need to be ground-referenced, such as when driving LEDs. In applications where the load voltage may vary, it provides a regulated output voltage. when converting a wide range of input voltages to the desired output voltage, an inverted buck converter can maintain a stable current which is more suitable for LED. Therefore, Providing flexibility in voltage regulation and ensuring proper LED operation make it an ideal choice for LED lighting applications without ground reference requirements. Fig.4.12 shows a parallel inverted buck converter topology connected to two LED strings with 300 LEDs in each string. Considering that each LED has a voltage drop of 1V, there is a total voltage drop of 300V.

Fig.4.13a illustrates the control strategy for the LED inverted buck converter. The current set point is calculated depending on the droop curve in Fig.4.7, then a current inner loop is used to generate a duty

cycle to control the switch of the converter. It can be seen that the LED voltage can be controlled as 300V and the current is limited as 1A regardless of the grid voltage variation in Fig.4.14.

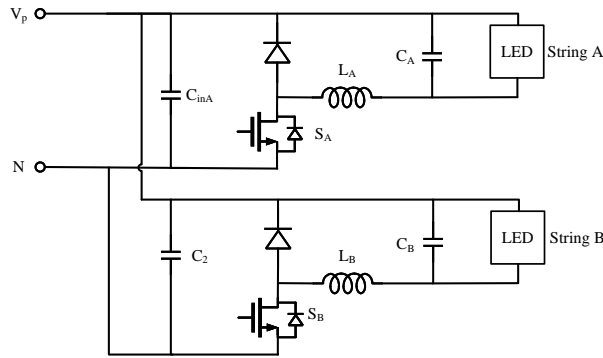


Figure 4.12: LED inverted buck converter topology

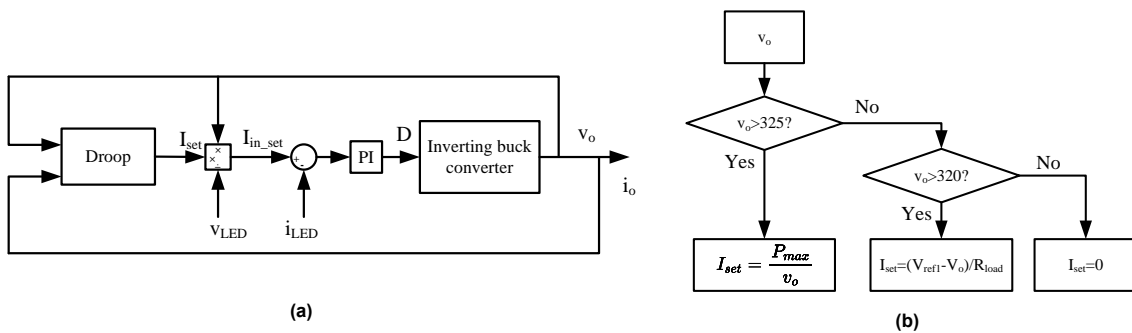


Figure 4.13: Droop control for the LED inverting buck converter (a) Block diagram (b) Droop definition

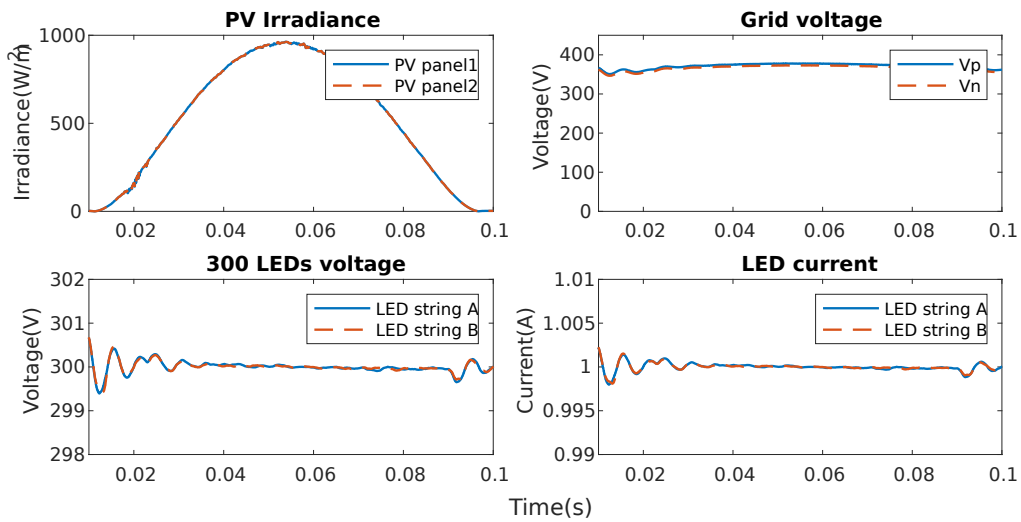


Figure 4.14: Simulation results of the inverting buck converter and LED with variable PV energy

4.3.4. Battery and bidirectional converter

A battery must discharge the grid if the MPPT converter cannot generate the rated grid voltage. As Fig.4.1 shows, a buck-boost DC/DC converter connected to positive and negative poles of the grid

to charge or discharge the batteries. As fig.4.7shows, there are five operation modes for the battery. When the grid voltage is higher than V_{ref1} , it works in charging mode. The battery converter works in maximum power mode until the grid current reaches the limitation. Then as the grid voltage decreases, the converter operates in droop mode and regulates the output current to zero at 730V. In the deadband between 720V and 730V, the converter idles, which means no power is transferred. The converter will discharge power back to the grid if the grid voltage continues to fall. The converter also operates in maximum power mode until a limit is reached in the discharging current, then it droops.

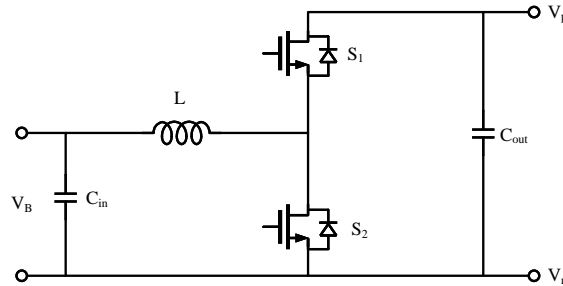


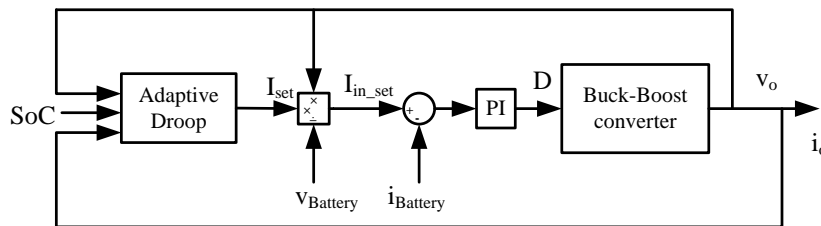
Figure 4.15: Battery buck-boost converter topology

The control block diagram is illustrated in Fig.4.16a. The reference current is provided by an adaptive droop control, and the droop definition is shown in Fig.4.16b. When the battery is at full capacity, indicated by Soc=1, charging is not possible. Conversely, if the battery is completely depleted, characterized by Soc=0, discharging from the grid is not allowed. Therefore, the yellow zone represents all of the idle modes.

The Virtual Resistance (VR) of the droop controller determines the droop zone. However, using the same VR for a battery with multiple SOC levels is not practical. The lower one will deplete faster and have worse lifespan performance as a result. Allowing the battery with lower Soc has more capacity to be charged while higher Soc limits the charging ability. Instead, the higher Soc can be discharged more and the lower one should be discharged less[50]. It is appropriate to apply a smaller slope to a battery with a lower Soc when it is in the charging mode and a higher Soc under discharging mode because a smaller slope enables the current output to be raised greatly rather than by a steeper droop value. As a result, new virtual resistance is redefined as:

$$\begin{aligned} R_l &= (1 - R_l) + (R_l Soc) \\ R_s &= 1 - (R_s Soc); \end{aligned} \quad (4.1)$$

Fig.4.19 indicates the new I-V characteristic of the battery. The droop slopes are obtained from (4.1). Fig.4.17 illustrates three modes: constant power mode, droop mode, and idle mode in charging operation corresponding to Fig.4.19. Fig.4.18 shows the simulation results. As can be seen, the grid will draw power from the battery if the PV system is unable to produce the required voltage. As a result, the grid current is negative and the battery SoC decreases as well. After the PV produces a lot of energy, the battery will be charged, which generates a positive grid current and rise the battery's SoC.



(a)

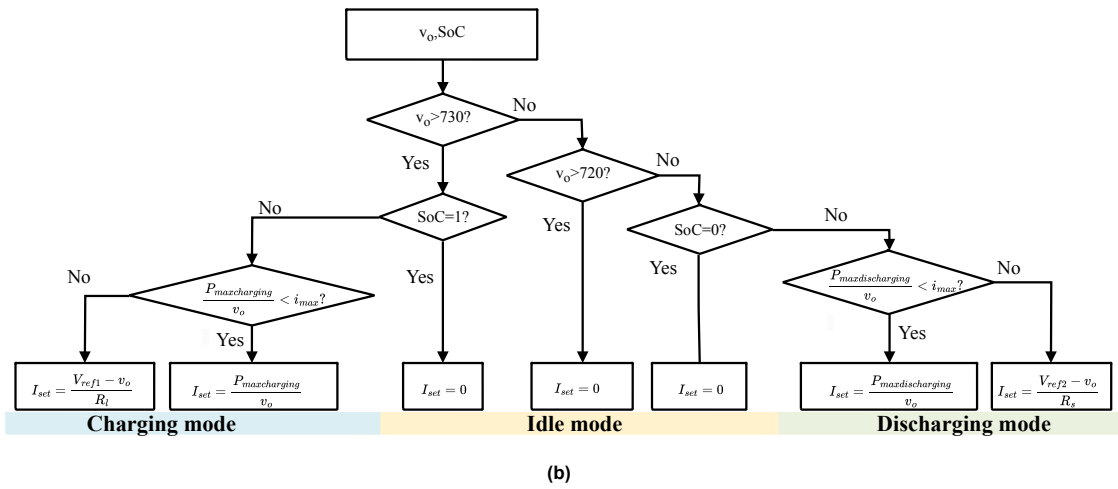


Figure 4.16: Droop control for the battery buck-boost converter (a) Block diagram (b) Droop definition

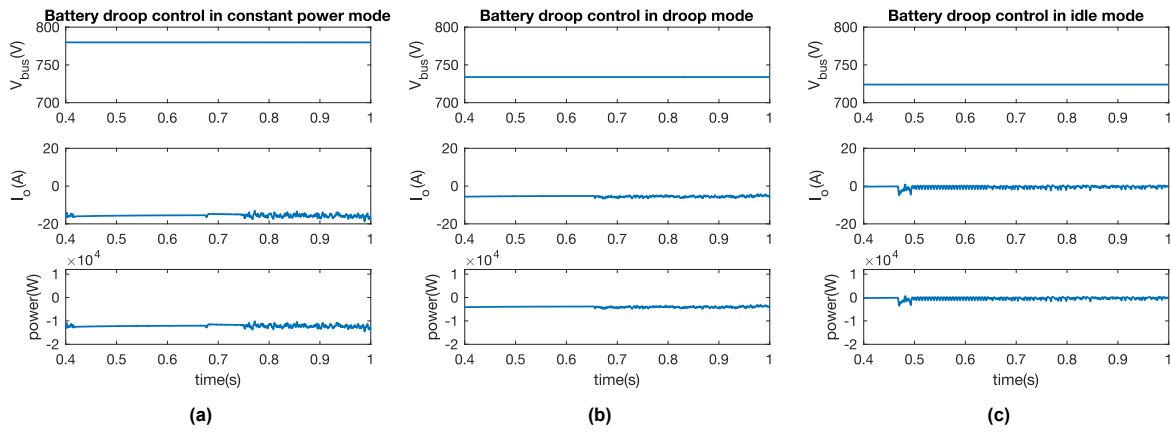


Figure 4.17: Simulation results for the battery buck-boost converter charging operation modes (a) Constant power mode (b) Droop mode (c) Idle mode

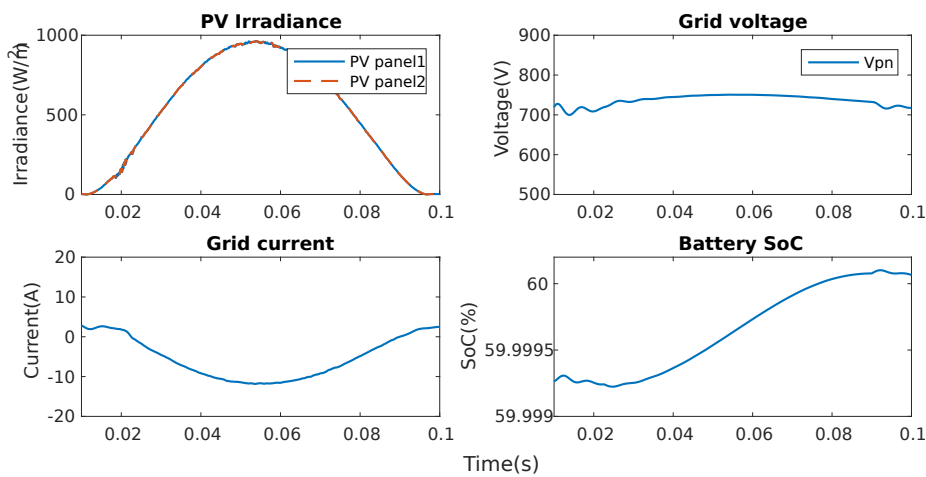


Figure 4.18: Simulation results of battery buck-boost converter with variable PV energy

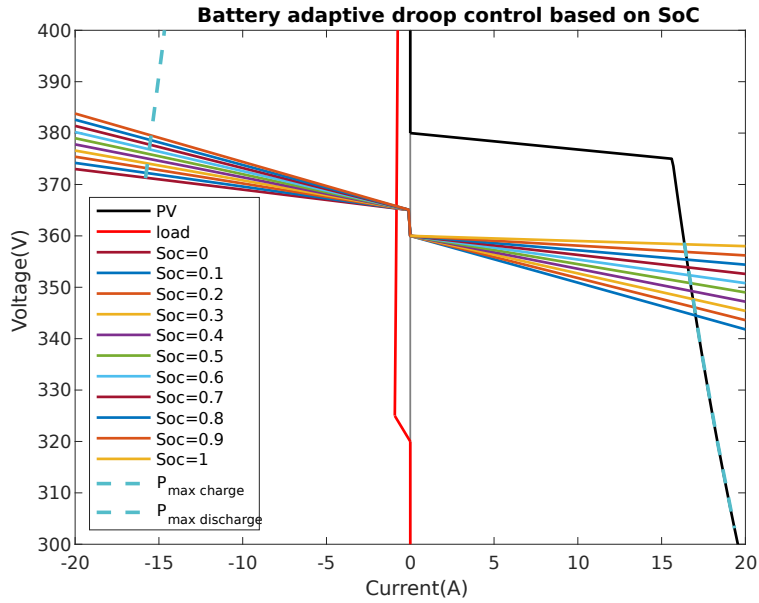


Figure 4.19: I-V characteristic of the battery droop control at different SoC

4.3.5. Solar Charging Station(SCS)

The diagram shown in Fig.4.1 illustrates the configuration of a 24V SCS which is connected to the grid with a DAHB converter as a bridge. The SCS consists of a single PV, an MPPT converter, a battery with a circuit breaker, and a power bank including a buck-boost converter and a 60W battery shown in Fig.4.20. In this configuration, a single PV panel is connected to an MPPT converter to generate PV energy. If the bus voltage of the SCS exceeds 24V, the single battery can be charged, otherwise, the battery will charge the bus. The MPPT converter's topology is depicted in Figure 4.21, and an interleaved buck converter is implemented due to its ability to minimize ripple currents. The control strategy for the MPPT converter remains consistent with the previous approach. In the simulation shown in Fig.4.22, a 60W power bank is used as the load. The irradiance of the PV panel drops three times and when it decreases to 0 battery supplies SCS. The power bank is capable of charging at 60W at a variable bus voltage.

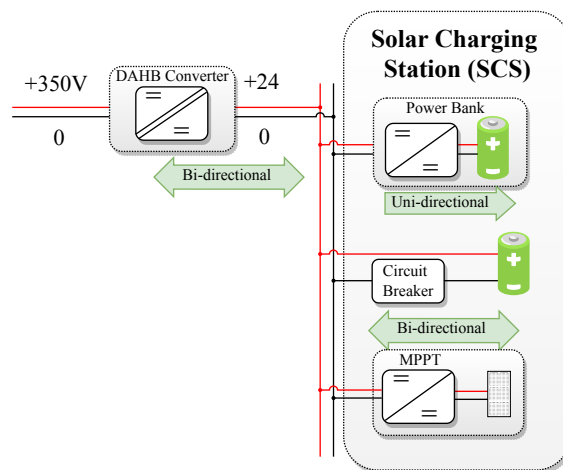


Figure 4.20: 24V SCS schematic consists of an MPPT converter, a single battery, and a power bank as a load

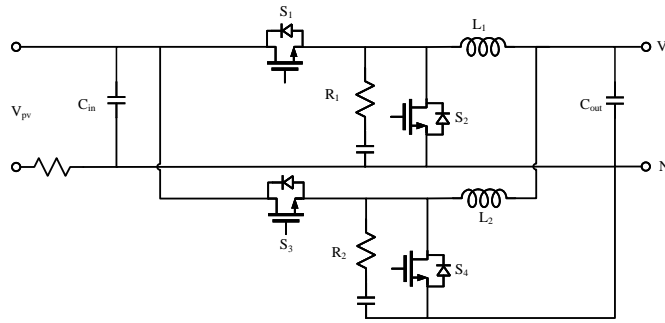


Figure 4.21: SCS-MPPT converter

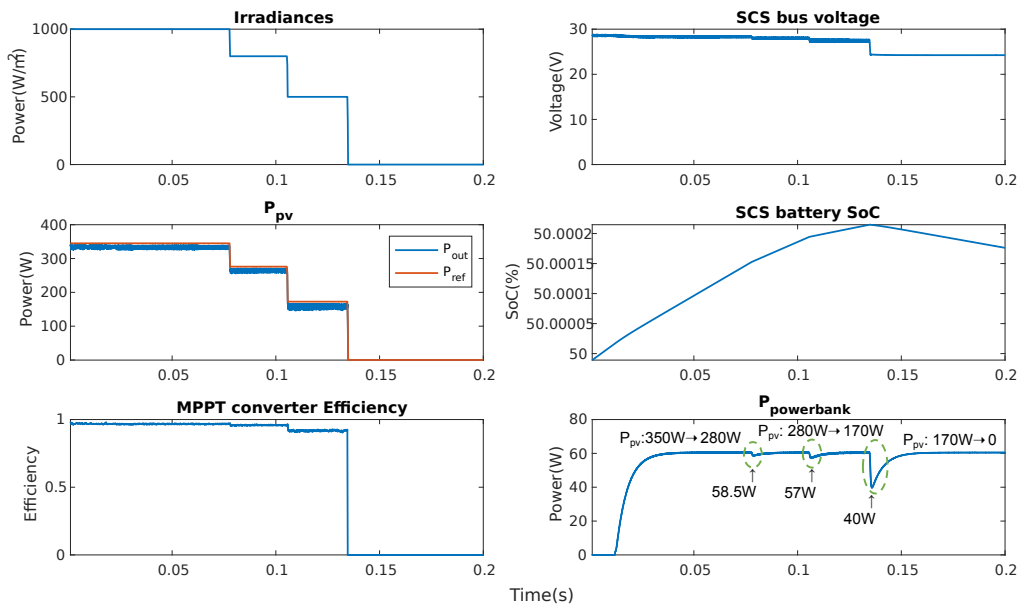


Figure 4.22: Simulation results of the 24V Solar Charging System with variable PV energy

4.4. Conclusion

In this chapter, a 350V bipolar DC microgrid which has the same configuration as the existing grid in the green village is established. For the MPPT converter, a variable step size P&O algorithm is implemented, then a hybrid control combining MPPT and droop control is applied and simulated. To maintain grid voltage under varying irradiance, a voltage balancing converter with droop control is connected. This converter effectively balances the positive(+350V) and negative (-350V)voltage. In addition, two LED strings as the DC loads are connected to the grid.

The grid backup is provided by a 12kW battery equipped with a buck-boost converter. This system operates in five distinct modes: maximum power charging mode, droop charging mode, idle mode, droop discharging mode, and maximum power discharging mode. The specific mode selection depends on the grid voltage. Since it is observed that a battery with a lower SoC has a greater capacity for charging, whereas a higher SoC is beneficial for discharging, a variable droop resistance control strategy based on SoC value is simulated.

A SCS consists of a single PV panel and a battery. The only load in this system is a 60W power bank. Simulation results indicate that the power bank can be charged at its maximum current and maximum power capacity.

5

Converter Controller Design and System Control Design

5.1. Overview

This chapter explores the controller used for the DAHB converter and the DC microgrid. First, a novel controller for DAHB is developed based on the SPS with voltage feedback, ensuring ZVS for a wide range of loads and improving smooth transitioning under variable load conditions. Furthermore, considering the priority of PV energy, followed by batteries, and grid energy as a backup, a coordinated control scheme is designed for a centralized SHS. Comprehensive scenarios and corresponding actions are analyzed. Moreover, given the absence of communication devices in the existing SHS in the Green Village, an alternative coordinated control strategy is proposed. Finally, the performance of the two system-level control schemes is compared and evaluated.

5.2. DAHB

5.2.1. Single phase shift with burst mode operation

Single phase shift

As mentioned above, the modulation of DAHB is a single phase shift control as shown in Fig.5.1¹. With the voltage difference through the PI controller, a phase shift is generated, which drives single phase shift modulation and generates gate signals for the primary and secondary switches. However, the curve $D_b = 1.0$ in Fig.5.2 indicates the converter will operate at a lower phase shift under light loads. As discussed in Section 3.4.3, when there is a large voltage variation at the input or output, the ZVS range may be lost.

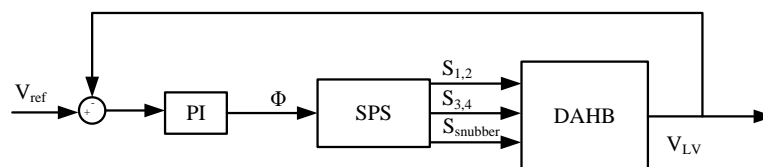


Figure 5.1: Single Phase Shift(SPS) control with voltage feedback block diagram

¹SPS with cascade PI control scheme is shown in Appendix A

Burst mode regulation the output power through ϕ and D_b . It's important to emphasize that for proper zero voltage switching (ZVS), DAHB operation necessitates a substantial ϕ value. Hence, when the load power diminishes, the P_o curve can transition to a distinct step to maintain a significant ϕ , as depicted in Figure 5.2. Burst mode active power can be expressed as follows:

$$P_b = \frac{nV_{HV}V_{LV}\Phi(1-|\Phi|)D_b}{4f_sL_s} \quad (5.1)$$

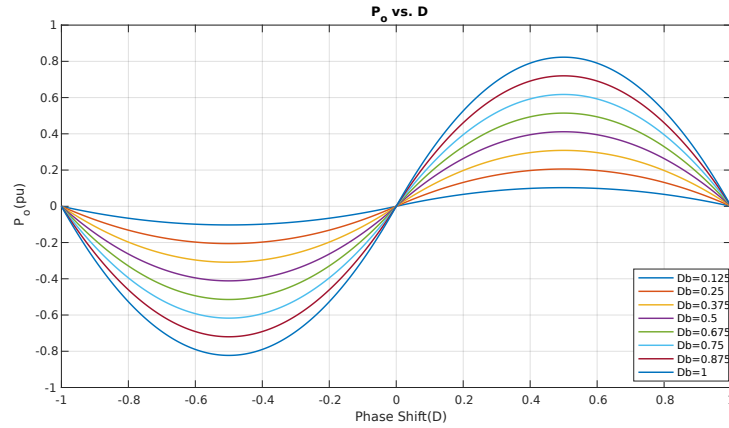


Figure 5.2: Power variation with burst duty cycle

Burst mode operation

In order to avoid false pulses or incomplete pulses driving the DAHB converter, when implementing burst mode operation, the following two conditions must be satisfied.

- The burst mode control frequency must be an integral multiple of the DAHB converter's switching frequency.
- In burst mode, burst on time should contain multiple complete pulses.

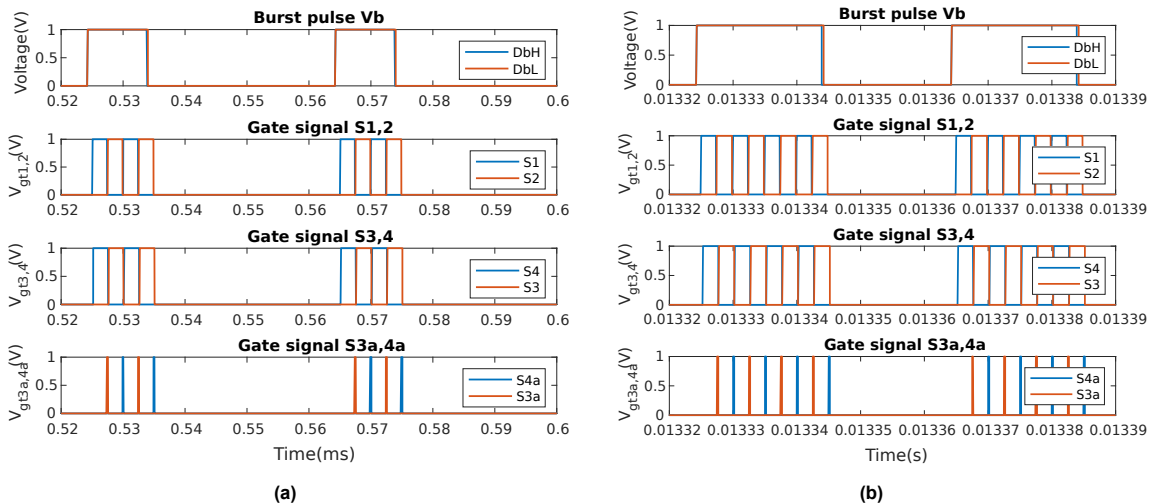


Figure 5.3: Single Phase Shift (SPS) with burst mode (a) $D_b=0.25$ (b) $D_b=0.5$

Since f_s is 200KHz, the burst mode frequency is 25KHz in this project, and 8 pulses are assumed to

represent a full pulse. Fig.5.3 illustrates the gate signal in burst mode operation. (a) shows two pulses for the primary and secondary sides of the converter, and (b) shows four pulses.

5.2.2. Dynamic burst mode control strategy

In the previous section, a fixed burst duty cycle has been employed. However, when extending burst mode to a dynamic setting, both the phase shift and burst duty ratio will undergo alterations. To achieve smooth transitions, a new control strategy is proposed. The control block diagram is shown below. If the phase shift Φ is within the range of minimum and maximum phase shifts, the burst duty ratio D_b will remain constant and the phase shift implemented in the converter switches will correspond to the output of the PI controller. However, once Φ reaches the maximum or minimum phase shift, the D_b will increase by one step (or decrease), and the Φ will reset to an initial phase to maintain the consistent power flowing during and after switching. The initial phase shift value is shown in tab.5.1.

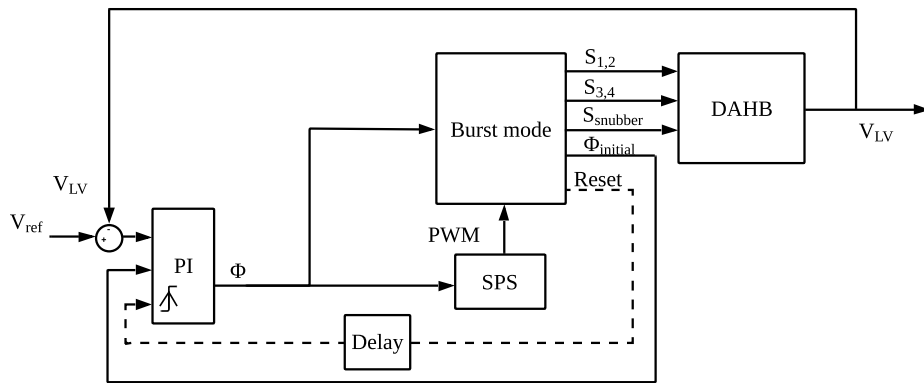


Figure 5.4: Novel burst mode with reset phase and SPS hybrid control method block diagram

Hysteresis

A hysteresis band is added to prevent bouncing when the D_b increments or decrements by one step [55]. Fig.5.5 illustrates the working principle of a hysteresis band, where the maximum phase shift is obtained from (3.16). If Φ reaches maximum phase shift under the current burst duty ratio, D_{b2} increases one step to D_{b3} , and Φ will be reset to the initial value. On the contrary, as Φ decreases to the initial value, D_b maintains its previous value. Only when Φ reaches the threshold of Φ_{min} , D_b transitions from its previous value (D_{b3}) to a lower value (D_{b2}).

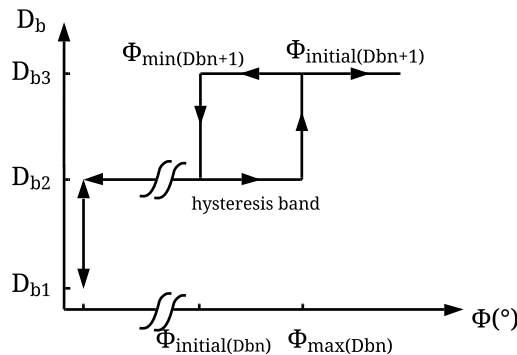


Figure 5.5: Transition points between switching modes of proposed control technique

Initial phase shift

As previously mentioned, whenever the burst duty ratio has a transition, the phase shift should be reset to an initial value to ensure consistent power flow through the DAHB converter during the switching process. Consequently, the key is to determine the appropriate initial phase values for each burst duty ratio. By analyzing Equation 3.16 and Equation 5.1, the initial phase can be calculated to substitute the corresponding burst duty ratio. Tab.5.1 provides a comprehensive summary of all initial phases associated with increasing and decreasing burst duty ratios. The step control methodology comprises a hysteresis band and the use of these initial phases, as illustrated in Figure 5.6.

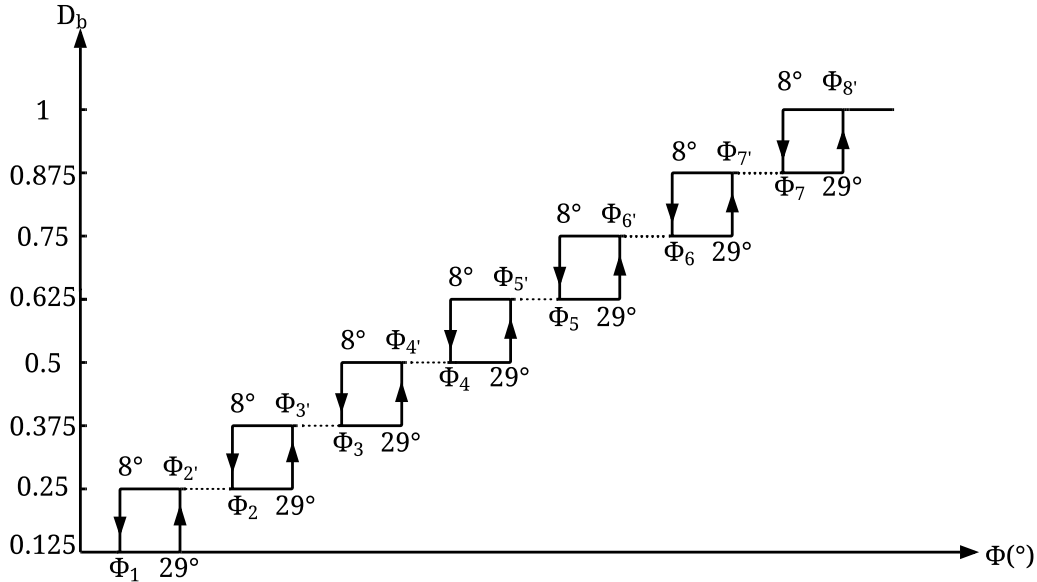


Figure 5.6: Hysteresis control scheme for burst mode operation

Table 5.1: Initial phase for dynamic burst operation

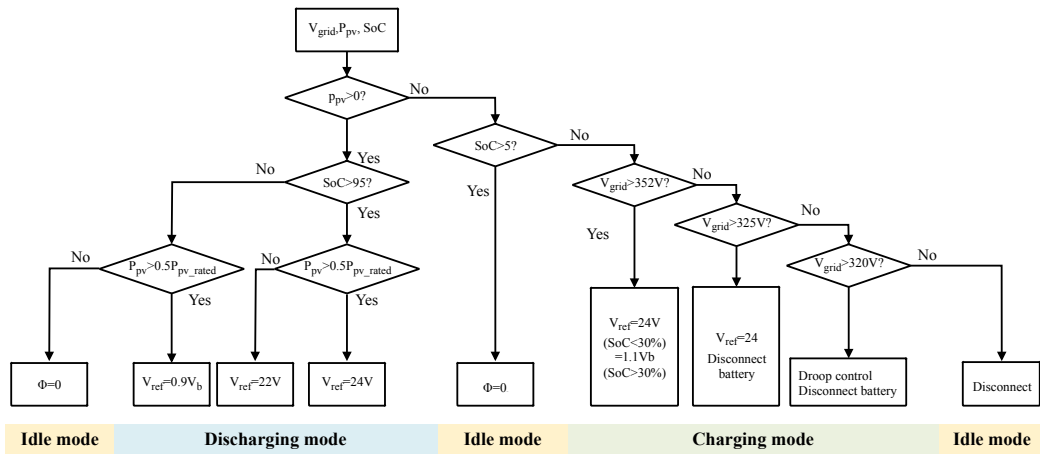
D_b increase	$\Phi_{max} (^{\circ})$	$\Phi_{initial} (^{\circ})$	D_b decrease	$\Phi_{initial} (^{\circ})$	$\Phi_{min} (^{\circ})$
0.125→0.25	30	$\Phi_{2'}=8.3893$	0.25→0.125	$\Phi_1=16.852$	8
0.25→0.375	30	$\Phi_{3'}=12.1056$	0.375→0.25	$\Phi_2=12.2956$	8
0.375→0.5	30	$\Phi_{4'}=14.3207$	0.5→0.375	$\Phi_3=10.8351$	8
0.5→0.625	30	$\Phi_{5'}=15.8324$	0.625→0.5	$\Phi_4=10.1148$	8
0.625→0.75	30	$\Phi_{6'}=16.9481$	0.75→0.625	$\Phi_5=9.6858$	8
0.75→0.875	30	$\Phi_{7'}=17.8152$	0.875→0.75	$\Phi_6=9.401$	8
0.875→1	30	$\Phi_{8'}=18.5141$	1→0.875	$\Phi_7=9.1982$	8

It is important to know that the output of PI controllers cannot instantaneously change since there is an integral process. Consequently, when the phase is reset to an initial value, it is necessary to provide a certain amount of time for the PI controller to respond and integral from this new initial phase shift. Otherwise, the PI controller will be reset by the current value and generate the wrong spike. Therefore, a delay block is applied in the simulation. In a digitally controlled DC/DC converter, the PI controller can store the current phase shift and output from the initial phase.

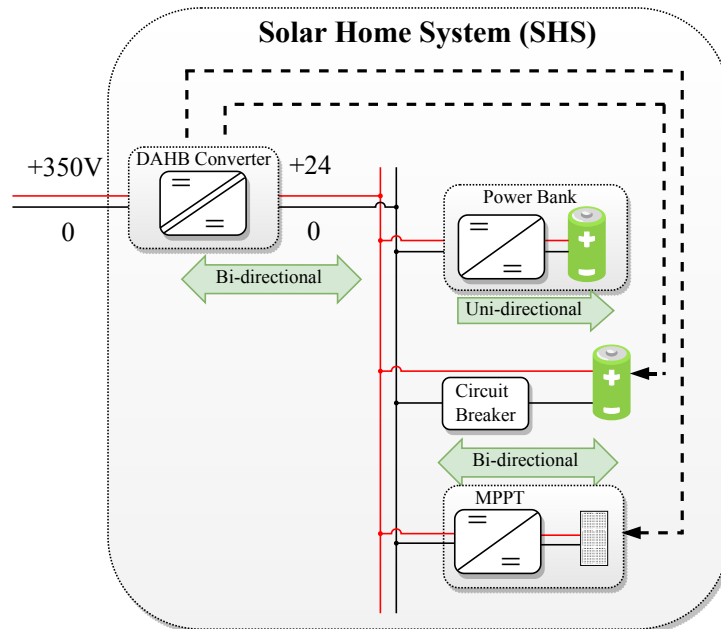
5.3. Coordinated Control

5.3.1. Decentralized control with centralized SHS

A decentralized control system with a centralized Solar Home System (SHS), is developed to effectively prioritize renewable sources in SCS. Within this framework in Fig.5.7a, the SCS employs a prioritization scheme in which PV energy takes precedence and the second is battery energy and DC microgrid is used as a backup to ensure the rated operation of the power bank. On the one hand, if the SCS battery reaches full capacity, DAHB will supply power to the grid if there is remaining PV energy. On the other hand, during night, when PV energy is unavailable, DAHB will take the grid power when the SCS battery is almost empty. Subsequently, if the grid has enough energy, both the power bank and the battery are charged. However, if the grid energy levels are moderate, only the power bank is charging, given its higher priority. In the event of low grid voltage, the DAHB converter closes the switch, thereby disconnecting the solar charging station from the grid.



(a)



(b)

Figure 5.7: Decentralized control with centralized SHS

The possible operation scenarios are explained as follows.

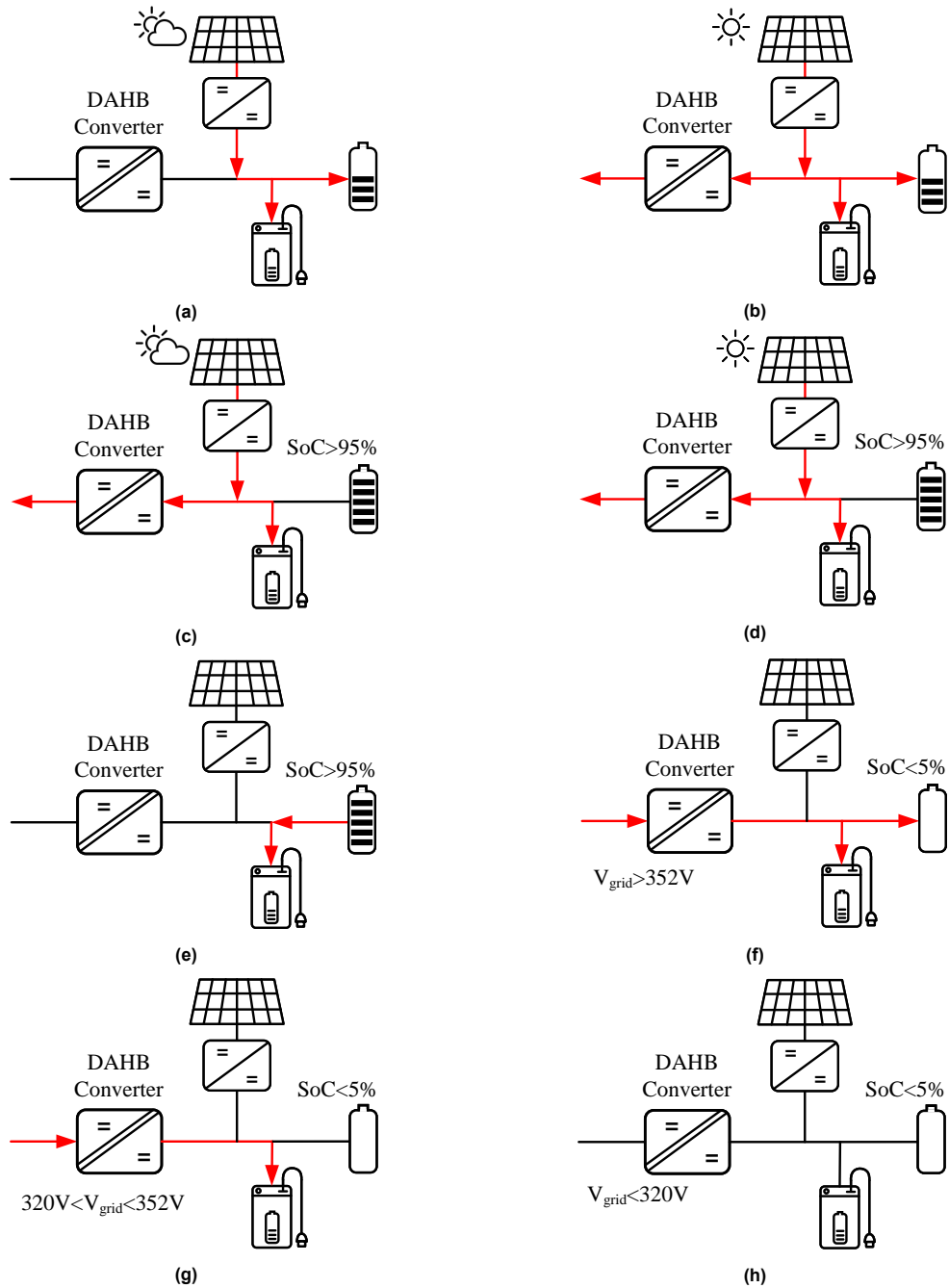


Figure 5.8: Possible operation scenarios (a) Partially sufficient PV energy (b) Sufficient PV energy (c) Partially sufficient PV energy with a full battery (d) Sufficient PV energy with a full battery (e) No PV energy and a full battery (f) No PV energy and an empty battery with the high grid voltage (g) No PV energy and an empty battery with the middle grid voltage (h) No PV energy and an empty battery with the low grid voltage

Fig.5.8 presents a comprehensive description of potential scenarios, while Tab.5.2 illustrates corresponding decision-making processes. An observation can be found that certain decision-making is influenced by the state of the SCS battery, therefore, it is necessary to coordinate between the DAHB converter and the SCS battery. Consequently, the establishment of inner communication between the DAHB converter and the battery in SHS becomes important. This communication loop is defined and illustrated in Fig.5.7b.

Table 5.2: Possible operation scenarios and decision making for centralized SHS

Scenarios	SHS conditions	DC Microgrid voltage	Decision-making
(a)	PV energy: Middle Battery: Not full	320V-380V	Charge power bank and battery
(b)	PV energy: High Battery: Not full	320V-380V	Charge power bank and battery Supply power to the grid
(c)	PV energy: Middle Battery: Fully charged	320V-380V	Charge power bank Supply power to the grid
(d)	PV energy: High Battery: Fully charged	320V-380V	Charge power bank Supply power to the grid
(e)	PV energy: None Battery: Fully charged	320V-380V	Battery discharges power bank
(f)	PV energy: None Battery: Empty	$V_{grid} > 352V$	Grid charges power bank and battery
(g)	PV energy: None Battery: Empty	320V-352V	Grid charges power bank Disconnect battery
(h)	PV energy: None Battery: Empty	$V_{grid} < 320$	Disconnect SCS

5.3.2. Decentralized control with decentralized SHS

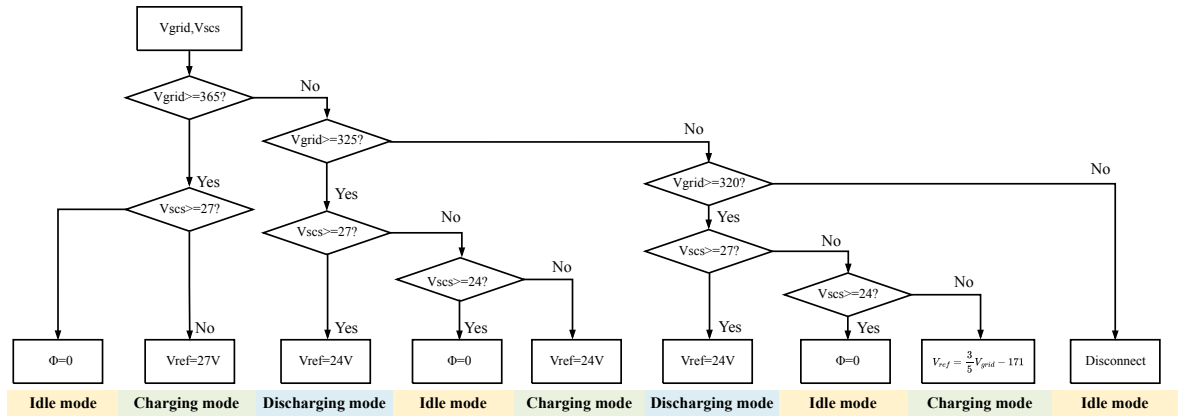
As the SHS system in the Green Village is decentralized, there is no communication coordination operation between the DAHB converter and SCS. Therefore, based on the collaborative control described above, a decentralized control strategy is proposed that regards SCS and DAHB as independent components.

The estimation of the battery state relies on the SCS bus voltage. The PV energy range typically ranges from 24V to 28V, with a battery voltage of 21V indicating an empty state and a voltage of 29V being fully charged. Consequently, when the SCS voltage surpasses 27V, it indicates an approximately fully charged battery. Conversely, if the SCS voltage falls within the 24V-28V range, it shows a moderate PV energy level or a battery with SOC in 40% - 90%. Therefore, the control methodology proposes a method of estimating the voltage difference between the rated and actual voltages. If the grid or SCS voltage significantly deviates from the rated voltage, the converter operates in the charging or discharging mode; otherwise, it remains in the idle mode.

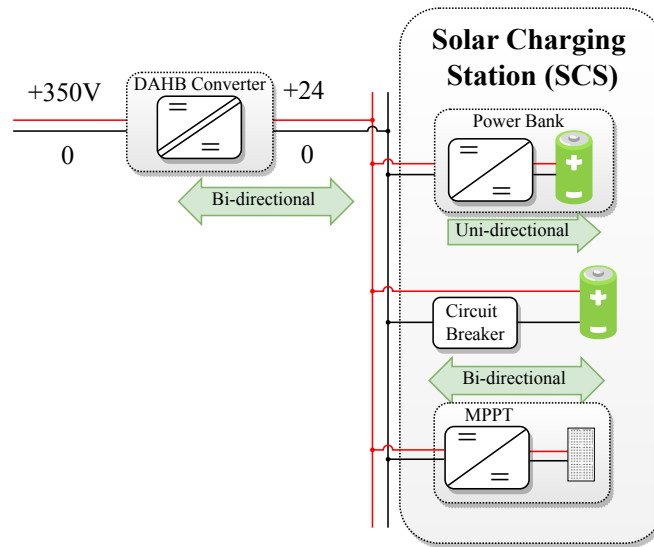
However, because of the lack of communication between the converter and the SCS, the actual state of the battery cannot be determined. Consequently, in situations where the battery is not empty but in a low state, the grid charges SCS. Consequently, the high priority of the power bank can be ensured, but it is uncertain to access the state of the battery.

Table 5.3: Possible operation scenarios and decision making for decentralized SHS

Scenarios	SHS bus voltage	DC Microgrid voltage	Decision making
(a) (b)	$V_{scs} \geq 27$	$V_{grid} \geq 365$	Islanded mode
(c) (d)	$24V < V_{scs} < 27V$	$V_{grid} \geq 365$	Supply power from the grid
(e) (f)	$V_{scs} \geq 27$	$320V < V_{grid} < 365V$	Supply power to the grid
(g) (h)	$24V < V_{scs} < 27V$	$320V < V_{grid} < 365V$	islanded mode
(i) (j)	$V_{scs} \leq 24V$	$320V < V_{grid} < 365V$	Supply power from the grid
(k)	$V_{scs} \geq 21V$	$V_{grid} < 320V$	Supply power to the grid
(l)	$V_{scs} < 21V$	$V_{grid} < 320V$	Islanded mode

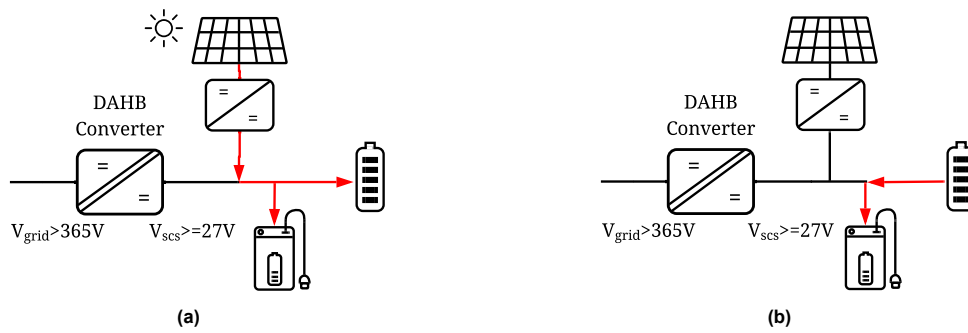


(a)



(b)

Figure 5.9: Decentralized control with decentralized SHS



(a)

(b)

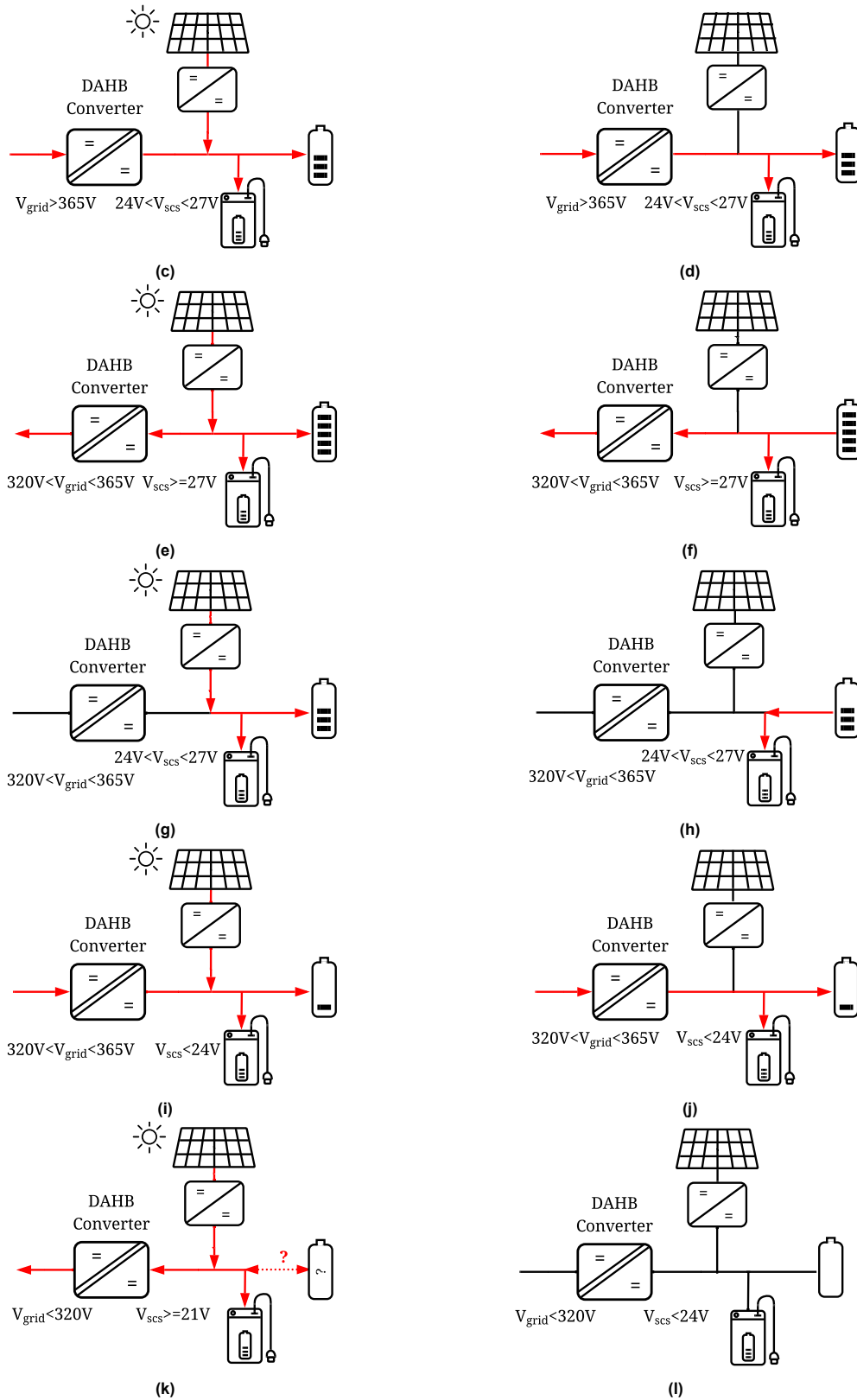


Figure 5.10: Possible operation scenarios (a) Idle mode: High V_{scs} and high V_{grid} with PV energy (b) Idle mode: High V_{scs} and high V_{grid} without PV energy (c) Charging mode: Middle V_{scs} and high V_{grid} with PV energy (d) Charging mode: Middle V_{scs} and high V_{grid} without PV energy (e) Discharging mode: High V_{scs} and medium V_{grid} with PV energy (f) Discharging mode: High V_{scs} and medium V_{grid} without PV energy (g) Idle mode: medium V_{scs} and medium V_{grid} with PV energy (h) Idle mode: medium V_{scs} and medium V_{grid} without PV energy (i) Charging mode: Low V_{scs} and medium V_{grid} with PV energy (j) Charging mode: Low V_{scs} and medium V_{grid} without PV energy (k) Discharging mode: Low V_{scs} and enough V_{grid} with PV energy (l) Idle mode: Low V_{scs} and low V_{grid} without PV energy

Fig.5.10 illustrates possible operation scenarios. Since SHS and DAHB are independent components, DHAB can only access the information on two sides voltage and current. The corresponding decision-making for each scenario is shown in Tab.5.3. It can be seen that the decision is determined by the range of the difference between the voltage at both ends of the converter and the rated voltage. Therefore, the propriety of the power bank can be ensured.

5.3.3. Comparison of two decentralized control

Table 5.4: Comparison of decentralized control with both decentralized and centralized SHS

Objectives	Decentralized control with centralized SHS	Decentralized control with decentralized SHS
Charging power bank	Yes	Yes
SHS hierarchical load supply	Yes	No
Grid energy as a backup	Yes	Yes
Surplus energy fed back to the grid	Yes	Yes
SHS-Battery health	Excellent	Poor
Economy	Low	High
Accessibility	Low	High
Number of converter	High	Low
Robustness	Low	High

A comparison is summarised in Tab.5.4. The first control scheme is beneficial for the hierarchical energy utilization of SHS. This approach allows users to economically access grid power only when the SHS is depleted of battery energy. Additionally, by monitoring the battery's SoC, the control strategy can disconnect the battery from the system upon reaching full capacity, thereby preventing overcharging and promoting battery health. However, this control strategy necessitates the real-time monitoring of battery status components and communication with the DAHB converter. Thereby improving the complexity and cost of the system. In the event of monitor or communication malfunction, such as incorrect reporting of battery status during depletion, the converter may be unable to take energy from the grid, potentially impeding the load from being charged. In contrast, In the second strategy, power flows are determined by the voltage differentials across the converter, making it more user-friendly and ensuring continuous load charging.

5.4. Conclusion

This chapter presents a control strategy developed for the previously modeled DAHB converter. The strategy focuses on expanding the ZVS range with burst mode operation. Considering that dynamic burst duty ratio results in transitions, hysteresis control is used to enhance stability under various load conditions. Additionally, to achieve seamless transitions, the initial phase shifts for each hysteresis band are determined.

Furthermore, a coordinated control scheme is proposed to ensure optimal energy distribution between the grid and SCS. The first coordinated control scheme treats SCS and DAHB converter as a centralized SHS, thus, it is necessary for inner communication and battery state monitoring. Alternatively, a coordinated control strategy is developed for a decentralized SHS, where the SCS and DAHB converters are regarded as independent components. A comparison is made to evaluate the performance of both schemes.

Both control strategies effectively realize load charging in various scenarios. However, the first strategy offers hierarchical energy utilization with increased complexity, while the other one emphasizes accessibility and can be implemented into the existing DC microgrid in the Green Village.

6

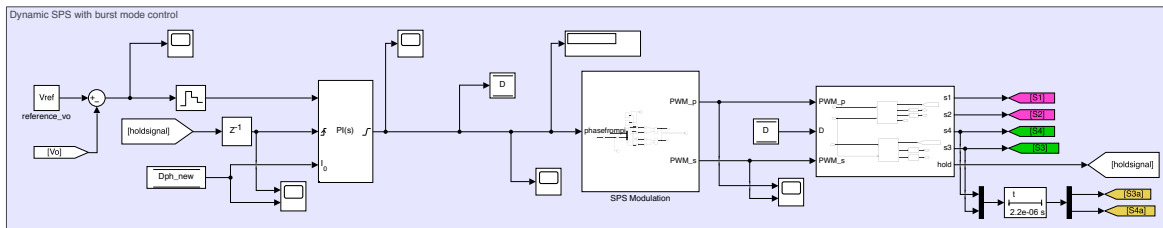
Simulation and Testing Results

6.1. Overview

In this chapter, simulation results and prototype results are shown and analyzed. First, the results of the DAHB simulation verify the performance of the proposed control scheme in steady state and dynamic transitions. The high efficiency of variable load operation demonstrates the performance of this approach. Furthermore, prototype testing for this approach is conducted. Moreover, a model for the DC microgrid is built in Matlab/Simulink and decentralized control is implemented. The simulation results validate the seamless power transition in different scenarios.

6.2. DAHB simulation and testing results

6.2.1. DAHB simulation results



(a)

The model is built in MATLAB/Simulink, as depicted in Fig.6.1. Fig.6.1a illustrates the topology of the model, while Fig.6.1b shows the control block, as defined in the previous chapter 5. As discussed previously, changes in the burst duty ratio lead to a restart of the phase shift. The new phase shift is then passed through an SPS block, generating PWM signals as the fundamental waveforms for the burst mode.

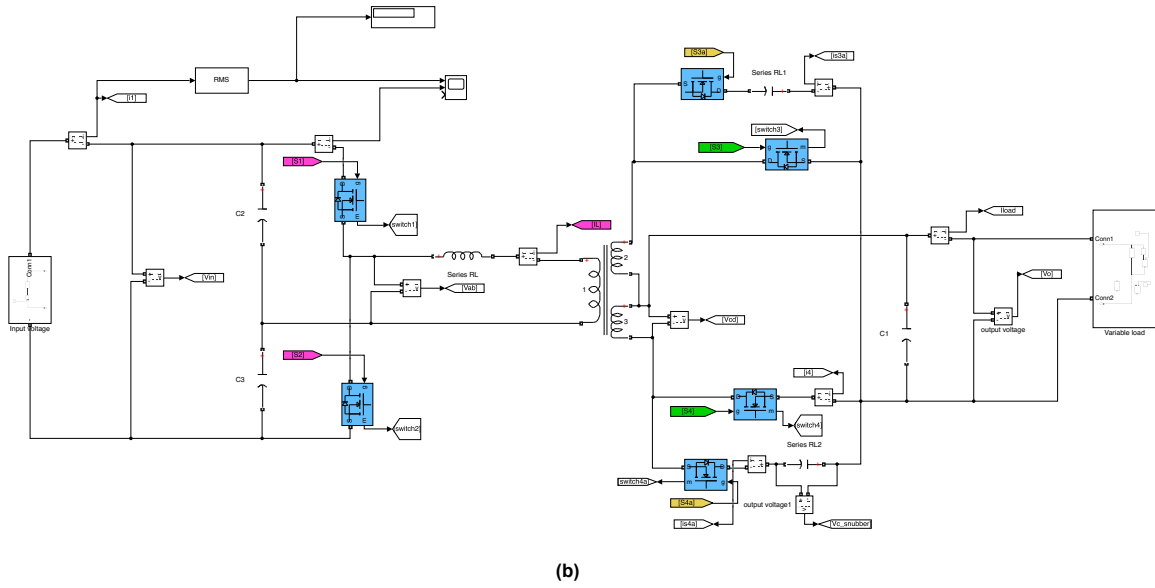


Figure 6.1: Simulation model built in Matlab/Simulink

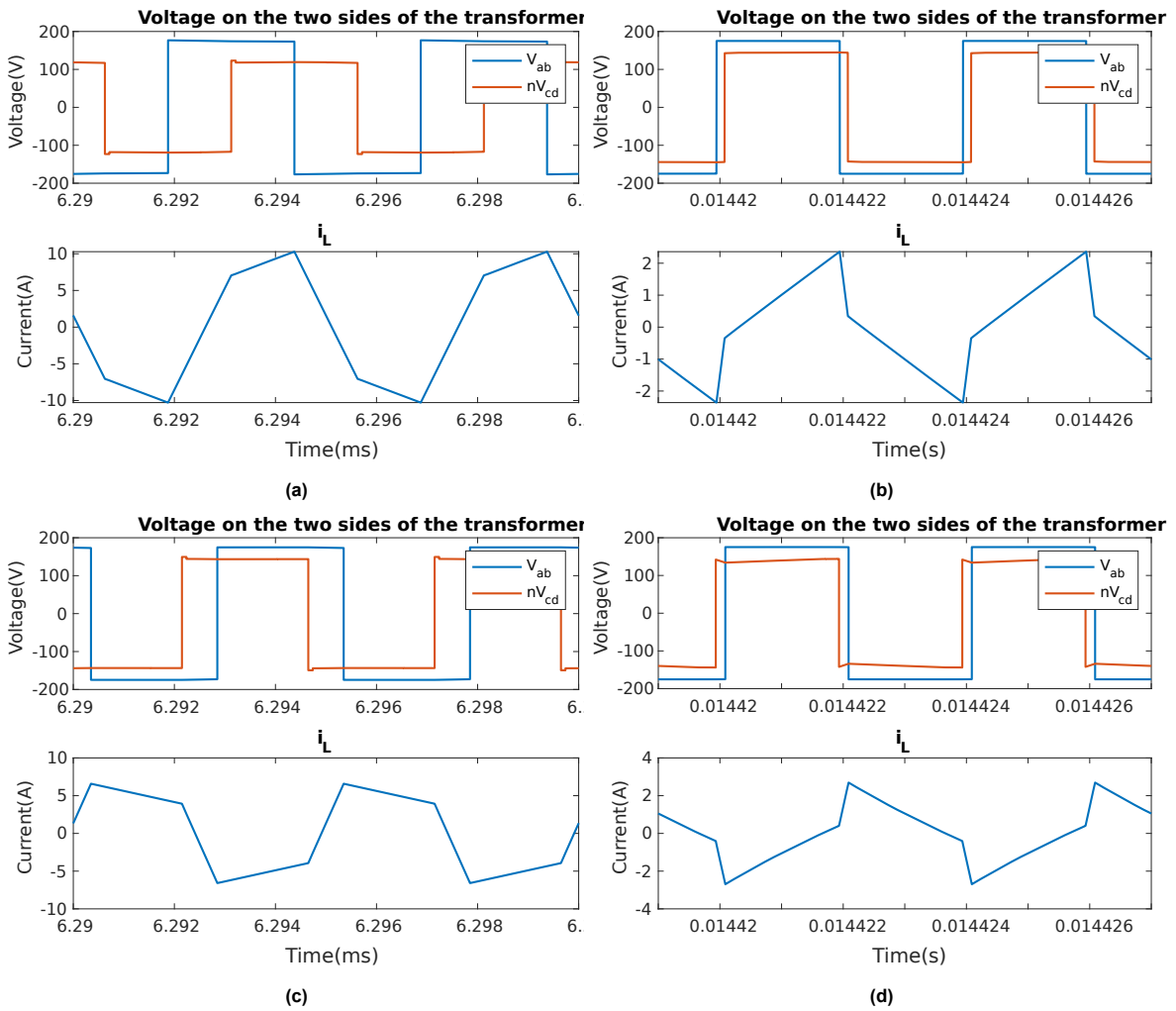


Figure 6.2: Typical DAHB waveforms with Single Phase Shift (SPS) control (a) Charging mode under nominal load (b) Charging mode under light load (c) Discharging mode under nominal load (d) Discharging mode under light load

Fig.6.2 shows the simulation results obtained using Single Phase Shift control during rated load and light load conditions. The controller actively adjusts the phase shift to regulate the output. The inductor current waveform indicates $I_1 I_2 \gg 0$ under rated load conditions, which indicates that the DAHB converter can maintain ZVS. However, under light load conditions, $I_1 I_2 < 0$ for two modes, indicating that either side of the DAHB switches is out of ZVS. In contrast, in Fig. 6.3, during the burst mode turn-on period, the inductor current waveform indicates $I_1 I_2 > 0$. This observation can be explained by the fact the burst duty cycle decreases under light load conditions leading to increasing phase shift, therefore, the ZVS range extends as well.

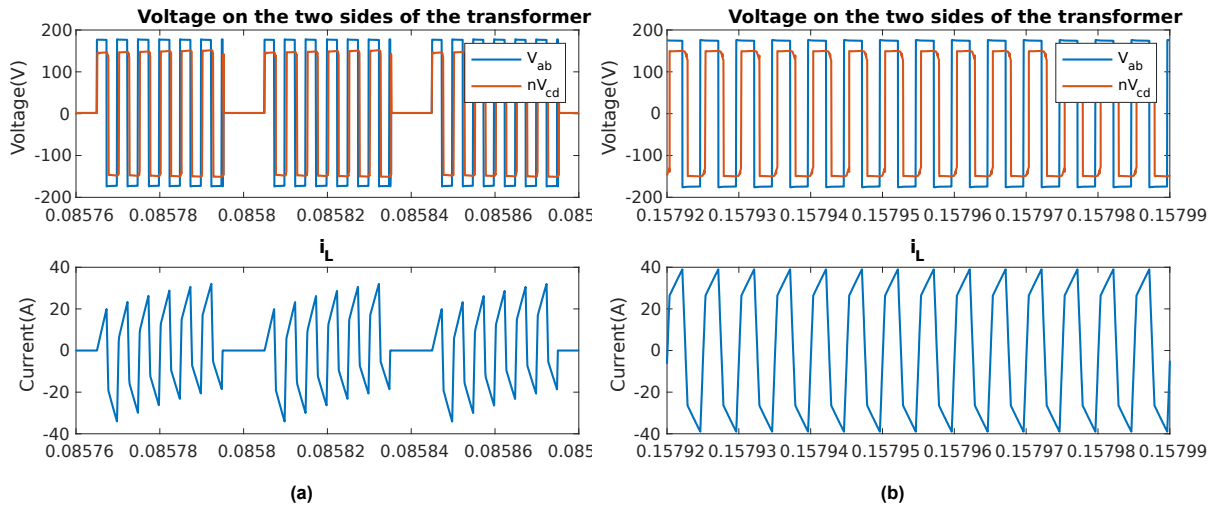
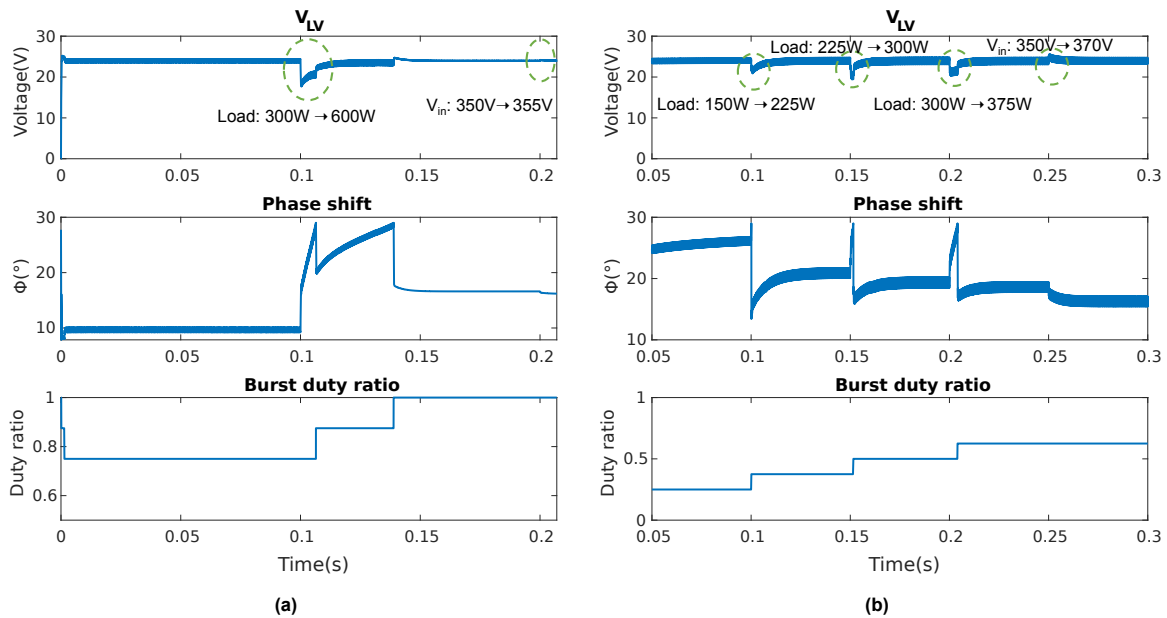


Figure 6.3: Typical DAHB waveforms with dynamic SPS and burst mode control (a) Charging mode under light load (b) Charging mode under nominal load



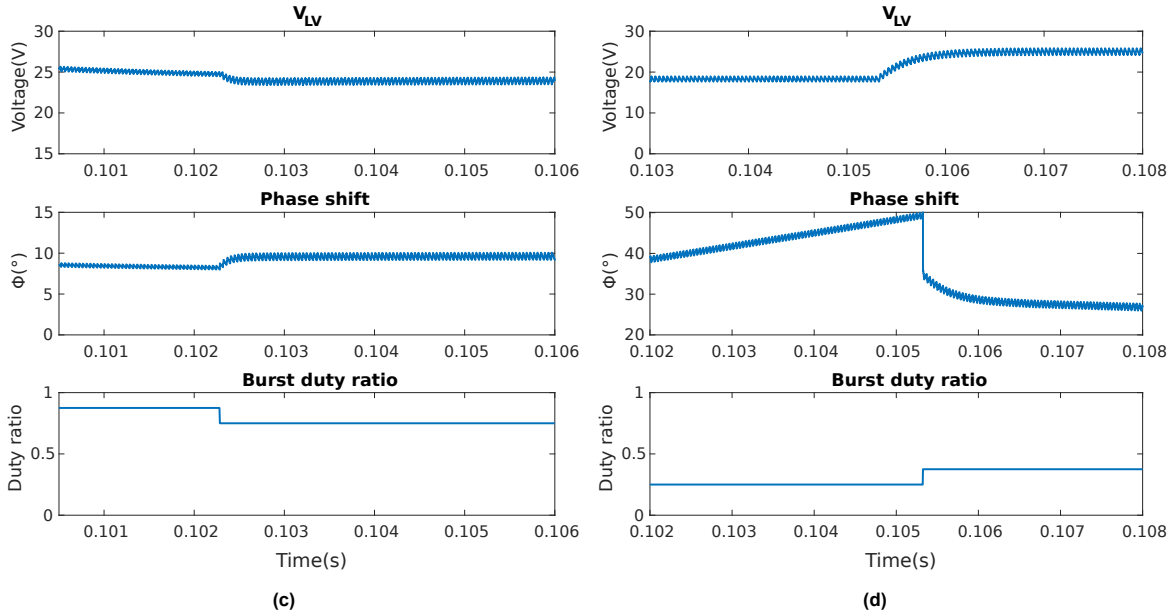


Figure 6.4: Simulation results with approached dynamic SPS and burst mode control (a) Disturbing test1 (b) Disturbing test2 (c) Simulation results when the D_b decrease (c) Simulation results when the D_b increase

To validate the control performance of the introduced hysteresis control method, different disturbing tests are performed as illustrated in Fig.6.4a and Fig.6.4b. At 0.1s, the load power increases from 300W to 600W. Since the output voltage is controlled at 24V, the current flowing through the circuit will increase proportionately. In response, the phase shift increases upon reaching the maximum phase shift, the burst duty ratio step leading to the phase shift is reset to an initial value, then the phase shift increases again until V_o is 24v. In addition, the input voltage rises from 350V to 322V, leading to phase-shift changes. Fig.6.4c and Fig.6.4d show the voltage transitions when the burst duty ratio decreases from 0.875 to 0.75 and increases from 0.25 to 0.375, respectively. In addition, The efficiency of the control strategy is analyzed in Fig.6.5b. It is obvious that the efficiency is higher than 90% with different loads.

A comparison was analyzed between burst mode and burst mode with the initial phase method. The results are depicted in Fig.6.5a. The red line represents the burst mode strategy, while the blue line represents the burst mode with the initial phase strategy.

Observing the graph, it can be seen that at 0.1065s, the burst duty ratio increases, resulting in a spike in both the output voltage and output power, as indicated by the red line. On the other hand, the blue line demonstrates a smooth transition, without any noticeable spikes or disturbances.

$$\eta = \frac{P_{out}}{P_{in}} \times 100\% \quad (6.1)$$

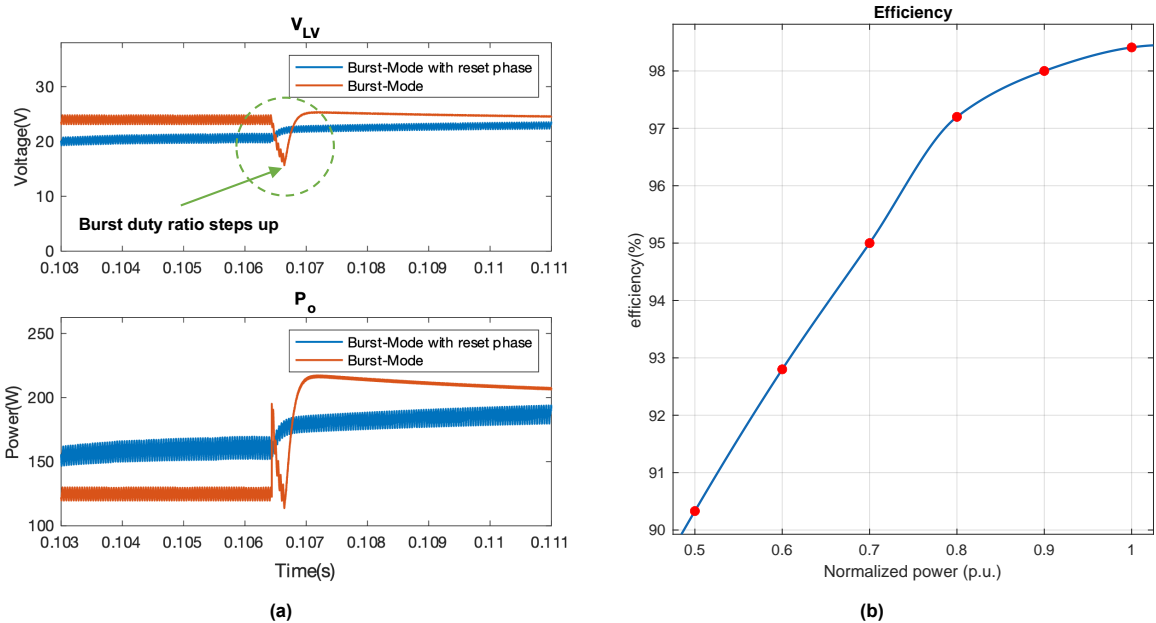


Figure 6.5: Simulation results of the novel burst mode with reset phase and SPS hybrid control method (a) Comparison of burst mode operation and novel burst mode with reset phase and SPS hybrid control method (b)Normalized output power and efficiency of novel burst mode with reset phase and SPS hybrid control method

6.2.2. DAHB prototype testing

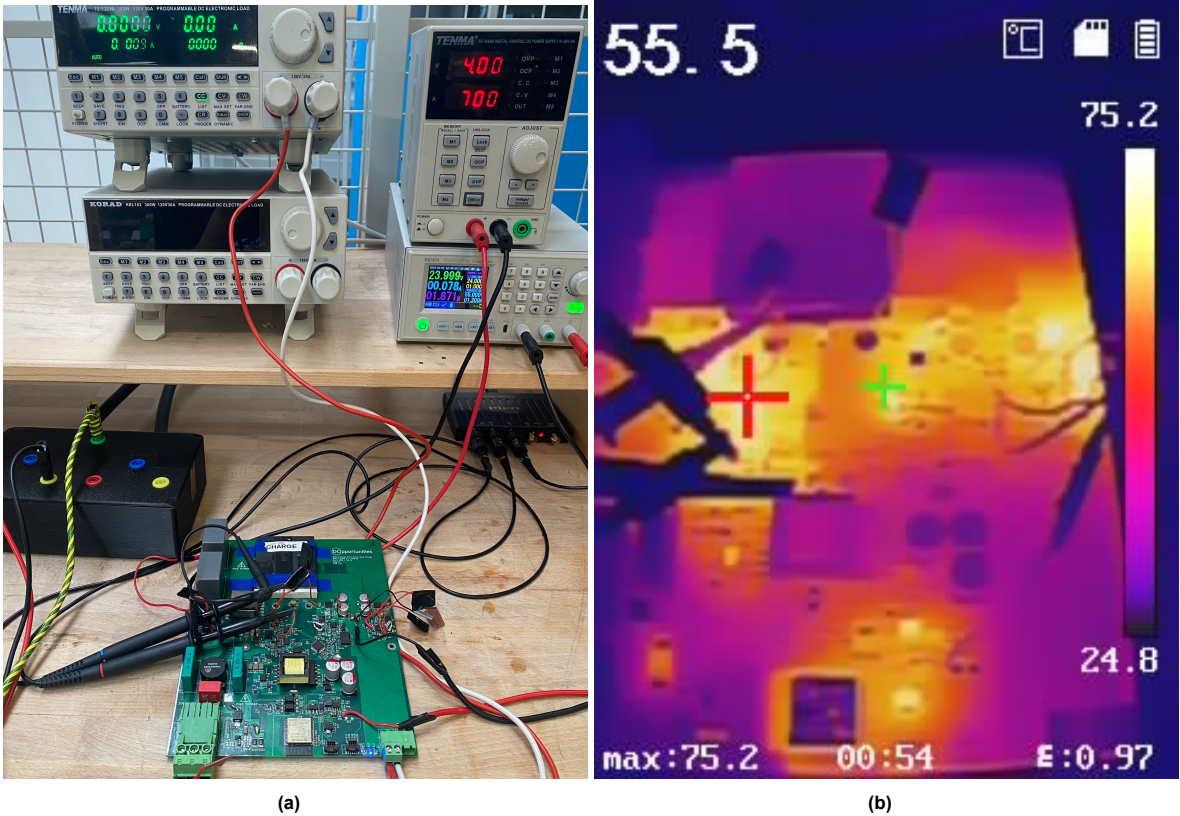


Figure 6.6: Prototype test

SPS with constant burst duty ratio

To validate the performance of the PI control strategy used for the DAHB converter, prototype tests are carried out with the SPS technique and a constant burst duty ratio $D_b = 0.25$. The prototype testing results are in Fig.6.7. During the testing, the input voltage is stepped up from zero to 350V, while the output voltage is regulated at 24V when the input voltage exceeds 175V. Furthermore, when the input voltage is held steady at 350V, variations in the load lead to phase changes and stable output voltage. Fig.6.7 illustrates V_{ds} for the switches and the gate signal.

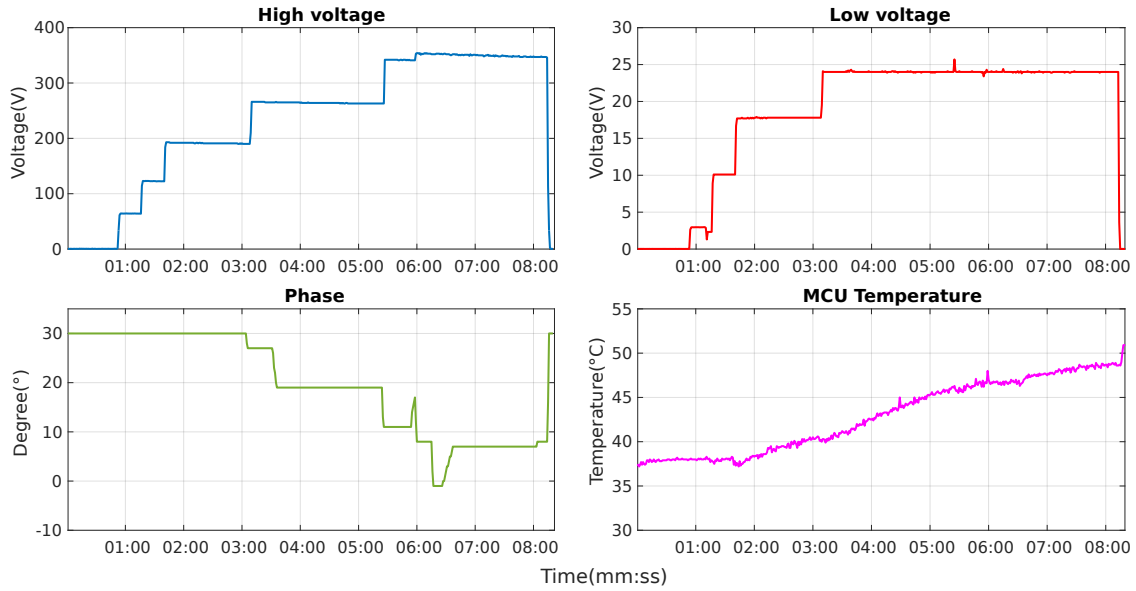


Figure 6.7: SPS with Db=0.25 prototype testing results from Grafana including V_i , V_o , ϕ , and MCU temperature

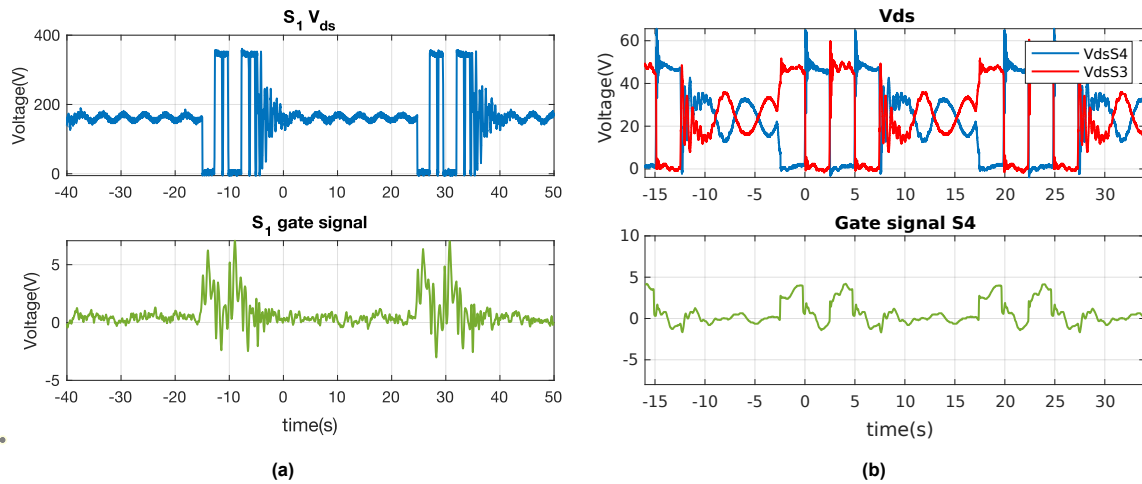


Figure 6.8: SPS with Db=0.25 prototype testing results from Picoscope (a)Primary side switch voltage and gate signal (b) Second side switch voltage and gate signal

SPS with dynamic burst duty ratio

To assess the dynamic performance of the novel burst mode with reset phase and SPS hybrid control method under light load conditions, a prototype test was conducted with an input voltage of 350V and varying load. The test results are presented in Figure 6.9.

Initially, the system was under light load, and subsequently, the load power continued to increase, leading to a corresponding increase in the phase shift. Once the maximum phase value was reached, the phase was reset to its initial value, and the pulse number was increased by one step. Additionally, it was observed that during the pulse number changes, there are no spikes in the output voltage. Thus, the capability of this control methodology to achieve seamless transitions is validated.

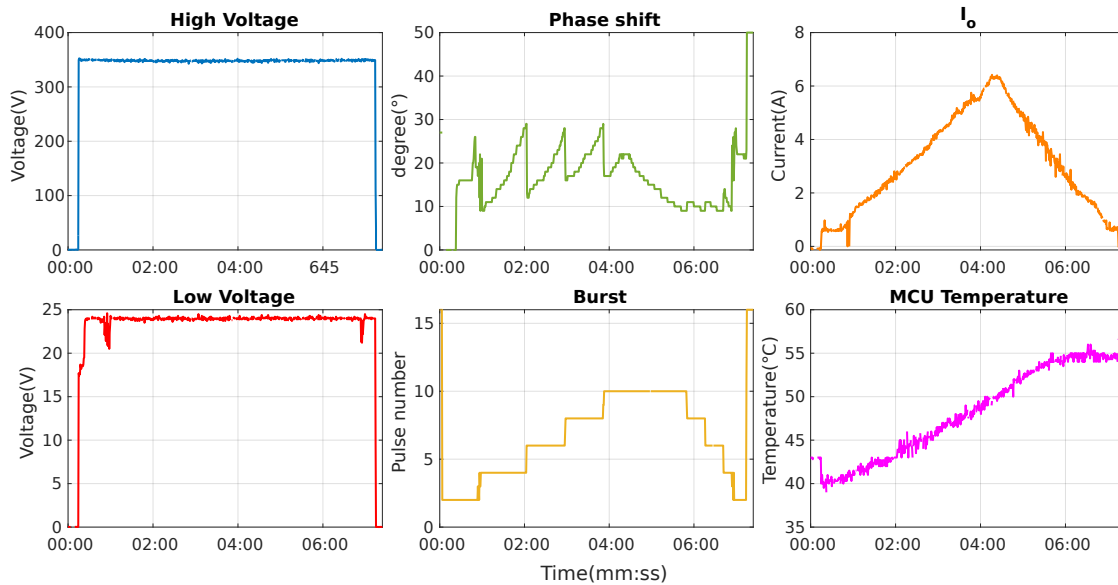


Figure 6.9: SPS with dynamic burst duty ratio prototype testing results ($V_{ref}=24V$) including input voltage, output voltage, phase, pulse number, output current, and MCU temperature

However, there are unstable points when transitioning from a pulse number of 2 to 4. The possible reason is that the system loses ZVS during this particular condition. Since 24V is chosen as the reference voltage, the voltage ratio is not 1 in theory. To substantiate this assumption, an additional test is conducted using a reference voltage of 29V, which ensures that the theoretical voltage ratio is 1. As depicted in Fig.6.10, there is no oscillation transitioning from a pulse number of 2 to 4.

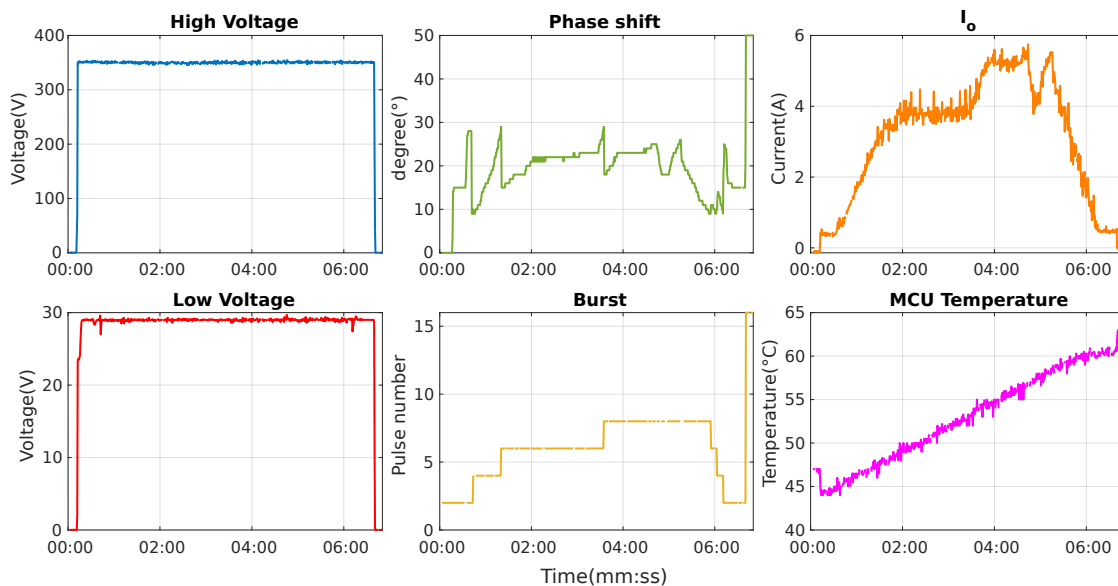


Figure 6.10: SPS with dynamic burst duty ratio prototype testing results ($V_{ref}=29V$) including input voltage, output voltage, phase, pulse number, output current, and MCU temperature

Fig.6.11 above, from top to bottom, show the change of V_{ds} of S1. When $D_b = 0.125$, there is only one pulse; as D_b increases, the pulse number also increases. However, there is a noise that can be observed on V_{ds} , the possible reason is that the dead time is too large. Fig.6.12 is the measured prototype efficiency under light load conditions. The highest efficiency is approximately 87.78%.

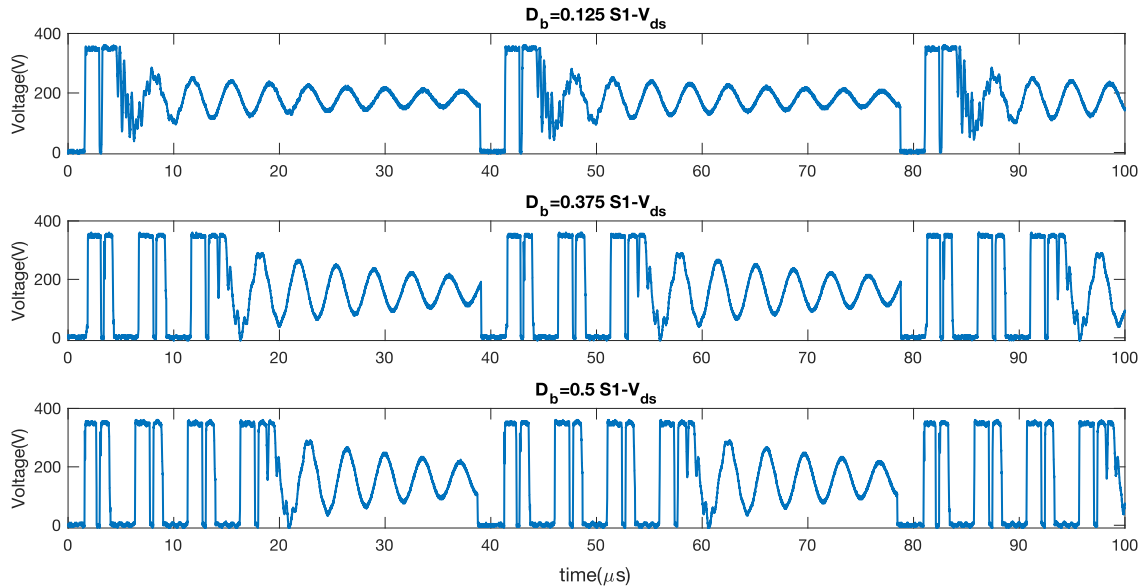


Figure 6.11: V_{ds} of S1 from Picoscope. The figures above, from top to bottom, are $D_b = 0.125$, $D_b = 0.375$ and $D_b = 0.5$

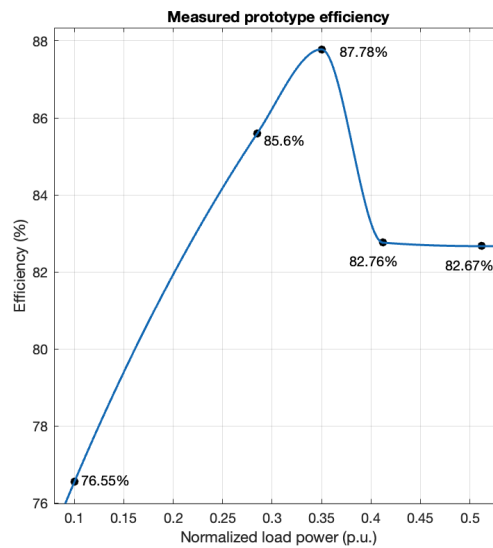


Figure 6.12: Measured prototype efficiency

It is possible to achieve the highest efficiency for a 100W light load (87.78%). As the load power increases, the efficiency can be maintained at more than 82.8%. So far, Fig.6.9 and Fig.6.10 shows the test with $\Phi_{max} = 30^\circ$. Another prototype is tested with $\Phi_{max} = 50^\circ$ and the results are shown in Fig.6.13. However, large voltage spikes in the output voltage is observed during the transition of burst mode. The fact is that the burst mode control remains unchanged until Φ reaches Φ_{max} . Consequently, a larger value of Φ_{max} requires an increased response time for the burst mode control to adapt. Both the simulation and prototype results verify the assumption in Fig.6.14.

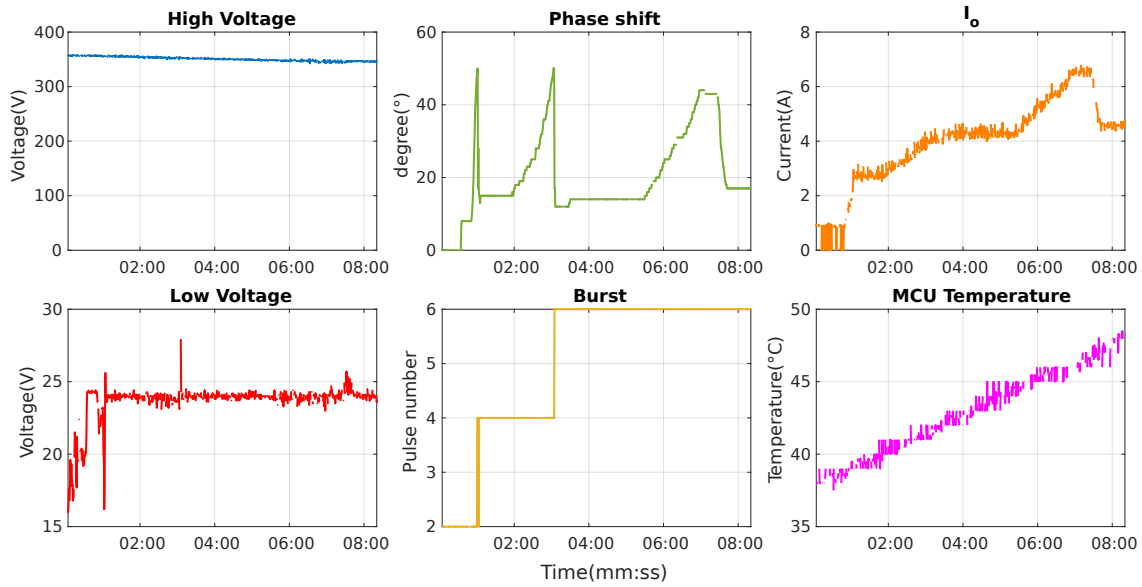


Figure 6.13: SPS with dynamic burst duty ratio prototype testing results ($\phi_{max} = 50^\circ$) including input voltage, output voltage, phase, pulse number, output current, and MCU temperature

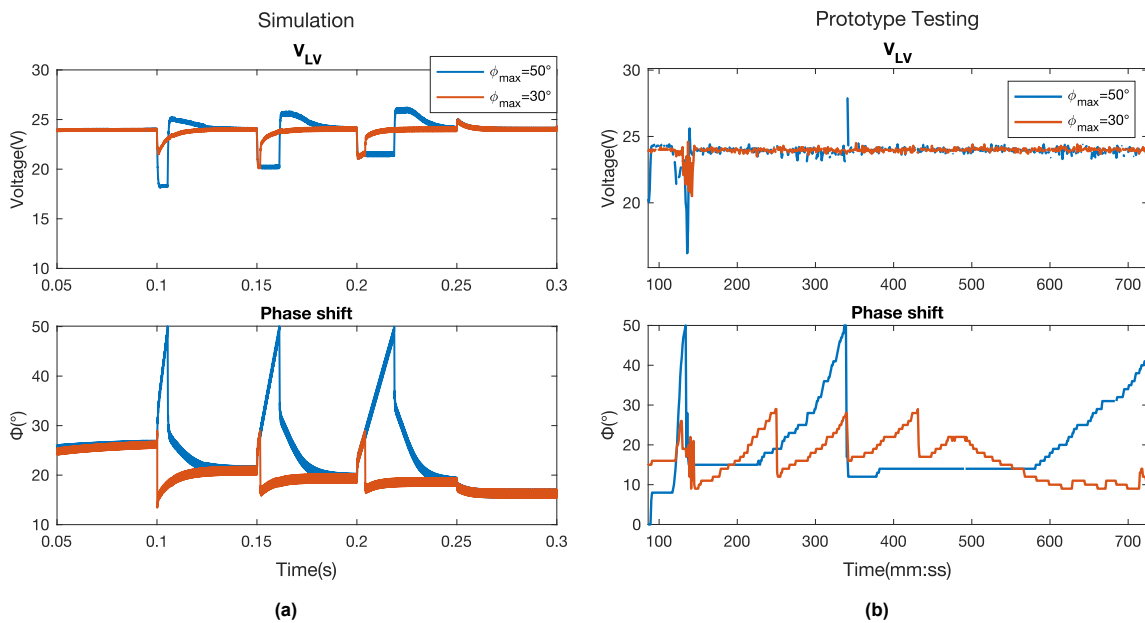


Figure 6.14: Simulation and prototype testing comparison between $\phi_{max} = 30^\circ$ and $\phi_{max} = 50^\circ$ (a) Simulation results (b) Prototype testing results

6.3. DC Microgrid simulation and testing results

6.3.1. DC microgrid simulation results

Fig.6.15 illustrates the bipolar DC microgrid employed in the energy access model constructed within Matlab / Simulink, following the schematic depicted in Fig.4.1. The SCS is connected to the grid via a DAHB converter, wherein the decentralized control scheme is incorporated within the converter's block.

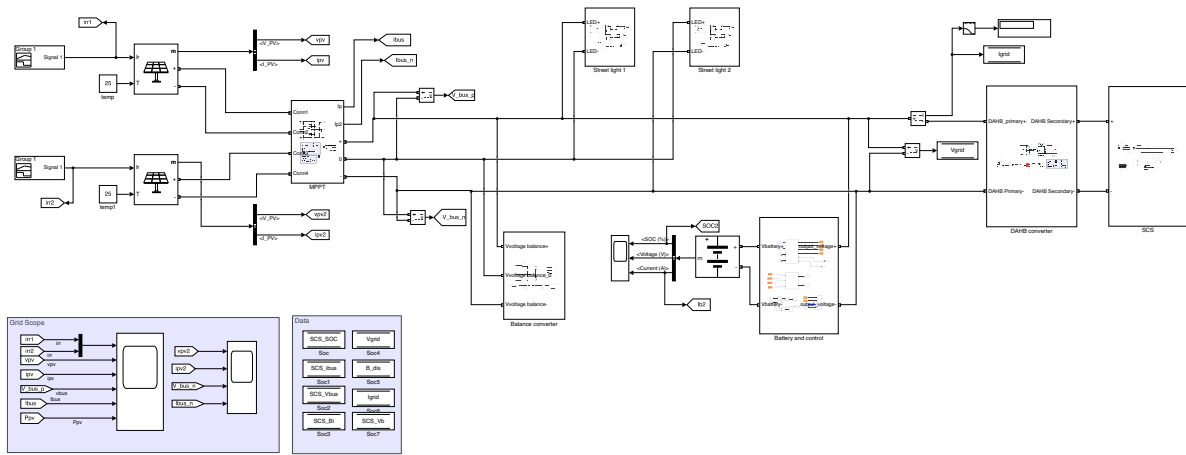
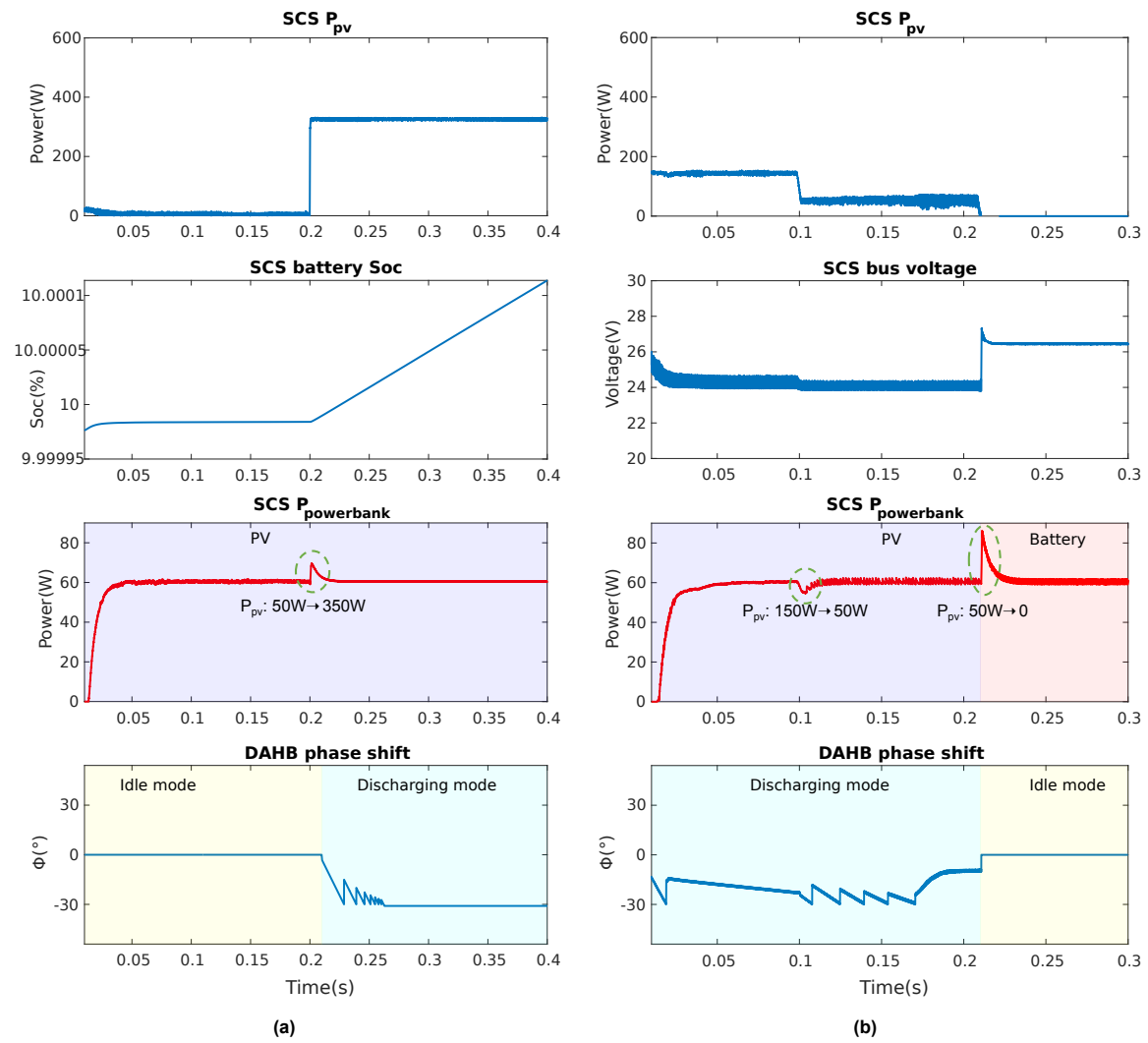


Figure 6.15: DC microgrid model in Matlab/Simulink

Decentralized control with centralized SHS



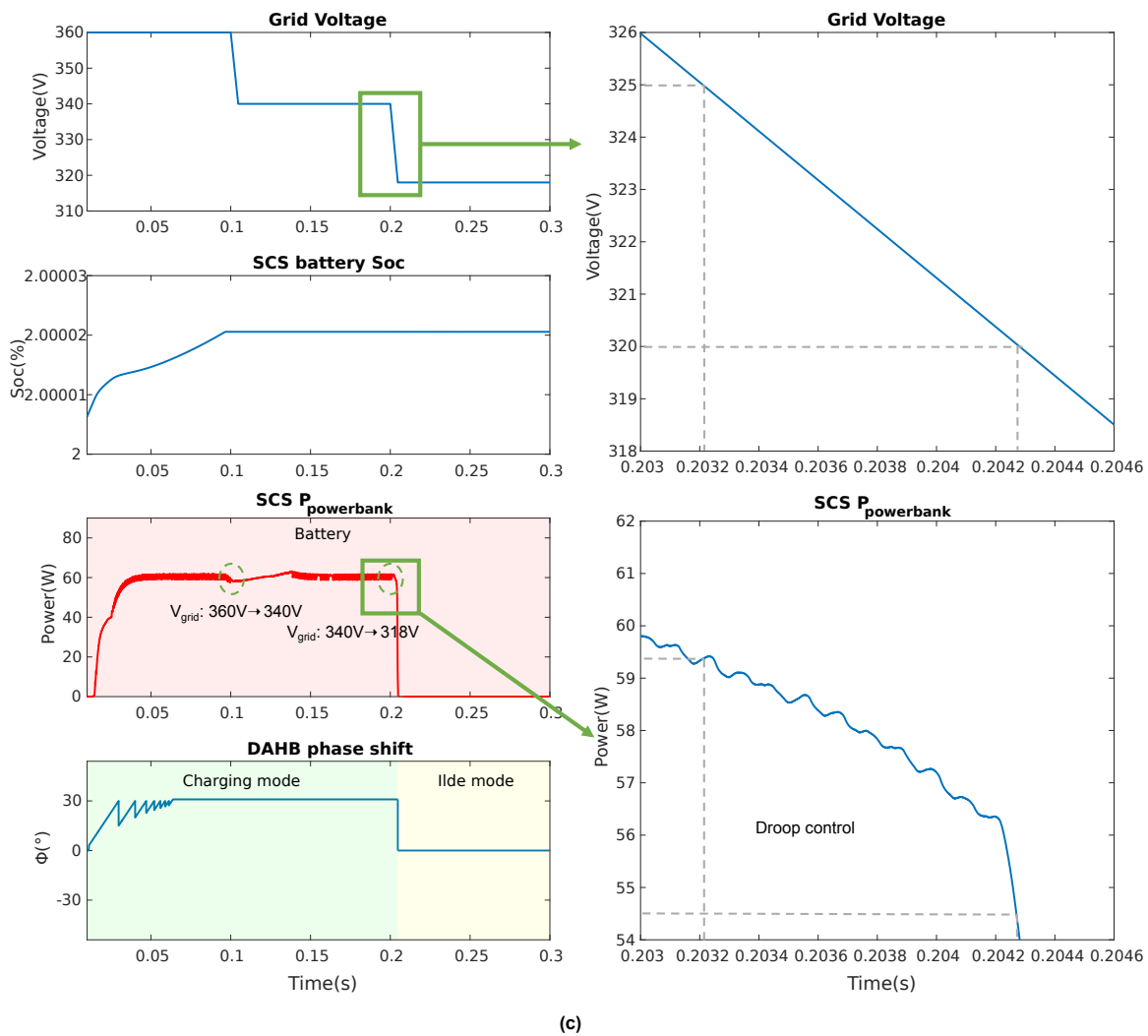


Figure 6.16: Coordinate control with centralized SHS simulation (a) Scenario a and b (b) Scenario c, d and e (c) Scenario f and j

Fig.6.16 shows the simulation results for the possible scenarios Fig.5.8. Figure 6.16a depicts two scenarios (a) and (b). At 0.2s, scenario (a) transitions to scenario (b) due to an increase in PV energy. The SoC of the battery indicates that it charges slowly with low PV energy and rapidly with high PV energy. Additionally, the DAHB converter switches from idle mode to discharging mode at 0.2 s, leading to a negative phase shift.

Figure 6.16b illustrates scenarios (c), (d), and (e). In these scenarios, the SHS battery is fully charged, leading the DAHB converter to discharge the microgrid at different speeds depending on the available PV energy, as evidenced from time 0 to 0.2s. At 0.2 s, the photovoltaic energy decreases to zero in scenario (e). Thus, the SCS battery supplies power to the power bank, while the DAHB converter remains idle.

Figure 6.16c shows charging mode scenarios, denoted as (f), (g), and (h). In these scenarios, the SCS battery is empty, necessitating the microgrid to supply power to the SCS. During the time interval of 0 to 0.1s, the grid voltage is high, resulting in a high SCS bus voltage and rapid charging of the battery. Between 0.1 and 0.2 s, as the grid voltage decreases to a moderate level, the SCS bus voltage also decreases, leading to a stop in battery charging. At time 0.2s, when the grid voltage drops to 325V, the DAHB converter operates in droop mode, causing the SCS bus voltage to decrease to zero until the grid voltage reaches 320V. Subsequently, the SCS disconnects from the grid and the power supplied

to the power bank decreases to zero.

Decentralized control with decentralized SHS

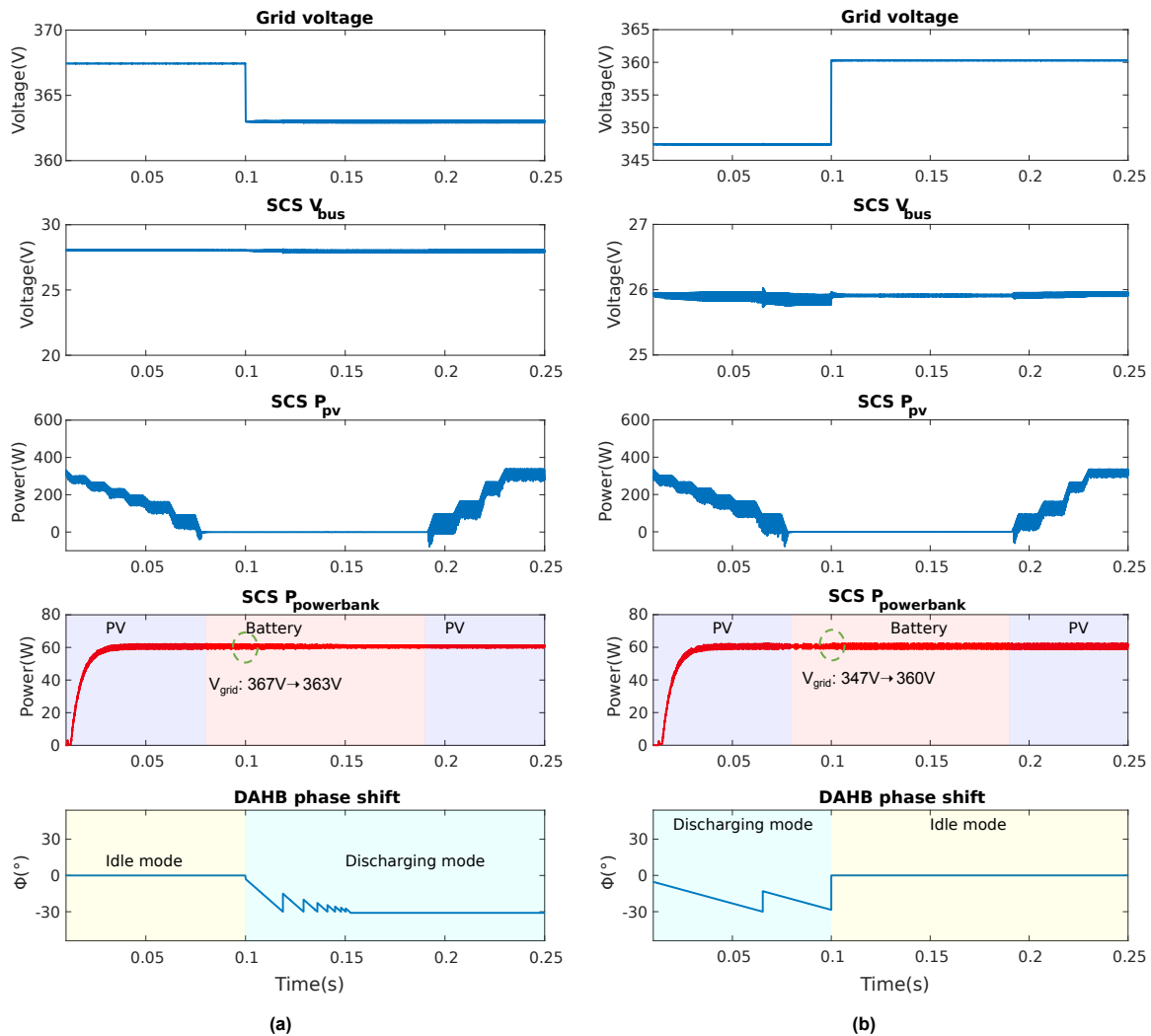


Fig.6.17a depicts the results for scenarios a and c, where both the grid voltage and SCS bus voltage remain at high levels, resulting in an idle mode. At 0.1s, the grid voltage decreases to a moderate level, leading the DAHB converter to transition from idle mode to discharging mode, consequently inducing a negative phase shift.

Fig.6.17b shows the results for scenarios e, f, g, and h. These scenarios involve inaccessible PV power, thus necessitating the following simulation setup: during the time interval from 0 to 0.1s, the grid voltage remains low while the SCS bus voltage is at a moderate level, causing the SCS to discharge into the grid. Within this timeframe, prior to 0.08 seconds, it is assumed that there is PV energy in the SCS, corresponding to scenario g, while the period from 0.08 seconds to 1 second illustrates scenario h. The converter operates in an idle mode from 0.1 seconds as the grid voltage increases to a moderate level, which is observed in scenarios e and f.

Fig.6.17c presents the outcomes for scenarios i, j, k, and l. In the time interval from 0 to 0.1 s, the grid voltage is lower than 320, while the SCS is a low voltage, leading the DAHB to charge the SCS, as represented by scenarios i and j. At 0.01 s, the voltage of the grid decreases, causing the DAHB converter to operate in idle mode, which corresponds to scenarios k and l. Fig.6.17d illustrates a scenario in which the DAHB operates in charging mode before 0.1s, then since the grid voltage decreases

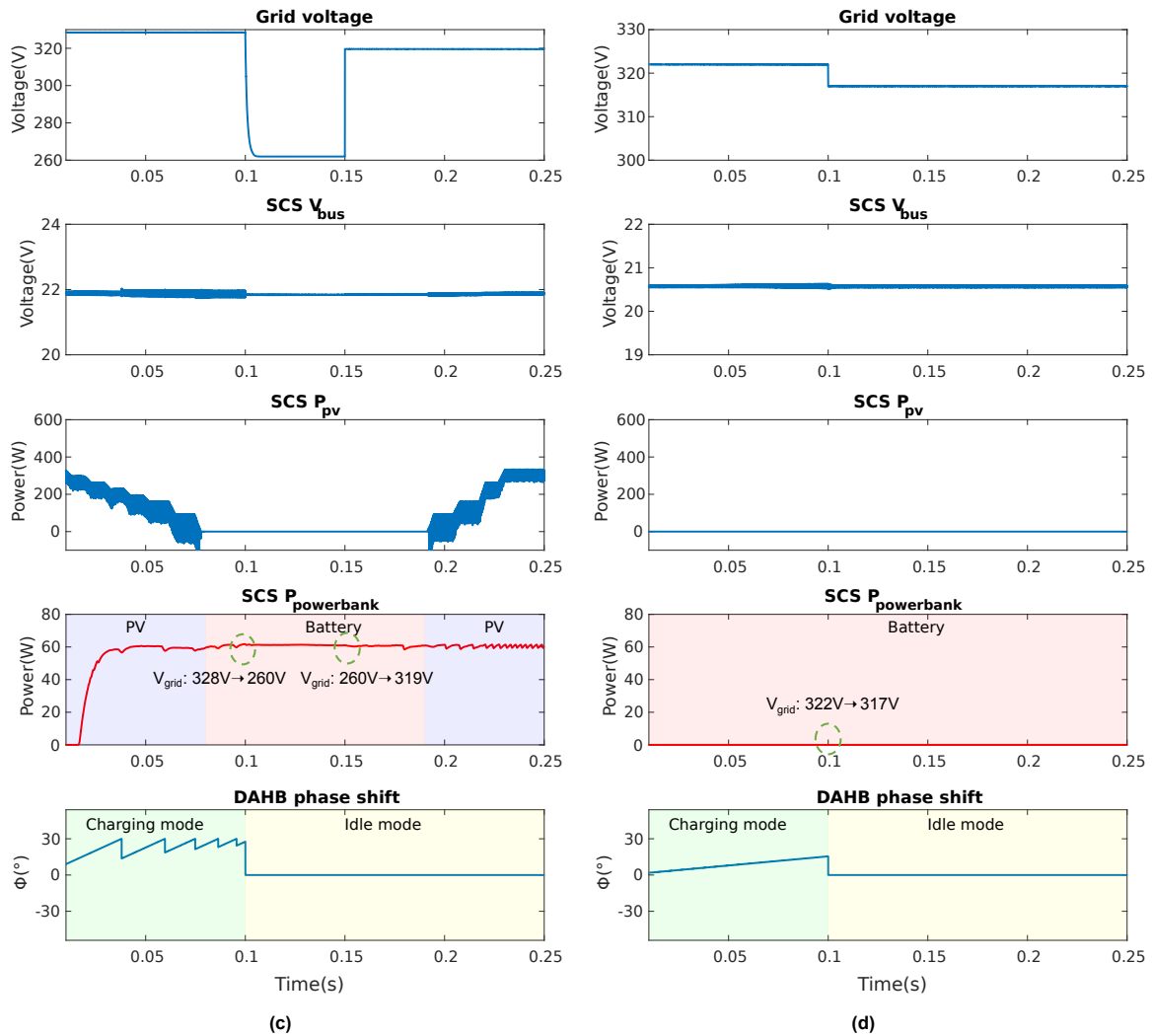


Figure 6.17: Coordinate control with decentralized SHS simulation (a) Scenario a, b, c and d (b) Scenario e, f, g, and h (c) Scenario i, j, k, and l (d) Scenario m

below 320V, the DAHB turns off the switch. The power bank will not be charged since the SCS bus voltage is less than 21V.

6.3.2. DC microgrid testing results

Line impedance

To test the real DC microgrid in the green village, the simulation results should be performed as the actual one. As a result, line impedance and the circuit breaker are considered in this section. The unit line impedance is estimated from the diameter and material of the cable, and the circuit breaker topology is based on the existing hardware in Green Village. The length of the grid bus is calculated as 100 meters and the line impedance is as follows. Fig.6.19 indicates the grid topology with line impedance and circuit breaker. The scenario Fig.5.10a is tested in this section, where both grid MPPT converters and SCS MPPT converters generate high PV energy.

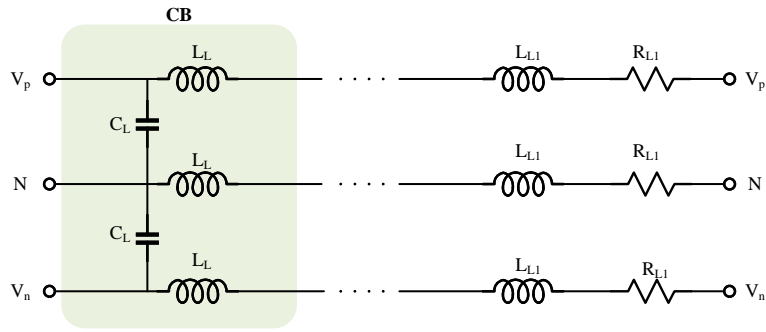


Figure 6.18: DC microgrid simulated circuit breaker and line impedance

Table 6.1: Circuit breaker and line impedance components

Line impedance components	Values
L_L	$5\mu H$
C_L	$15\mu F$
L_{L1}	$30\mu H$
R_{L1}	0.2867Ω

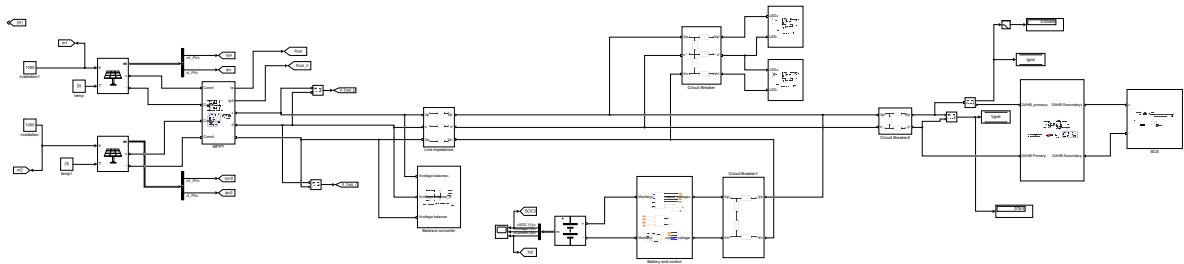


Figure 6.19: DC microgrid simulated circuit breaker and line impedance

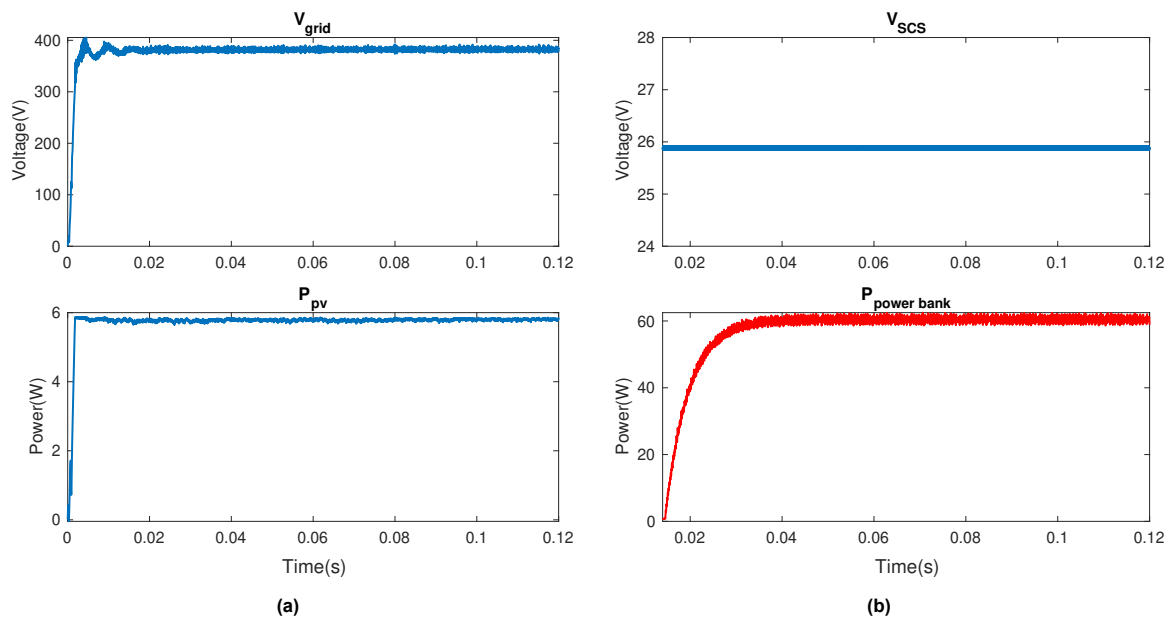


Figure 6.20: DC microgrid simulation with circuit breaker and line impedance (a) 350V grid characteristic (b) SCS characteristic

Fig.6.20 indicates that the grid bus voltage can be controlled in the steady state with small oscillations and the MPPT converter can track the maximum power. The power bank can be charged at 60W as well.

6.4. Testing results

Some important indicators of the converters connected in Green Village were measured as follows. It should be noted that SSP V1 is connected to the power supply (AC/DC converter and MPPT), and V2 connects to the LED single load.

- The DC microgrid operates for 24 hours; results are shown in Fig.6.22.
- DC microgrid operation on an island results are shown in Fig.6.23.

At 14:45, deactivate the MPPT system, initiating a transition in the power source from the PV to the AC grid. As a result, the supply voltage underwent fluctuations, ultimately settling at 350V.

Subsequently, at 14:50, the AC grid was intentionally disconnected from the microgrid, marking the DC microgrid turned off.

- DC Microgrid Interconnection and LED Droop Control Findings are shown in Fig.6.24.

At 15:14, the DC microgrid seamlessly interconnected with the AC system, followed by the activation of the circuit breaker module. Once stability was achieved, a single LED was connected to the system at 15:16:30. At 15:26:00, the LED's brightness was incrementally raised, which led to the LED going into maximum power mode.

Furthermore, the efficacy of the LED droop control was examined. As previously detailed, the grid voltage remained within the range of 320V to 325V, while the load operated in droop mode. At 15:30, the MPPT converter was deliberately disconnected, prompting an adjustable grid voltage. then continue to decrease grid voltage and cause the LED's power output to progressively drop, transitioning from its maximum power mode to droop mode. The illumination patterns for both the maximum power control mode and the droop control mode are visually contrasted in Fig.6.21.

At 15:37:00, the grid voltage was reinstated to 350V and the photovoltaic (PV) system was reconnected at 15:38:00.



Figure 6.21: LED droop control testing (a) DC microgrid voltage is 321V: droop mode (b) DC microgrid voltage is 380V: constant power mode

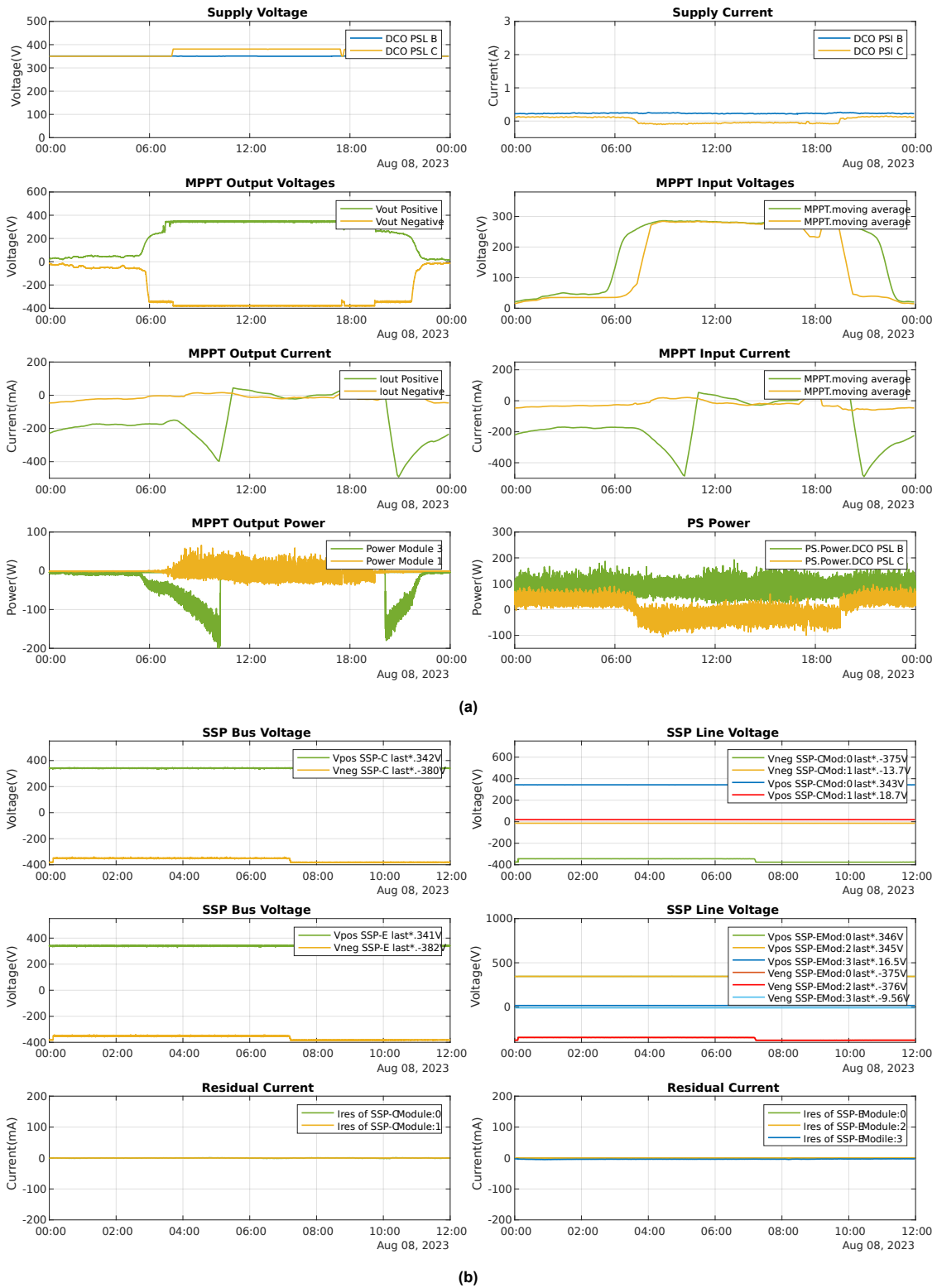


Figure 6.22: 24-hour performance data from DC microgrid converter in Green Village: (a)Real MPPT converter (b)SSP V1

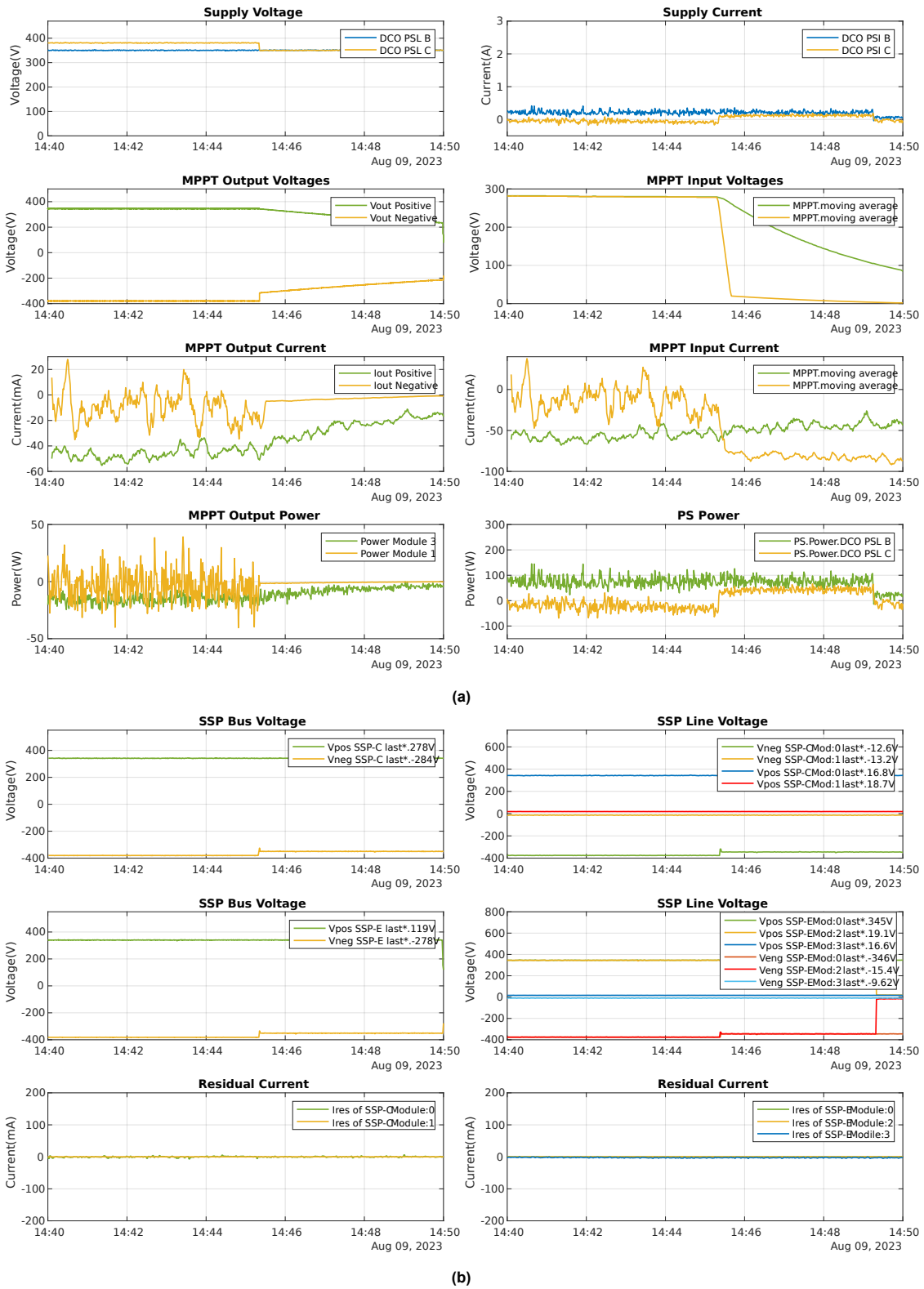
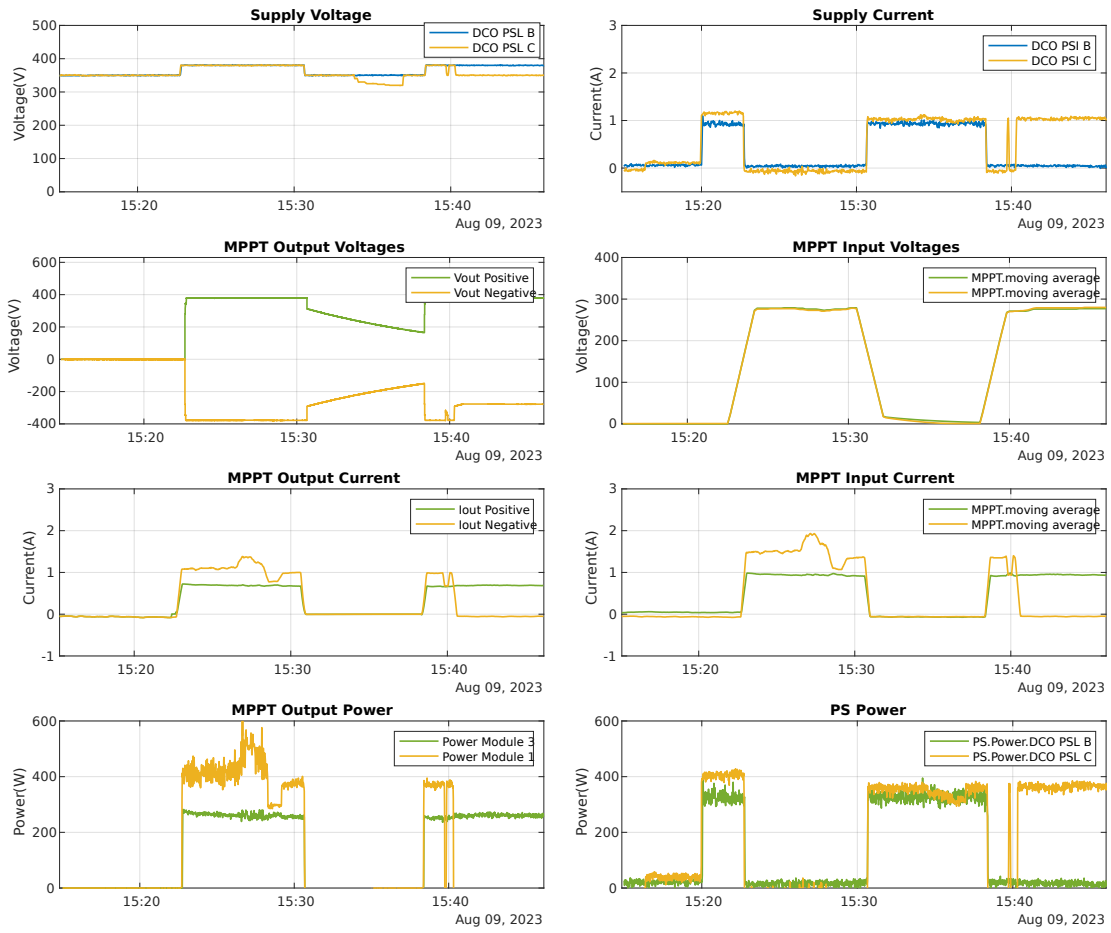
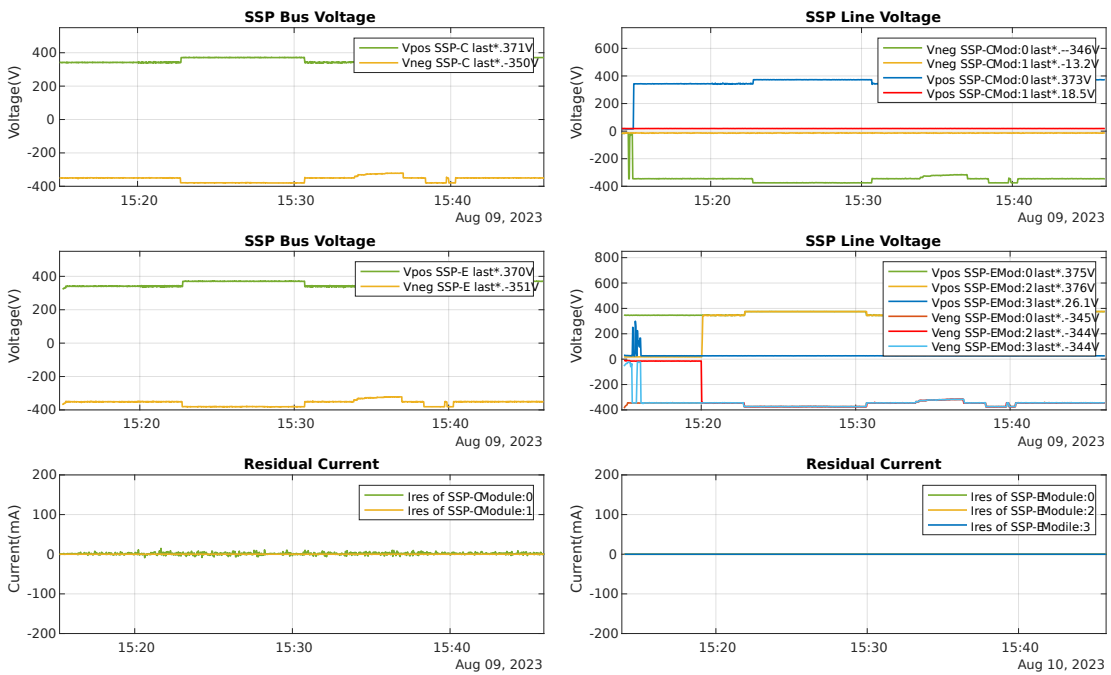


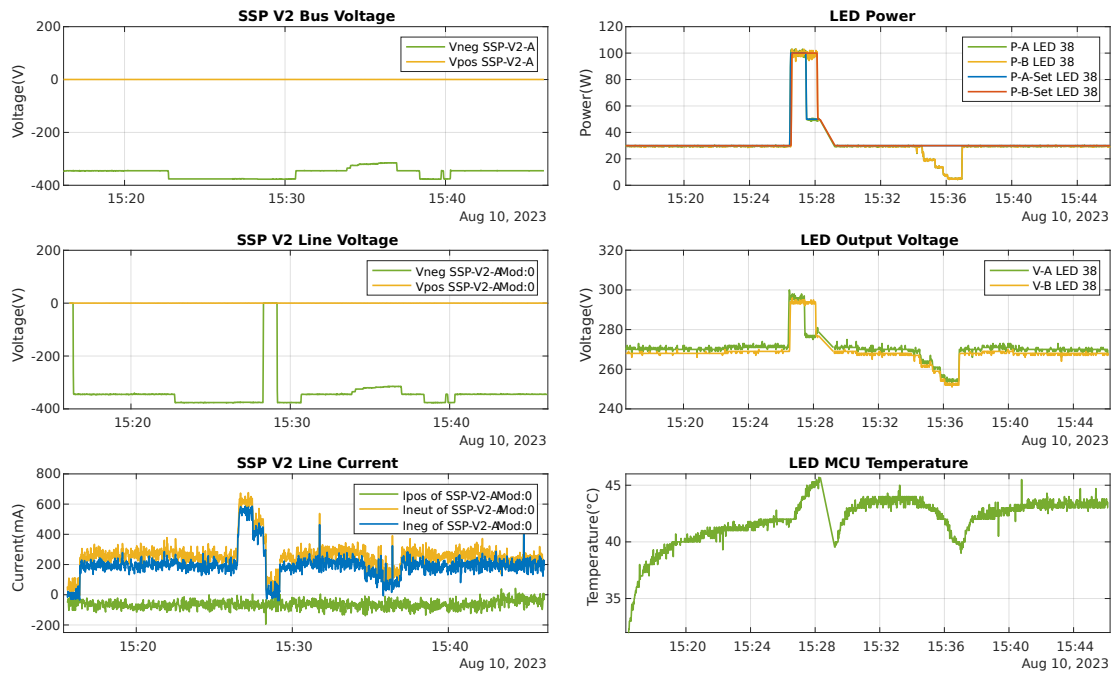
Figure 6.23: Power supplies turn off performance data from DC microgrid converter in Green Village (a)Real MPPT converter (b)SSP V1



(a)



(b)



(c)

Figure 6.24: DC microgrid interconnection and LED Droop Control (a)Real MPPT converter (b)SSP V1 (c)SSP V2 and LED

6.5. Conclusion

In this chapter, the controller developed in the previous section is verified through simulation and prototype testing. The test results demonstrate the converter's ability to guarantee ZVS and enhance smooth transitioning under variable light load conditions. With the implemented controller, the converter achieves an average efficiency of 84% under light load. Furthermore, the controller successfully overcomes the issue of unstable transitions when the burst mode switches, showing its robustness and reliability.

Furthermore, system-level coordinated controls designed before are simulated. The results indicate that both centralized SHS control and decentralized SHS control achieve seamless transitioning in various scenarios. These outcomes explore the possibility of the practical implementation of system-level controls in existing DC microgrid applications.

7

Conclusions

The main objective of this thesis is control for a DC/DC bidirectional converter and distribution control for a bipolar DC microgrid. In this chapter, the main conclusions for each research question and some recommendations for future research are given.

How to select, model, and implement DAHB bidirectional control with smooth transitions between forward and reverse directions while considering both efficiency and complexity?

Firstly, a mathematical model of the DAHB converter is built. Then, the transfer function is derived through the small signal model. Subsequently, optimal parameters for a PI controller are determined by analyzing Bode plots. Furthermore, to enhance efficiency across a wide range of loads, a novel control methodology is designed. By reducing the burst duty ratio, the phase shift is increased, thereby preventing the loss of ZVS, resulting in high efficiency under light load conditions. This strategy utilizes hysteresis and resets phase shift to an estimated value to ensure smooth transitioning when the burst duty cycle switches.

During a direction switch, a step-by-step procedure is followed to ensure smooth transitioning. First, if the burst duty cycle is initially larger than the minimum value, it steps down until it reaches the minimum value. Subsequently, the phase shift decreases to zero before gradually increasing in the opposite direction. Finally, the burst duty cycle is increased until stability is achieved. This step-by-step process guarantees a smooth transition when the direction is changed.

How to model and design simulation for system-level control for a DC grid used in energy access?

A bipolar 350V microgrid system is built in MATLAB/Simulink model. The microgrid model consists of various components, including an MPPT converter, a voltage balancing converter, streetlight LEDs, a bidirectional DC/DC converter, and a battery. Additionally, a 24V SCS is established within the system, which consists of an MPPT converter, a battery, and a power bank incorporating a bidirectional DC/DC converter and a battery. The SCS is connected to the grid via the DAHB converter. Each converter connected to the grid implements both local droop control and feedback control mechanisms to ensure that the DC microgrid components can appropriately respond to variations in the grid voltage. To enhance the realism of the simulation, another developed model taking into consideration both line impedance and circuit breakers is simulated.

How can coordinated control be designed and modeled while prioritizing renewable energy and using droop control if DAHB and SCS are considered integrated SHS?

To model different grid operation scenarios to test the robustness, integrity, and stability of decentralized DC grid control, a coordinated control is designed. The core assumption is that there is communication

inner SHS, enabling DAHB converter access to information such as the battery SoC and the PV energy available at the SCS. Thus, the coordinated control modifies the DAHB converter's reference voltage in response to different scenarios, thus managing the power flow through the DAHB converter. Furthermore, the coordinated control system also manages the battery within the SCS. It decides whether the battery should be connected or disconnected to ensure the priority of the power supply.

If DAHB and SCS are independent modules, how do design and model a decentralized control suitable for the existing grid in the Green Village?

In the green village, there is currently no direct communication established between the DAHB converter and the SCS. Therefore, an alternative coordinated control system has been developed to manage the direction of power flow in the DAHB converter. This control strategy operates by measuring and analyzing the voltage on either side of the DAHB converter. Based on this information, it dynamically adjusts the DAHB's reference voltage to control the direction of power flow within the system. This approach enables bidirectional energy access without necessitating any changes to the grid's existing structure. Furthermore, SCS voltage is more stable since components are not suddenly disconnected or connected compared to the previous method.

7.1. Future work

In this thesis a novel control strategy for DAHB converters are designed and tested, it improves the efficiency under light load condition and extends the operation range. Although the bidirectional control is simulated in Simulink and demonstrates the achievement of smooth transitioning between forward and reverse direction, only the charging prototype is tested. In the future, the discharging prototype will be tested.

Additionally, to improve safety, an alternative cascade control is designed and simulated, but it not be tested due to the scope of the thesis. In the future, it could be implemented and tested, furthermore, it is possible to develop a comparison of single voltage loop control and cascade double loop control analysis.

This thesis works on the design and simulation of a comprehensive system-level coordinated control. Prioritizing PV energy utilization while keeping the DC microgrid as a reliable backup is the principle of the control strategy, the simulations demonstrate the achievement of stable voltage for users across various scenarios. Additionally, the control strategy successfully facilitates seamless switching between these different scenarios. Nonetheless, due to some unresolved issues with the SCS and time limitations, the implementation of coordinated control in the green village remains pending.

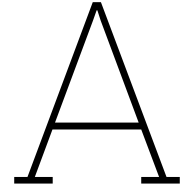
References

- [1] Hannah Ritchie, Max Roser, and Pablo Rosado. *Energy*. Ed. by Our World in Data. [Online]. 2022. URL: <https://ourworldindata.org/energy>.
- [2] IEA. *People without access to electricity worldwide*. Ed. by IEA. [Online; posted Nov 4,2022]. 2012-2022. URL: <https://www.iea.org/data-and-statistics/charts/people-without-access-to-electricity-worldwide-2012-2022>.
- [3] Our World in Data. *Number of people without access to electricity*. [Online;] 2000 – 2019. URL: <https://ourworldindata.org/grapher/number-without-electricity-by-region>.
- [4] Our World in Data, ed. *Electricity access, 2020*. [Online; posted Jun 02,2022]. 1990-2020. URL: <https://ourworldindata.org/grapher/share-of-the-population-with-access-to-electricity?country=BLR~RWA~FJI~JAM~HKG~AUS~Europe+and+Central+Asia~ABW~TJK~TCD~BRN~PYF~NLD~MEX~COD~CUW~CYM~COL>.
- [5] Debajit Palit and Kaushik Ranjan Bandyopadhyay. “Rural Electricity Access in South Asia: Is grid extension the remedy? A critical review”. In: *Renewable and Sustainable Energy Reviews* 60 (2016), pp. 1505–1515.
- [6] Nishant Narayan et al. “Quantifying the Benefits of a Solar Home System-Based DC Microgrid for Rural Electrification”. In: *Energies* 12.5 (2019), pp. 1–22. ISSN: 1996-1073.
- [7] IEA. *Solar PV power generation in the Net Zero Scenario, 2010-2030*. <https://www.iea.org/data-and-statistics/charts/solar-pv-power-generation-in-the-net-zero-scenario-2010-2030>, IEA. Licence:CCBY4.0.
- [8] Solar Energy Technologies Office. *2030 Solar Cost Targets*. Ed. by GOV ENERGY. [Online; posted Aug 13,2012]. 2022. URL: <https://ourworldindata.org/energy>.
- [9] Mashood Nasir et al. “Solar PV-Based Scalable DC Microgrid for Rural Electrification in Developing Regions”. In: *IEEE Transactions on Sustainable Energy* 9.1 (2018), pp. 390–399. DOI: 10.1109/TSTE.2017.2736160.
- [10] Tomislav Dragičević et al. “DC Microgrids—Part I: A Review of Control Strategies and Stabilization Techniques”. In: *IEEE Transactions on Power Electronics* 31.7 (2016), pp. 4876–4891. DOI: 10.1109/TPEL.2015.2478859.
- [11] Shuai Shao et al. “Modeling and Advanced Control of Dual-Active-Bridge DC–DC Converters: A Review”. In: *IEEE Transactions on Power Electronics* 37.2 (2022), pp. 1524–1547. DOI: 10.1109/TPEL.2021.3108157.
- [12] Eun-Soo Kim et al. “An improved soft switching bi-directional PSPWM FB DC/DC converter”. In: *IECON '98. Proceedings of the 24th Annual Conference of the IEEE Industrial Electronics Society (Cat. No.98CH36200)*. Vol. 2. 1998, 740–743 vol.2. DOI: 10.1109/IECON.1998.724185.
- [13] Hui Li, F.Z. Peng, and J.S. Lawler. “A natural ZVS high-power bi-directional DC-DC converter with minimum number of devices”. In: *Conference Record of the 2001 IEEE Industry Applications Conference. 36th IAS Annual Meeting (Cat. No.01CH37248)*. Vol. 3. 2001, 1874–1881 vol.3. DOI: 10.1109/IAS.2001.955786.
- [14] Yu Du et al. “Review of high power isolated bi-directional DC-DC converters for PHEV/EV DC charging infrastructure”. In: *2011 IEEE Energy Conversion Congress and Exposition*. 2011, pp. 553–560. DOI: 10.1109/ECCE.2011.6063818.
- [15] Shuai Shao et al. “Circulating Current and ZVS-on of a Dual Active Bridge DC-DC Converter: A Review”. In: *IEEE Access* 7 (2019), pp. 50561–50572. DOI: 10.1109/ACCESS.2019.2911009.

- [16] Fei Xue, Ruiyang Yu, and Alex Q. Huang. "A 98.3% Efficient GaN Isolated Bidirectional DC–DC Converter for DC Microgrid Energy Storage System Applications". In: *IEEE Transactions on Industrial Electronics* 64.11 (Nov. 2017), pp. 9094–9103. ISSN: 1557-9948. DOI: 10.1109/TIE.2017.2686307.
- [17] Zhe Zhang, Jiasheng Huang, and Yudi Xiao. "GaN-Based 1-MHz Partial Parallel Dual Active Bridge Converter With Integrated Magnetics". In: *IEEE Transactions on Industrial Electronics* 68.8 (2021), pp. 6729–6738. DOI: 10.1109/TIE.2020.3007078.
- [18] Fei Xue et al. "A novel bi-directional DC-DC converter for distributed energy storage device". In: *2015 IEEE Applied Power Electronics Conference and Exposition (APEC)*. Mar. 2015, pp. 1126–1130. DOI: 10.1109/APEC.2015.7104489.
- [19] Florian Krismer. "Modeling and Optimization of Bidirectional Dual Active Bridge DC–DC Converter Topologies". PhD thesis. ETH ZURICH, 2010.
- [20] F. Krismer, S. Round, and J. W. Kolar. "Performance optimization of a high current dual active bridge with a wide operating voltage range". In: *2006 37th IEEE Power Electronics Specialists Conference*. June 2006, pp. 1–7. DOI: 10.1109/pesc.2006.1712096.
- [21] G. Guidi et al. "Improvement of light load efficiency of Dual Active Bridge DC-DC converter by using dual leakage transformer and variable frequency". In: *2010 IEEE Energy Conversion Congress and Exposition*. Sept. 2010, pp. 830–837. DOI: 10.1109/ECCE.2010.5617909.
- [22] Vishnu Mahadeva Iyer, Srinivas Gulur, and Subhashish Bhattacharya. "Hybrid control strategy to extend the ZVS range of a dual active bridge converter". In: *2017 IEEE Applied Power Electronics Conference and Exposition (APEC)*. 2017, pp. 2035–2042. DOI: 10.1109/APEC.2017.7930979.
- [23] Jani Hiltunen et al. "Variable-Frequency Phase Shift Modulation of a Dual Active Bridge Converter". In: *IEEE Transactions on Power Electronics* 30.12 (2015), pp. 7138–7148. DOI: 10.1109/TPEL.2015.2390913.
- [24] Lin Shi, Bangyin Liu, and Shanxu Duan. "Burst-Mode and Phase-Shift Hybrid Control Method of LLC Converters for Wide Output Range Applications". In: *IEEE Transactions on Industrial Electronics* 67.2 (2020), pp. 1013–1023. DOI: 10.1109/TIE.2019.2898578.
- [25] Sónia Ferreira Pinto Ph.D. J. Fernando Silva Ph.D. "Control Methods for Switching Power Converters". In: *Power Electronics Handbook*. Ed. by Muhammad H. Rashid. ScienceDirect, 2007. Chap. 34, pp. 935–998.
- [26] Hamid Daneshpajoo et al. "Modeling of the Phase Shift plus Duty Cycle Controlled Half Bridge DC to DC Converter". In: *Intelec 2013; 35th International Telecommunications Energy Conference, SMART POWER AND EFFICIENCY*. 2013, pp. 1–6.
- [27] Hui Li, Fang Zheng Peng, and J.S. Lawler. "A natural ZVS medium-power bidirectional DC-DC converter with minimum number of devices". In: *IEEE Transactions on Industry Applications* 39.2 (2003), pp. 525–535. DOI: 10.1109/TIA.2003.808965.
- [28] Hua Bai et al. "The dynamic model and hybrid phase-shift control of a dual-active-bridge converter". In: *2008 34th Annual Conference of IEEE Industrial Electronics*. 2008, pp. 2840–2845. DOI: 10.1109/IECON.2008.4758409.
- [29] Biao Zhao et al. "Overview of Dual-Active-Bridge Isolated Bidirectional DC–DC Converter for High-Frequency-Link Power-Conversion System". In: *IEEE Transactions on Power Electronics* 29.8 (2014), pp. 4091–4106. DOI: 10.1109/TPEL.2013.2289913.
- [30] Hengsi Qin and Jonathan W. Kimball. "Closed-Loop Control of DC–DC Dual-Active-Bridge Converters Driving Single-Phase Inverters". In: *IEEE Transactions on Power Electronics* 29.2 (2014), pp. 1006–1017. DOI: 10.1109/TPEL.2013.2257859.
- [31] Sheridan Steve, Sunderland Keith, and Courtney Jane. "Swarm electrification: A comprehensive literature review". In: *Renewable and Sustainable Energy Reviews* 175 (2023). DOI: 10.1016/j.rser.2023.113157.
- [32] Mandelli Stefano et al. "Off-grid systems for rural electrification in developing countries: Definitions, classification and a comprehensive literature review". In: *Renewable and Sustainable Energy Reviews* 58 (2026), pp. 1621–1646. DOI: 10.1016/j.rser.2015.12.338.

- [33] Kurtis Unger and Mehrdad Kazerani. "Organically grown microgrids: Development of a solar neighborhood microgrid concept for off-grid communities". In: *IECON 2012 - 38th Annual Conference on IEEE Industrial Electronics Society*. 2012, pp. 5663–5668. DOI: 10.1109/IECON.2012.6389060.
- [34] Justo Jackson-John et al. "AC-microgrids versus DC-microgrids with distributed energy resources: A review". In: *Renewable and Sustainable Energy Reviews* 24 (Aug. 2013), pp. 387–405. DOI: 10.1016/j.rser.2013.03.067.
- [35] Salonen Pasi et al. "An LVDC Distribution System Concept". In: *Proceedings of the Nordic Workshop on Power and Industrial Electronics* (2008).
- [36] Dushan Boroyevich et al. "Future electronic power distribution systems a contemplative view". In: *2010 12th International Conference on Optimization of Electrical and Electronic Equipment*. 2010, pp. 1369–1380. DOI: 10.1109/OPTIM.2010.5510477.
- [37] Hiroaki Kakigano, Yushi Miura, and Toshifumi Ise. "Low-Voltage Bipolar-Type DC Microgrid for Super High Quality Distribution". In: *IEEE Transactions on Power Electronics* 25.12 (2010), pp. 3066–3075. DOI: 10.1109/TPEL.2010.2077682.
- [38] Jackson Lago and Marcelo Lobo Heldwein. "Operation and Control-Oriented Modeling of a Power Converter for Current Balancing and Stability Improvement of DC Active Distribution Networks". In: *IEEE Transactions on Power Electronics* 26.3 (Mar. 2011), pp. 877–885. DOI: 10.1109/TPEL.2011.2105284.
- [39] Binbin Li et al. "DC/DC Converter for Bipolar LVdc System With Integrated Voltage Balance Capability". In: *IEEE Transactions on Power Electronics* 36.5 (2021), pp. 5415–5424. DOI: 10.1109/TPEL.2020.3032417.
- [40] Xianjin Zhang and Chunying Gong. "Dual-Buck Half-Bridge Voltage Balancer". In: *IEEE Transactions on Industrial Electronics* 60.8 (2013), pp. 3157–3164. DOI: 10.1109/TIE.2012.2202363.
- [41] Xianjin Zhang, Chunying Gong, and Zhilei Yao. "Three-Level DC Converter for Balancing DC 800-V Voltage". In: *IEEE Transactions on Power Electronics* 30.7 (2015), pp. 3499–3507. DOI: 10.1109/TPEL.2014.2344016.
- [42] M. B. Ferrera et al. "A SEPIC-Cuk converter combination for bipolar DC microgrid applications". In: *2015 IEEE International Conference on Industrial Technology (ICIT)*. 2015, pp. 884–889. DOI: 10.1109/ICIT.2015.7125209.
- [43] N.H. van der Blij. "DC Distribution Systems: Modeling, Stability, Control Protection". PhD dissertation. Delft University of Technology, 2020.
- [44] Rodrigo A. F. Ferreira et al. "Analysis of voltage droop control method for dc microgrids with Simulink: Modelling and simulation". In: *2012 10th IEEE/IAS International Conference on Industry Applications*. 2012, pp. 1–6. DOI: 10.1109/INDUSCON.2012.6452563.
- [45] Laurens Mackay et al. "Toward the Universal DC Distribution System". In: *Electric Power Components and Systems* 45.10 (2017), pp. 1032–1042. DOI: 10.1080/15325008.2017.1318977.
- [46] M. E. Ropp D. P. Hohm. "Comparative Study of Maximum Power Point Tracking Algorithms". In: *PROGRESS IN PHOTOVOLTAICS: RESEARCH AND APPLICATIONS*. 2003, pp. 47–62. DOI: 10.1002/pip.459.
- [47] Tomislav Dragičević et al. "Supervisory Control of an Adaptive-Droop Regulated DC Microgrid With Battery Management Capability". In: *IEEE Transactions on Power Electronics* 29.2 (2014), pp. 695–706. DOI: 10.1109/TPEL.2013.2257857.
- [48] Xiaonan Lu et al. "SoC-based droop method for distributed energy storage in DC microgrid applications". In: *2012 IEEE International Symposium on Industrial Electronics*. 2012, pp. 1640–1645. DOI: 10.1109/ISIE.2012.6237336.
- [49] Nelson L. Diaz et al. "Intelligent Distributed Generation and Storage Units for DC Microgrids—A New Concept on Cooperative Control Without Communications Beyond Droop Control". In: *IEEE Transactions on Smart Grid* 5.5 (2014), pp. 2476–2485. DOI: 10.1109/TSG.2014.2341740.

- [50] Nishant Narayan et al. "Decentralized Control-Scheme for DC-Interconnected Solar Home Systems for Rural Electrification". In: *2019 IEEE Third International Conference on DC Microgrids (ICDCM)*. 2019, pp. 1–6. DOI: 10.1109/ICDCM45535.2019.9232831.
- [51] Song HuiHuan Zacchaeus, Wesley Poh Qi Tong, and R.T. Naayagi. "Modelling and Simulation of DC microgrid". In: *2018 IEEE 4th Southern Power Electronics Conference (SPEC)*. 2018, pp. 1–5. DOI: 10.1109/SPEC.2018.8636004.
- [52] Yinjiao Xing et al. "State of charge estimation of lithium-ion batteries using the open-circuit voltage at various ambient temperatures". In: vol. 113. 2014, pp. 106–115. DOI: 10.1016/j.apenergy.2013.07.008.
- [53] Alberto Rodríguez et al. "Different Purpose Design Strategies and Techniques to Improve the Performance of a Dual Active Bridge With Phase-Shift Control". In: *IEEE Transactions on Power Electronics* 30.2 (2015), pp. 790–804. DOI: 10.1109/TPEL.2014.2309853.
- [54] Karl Johan Åström. In: "PID control," in *Control System Design*. Department of Mechanical & Environmental Engineering, 2002, pp. 216–219.
- [55] Bo-Yuan Chen and Yen-Shin Lai. "Switching Control Technique of Phase-Shift-Controlled Full-Bridge Converter to Improve Efficiency Under Light-Load and Standby Conditions Without Additional Auxiliary Components". In: *IEEE Transactions on Power Electronics* 25.4 (2010), pp. 1001–1012. DOI: 10.1109/TPEL.2009.2033069.
- [56] Yiwei Pan et al. "A Dual-Loop Control to Ensure Fast and Stable Fault-Tolerant Operation of Series Resonant DAB Converters". In: *IEEE Transactions on Power Electronics* 35.10 (2020), pp. 10994–11012. DOI: 10.1109/TPEL.2020.2975348.



Cascaded PI Control for a DAHB Converter with SPS

The results of the prototype discharge test are omitted from this thesis, as a significant spike breaks the components when it starts to transfer power. The possible reason is that the phase shift reaches saturation in the beginning state, resulting in an instantaneous large current. To solve this issue, an alternative approach involving cascaded voltage and current control is investigated. The work of [56] validates that the implementation of a double loop enhances the dynamic performance of the overall control system.

A.1. Cascade PI control

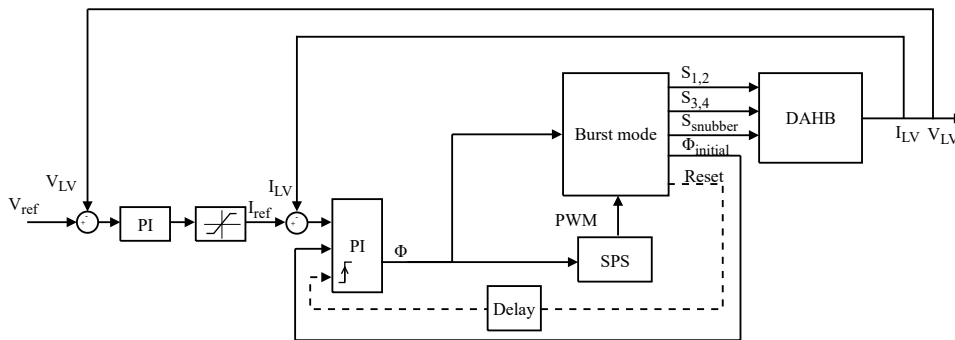


Figure A.1: Cascade double loop control based on novel burst mode with reset phase and SPS hybrid control method block diagram

Two PI regulators are connected in a cascade scheme with two loops, a voltage loop, and an inner current loop as shown in Fig.A.1. The PI parameters are tuned as experience shown below.

Table A.1: PI parameters of cascade voltage and current control

Parameters	Current loop	Voltage loop
Kp	0.001	400
Ki	50	1

A.2. Simulation results

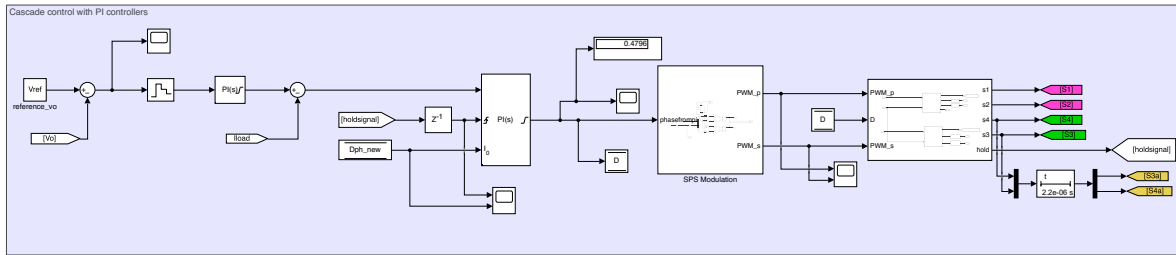


Figure A.2: Cascade double loop control model in Matlab/Simulink

The control loop is modified as the control block diagram shows. Fig.A.3a shows the performance of cascade PI control. At 0.1s, the load decreases from 300W to 150W, and both voltage and power can achieve smooth transitioning. Similar outcomes can be seen in Fig.A.3b.

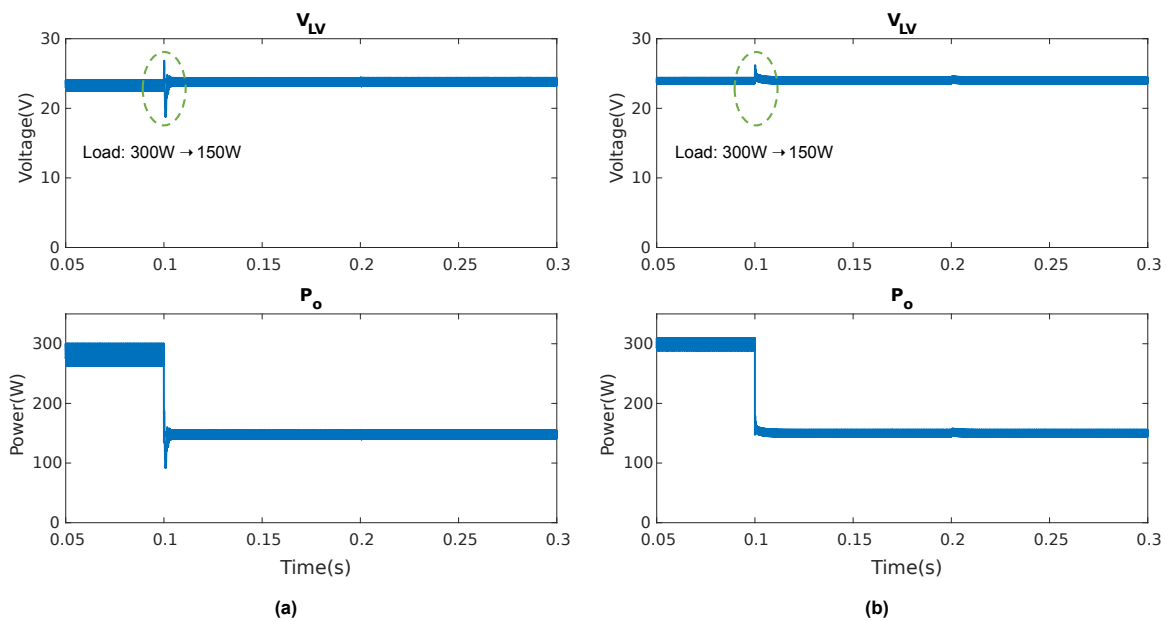


Figure A.3: Cascade control simulation results: (a) Cascade voltage and current control (b) Voltage control

A.3. Conclusion

In this chapter, the possibility of deploying a cascade voltage and current control strategy is investigated. This approach offers the advantage of saturating the output current, thereby enhancing the converter's safeguarding capabilities. As a result, this control strategy proves to be well-suited for discharging converters. The simulation analysis shows high dynamic performance.

B

Experimental Setup

In this chapter, the hardware used in the experimental DC distribution system is introduced.

B.1. Power Electronic Converters

The key contribution of the laboratory scale system is the controller of a DAHB converter. A photo of the converter is shown below.



Figure B.1: DAHB converter prototype

B.2. Laboratory Power Supplies

The input side of the DAHB converter is connected to an SM 500-CP-90 power supply, which is a bidirectional power supply rated for 500 V and 90 A in two quadrants, and can therefore be used as a source as well as an electronic load.



Figure B.2: SM 500-CP-90 bidirectional power supply from Delta Elektronika

B.3. Laboratory loads

A load is connected to the secondary side, which can be used to simulate the state of charge of the battery.



Figure B.3: 72-13210 DC Electronic Load from Tenma

Acknowledgements

I am very grateful that the topic of my thesis corresponds to my motivation to study here. The journey leading up to the MSc thesis has been long but not lonely. I wish to extend my gratitude to those who have contributed to my path. Without their support, this thesis would have remained an unattainable aspiration.

First of all, I would like to express my gratitude to Dr. Ir. Laurens Mackay for giving me the opportunity to pursue my thesis in DC Opportunities. Throughout my thesis, he has given me guidance and freedom to develop the thesis in accordance with my vision. I would like to thank him for encouraging me to be more creative and comprehensive in my work. I also hold gratitude for Dr. Zian Qin, whose encouragement and insightful feedback have illuminated my path during my MSc thesis.

The outcome of my efforts in this thesis would not have been possible without the steadfast assistance of Jesse Echeverry, my daily supervisor. His patient guidance over the past ten months has been significant in my progress. I appreciate his patience and support in the last year. He spent his time for me to organize weekly meetings to discuss the process and gave me guidance and suggestions which helped me make the thesis more comprehensive and complete. To be honest, I must candidly acknowledge that he helped me construct unattainable ideas into reality step by step.

Equally deserving of recognition is Sachin Yadav, my on-campus daily supervisor, whose guidance has been instrumental in my journey. He has guided me a lot and has been very patient and supportive during the process. His willingness to engage in discussions and the wealth of constructive suggestions he shared have illuminated my path.

I am also indebted to the individuals at DC Opportunities with whom I collaborated during my MSc thesis, Hidde Moens, Gerasimos Maroulis, Lukas Irazusta Gorostidi, and Samad Shah. Their assistance and support spanned every aspect of design, testing, and even presentation. Their contributions have left an indelible mark on my journey.

To my colleagues and friends within the realm of DC Opportunities, I am moved by the profound bond we share. I will never forget the time we spent together during lunch, on the beach volleyball, and company dinner. These are precious memories for me. I also thank the new friends that made in Delft. They encouraged me when I was not making any progress and upset during my MSc thesis. The friendship is truly memorable and makes my life much more meaningful with you here.

Last, but not least, I am profoundly grateful to my parents. I appreciate the support and trust that have given me the privilege of this life-altering experience at TU Delft. Their encouragement has been the cornerstone of my journey, and I shall forever cherish the profound impact they've had on my life.